DYNAMICS OF INTELLIGENT POLY(N-ISOPROPYLACRYLAMIDE) MICROGELS

A Dissertation

by

SRINIVASA RAO PULLELA

Submitted to the Office of Graduate Studies of
Texas A&M University
in partial fulfillment of the requirements for the degree of

DOCTOR OF PHILOSOPHY

May 2009

Major Subject: Chemical Engineering

DYNAMICS OF INTELLIGENT POLY(N-ISOPROPYLACRYLAMIDE) MICROGELS

A Dissertation

by

SRINIVASA RAO PULLELA

Submitted to the Office of Graduate Studies of
Texas A&M University
in partial fulfillment of the requirements for the degree of

DOCTOR OF PHILOSOPHY

Approved by:

Chair of Committee,	Zhengdong Cheng
Committee Members,	Arul Jayaraman
	Victor Ugaz
	Kenith Meissner
Head of Department,	Michael Pishko

May 2009

Major Subject: Chemical Engineering

ABSTRACT

Dynamics of Intelligent Poly(N-isopropylacrylamide) Microgels. (May 2009)

Srinivasa Rao Pullela, B.S, University of Mumbai; M.S, Oklahoma State University

Chair of Advisory Committee: Dr. Zhengdong Cheng

This dissertation investigates the self assembly and automatic oscillation of intelligent poly (N-isopropylacrylamide) [PNIPAM] microgel particles. The equilibrium phase diagram as a function of temperature and concentration was constructed for the charged PNIPAM spheres. The PNIPAM microgel particles display rhythmic size oscillations when covalently coupled to a nonlinear chemical reaction, the Belousov-Zhabotinsky (BZ) reaction. The nonequilibrium dynamics of PNIPAM microgels in the presence of BZ reaction was studied by the systematic variation of substrate concentrations and temperature. In addition, the BZ chemical reaction was modeled to reveal the existence of upper temperature limits for nonlinear chemical systems.

The experiments employ environment sensitive PNIPAM particles that are sensitive to temperature, pH, and ionic strength. The PNIPAM particles have been demonstrated here to behave as hard spheres at low pH values and soft spheres at high pH. This is done by measuring the freezing and melting boundary of fluid-crystal coexistence region with a new technique which is simpler and quicker compared to the traditional sedimentation method.

A novel method was developed to achieve size uniformity of PNIPAM gel particles with covalently-bound tris(bipyridyl)ruthenium(II) via the coordination chemistry between a ruthenium complex and the monodispersed PNIPAM gel particles bearing bipyridine ligands. The correlation between the dynamic behavior of BZ reaction induced

mechanical oscillations of PNIPAM particles and substrate concentrations was presented in a ternary phase diagram. In particular, the dependence of oscillation frequency and induction time on the substrate concentrations was studied. The temperature dependency of the induction time and oscillatory frequency of the BZ reaction in this polymer-immobilized catalyst system were compared to the bulk BZ reaction with the catalyst in the solution phase. Prolonged induction times were observed for the immobilized catalyst, compared with free catalyst, while little difference was observed on the oscillation frequency.

A theoretical improvement has been achieved by incorporating the temperature dependence in the BZ Oregonator model. Bifurcation has been calculated in the phase space spanned by initial reagents concentration ratio, stoichiometric factor and temperature. The existence of upper temperature limits has been demonstrated.

DEDICATION

To my wonderful parents,

who sacrificed many things so that I could find my way in life.

To my loving sisters,

who supported every decision that I made and influenced whom I have become today.

To my beloved wife,

who gave moral support when needed.

To my professor, Zhengdong Cheng,

who was instrumental in shaping my career.

ACKNOWLEDGEMENTS

Numerous people have to be thanked for helping me through this stage of my life; most of them cannot be mentioned in this short space. Foremost, I am very grateful to my advisor, Dr. Zhengdong Cheng, for giving me an opportunity to work in his lab. I am deeply indebted to him not only for his knowledge, patience, and support, but also for his guidance to direct me into a professional career. I am very thankful to him for correcting every single mistake in my write-ups, presentations, and for teaching me how to write in scientific language and publish research work. Dr. Cheng gave me the freedom to pursue research, offered great conversations, pushed me to become more productive, and is always available for discussions about research and future life plans. His excitement for science is a true inspiration to me. I am extremely fortunate and proud to be his (first) student. I look forward to continuing more fruitful interactions ahead.

I also would like to thank my committee members, Dr. Arul Jayaraman, Dr. Victor Ugaz, and Dr. Kenith Meissner for their insightful comments, guidance, and support throughout the course of my research. I will always remember their friendly and helping nature. I greatly acknowledge the generous funding support from Dr. Sam Mannan in my last semester. I extend my sincere gratitude to Dr. Mahmoud El-Halwagi, and Dr. Tahir Cagin for their supportive words of wisdom whenever I was at crossroads. I cannot forget the help that I received from Dr. Michael Bevan. Thanks to him for discussions about my research. I would like to thank all other faculty members and administrative staff in the Chemical Engineering Department for their friendly and helping nature. I owe a special debt of gratitude to Towanna Arnold for her suggestions right from day one to the present.

My time here at Texas A&M University certainly would not have been productive, and not nearly as enjoyable, had I not had wonderful colleagues and friends around me. The

camaraderie, yet professional atmosphere among all past and current group members of Dr. Cheng's lab, has contributed to the successful completion of my research work. A great deal of gratitude goes to my research partners Dr. Jingyi Shen, Peng He, Dr. Dawei Luo, and Diego Cristancho. Thank you very much for your help at the crucial moments of the project. Your friendship is something I will always treasure. I would like to thank Dr. Richard Beckham and Dr. Gregory Fernandez for making me understand the theoretical aspects of colloidal phase transitions. I am grateful to my dear friend, Marcus Siddhartha, and many others who are always there to share both happy and unhappy moments. You have all been an integral part of my life and I look forward to sharing many more happy moments in the future.

The greatest appreciation is reserved for my parents who have devoted so much of their lives to the betterment of their children. I am very grateful for the sacrifices they have made, and forever indebted to their selflessness and affection. They have provided me every opportunity to thrive in this world, and they are always in my thoughts and prayers. I also hold equal appreciation for my two loving sisters, who are the sources of my strength, love and inspiration. They have always supported the decisions that I made, and their support and love have the biggest influence in who I am. I would like to express my gratitude to my brothers-in-law for their support and generosity. Last, but not least, I would like to acknowledge my wonderful friend and wife, Shobha, for her endless patience, understanding, and love as I have labored to complete my Ph.D., for helping to keep me grounded and for maintaining a broader positive perspective while in College Station.

NOMENCLATURE

AA	Acrylic Acid
BZ	Belousov-Zhabotinsky
LCST	Lower Critical Solution Temperature
NIPAM	N-isopropylacrylamide
PNIPAM	Poly(N-isopropylacrylamide)
TCA	Tricarboxylic Acid
T	Temperature
f	Stoichiometric Factor

TABLE OF CONTENTS

CHAPTER Page

LIST OF FIGURES

FIGURE Page

FIGURE Page

FIGURE Page

LIST OF TABLES

CHAPTER I

INTRODUCTION: POLY(N-ISOPROPYLACRYLAMIDE) GELS

1.1 Stimuli-Responsive Poly(N-isopropylacrylamide) Gels

Response to stimuli is a basic phenomenon in living systems. Aqueous environment-sensitive gels form an interesting subset of polymer gels, offering promising routes to mimic complex functions of living systems. The polymer gels are swollen in water and contain up to 97% of water. They undergo relatively large and abrupt reversible size changes in response to small external variations in the environmental conditions. They are classified according to the stimuli they respond to as: temperature, pH, ionic strength, light, electric and magnetic field sensitive. The swell-shrink properties of microgels depend upon the subtle balance of polymer-polymer vs. polymer-water interactions. Their ability to swell and de-swell according to conditions makes them an interesting proposition for use in intelligent materials. This phenomenon has been exploited in many areas such as drug delivery,[1-4] chemical and biosensing,[5-7] nano-patterning[8] etc.

Poly(N-isopropylacrylamide) [PNIPAM] is a well studied polymer that exhibits reversible phase transitions with the applied stimuli. The mechanistic understanding of swell and de-swell phase transition, fine control of the structure-property relationship, and novel biomedical applications of PNIPAM gels are the subjects of focus for many recent studies. Tanaka reported the thermodynamics underlying the collapse of the polymer network in polyacrylamide gels for the first time in 1978.[9] PNIPAM exhibits a lower solution critical temperature (LCST) of about 32°C.[10] Below the LCST, PNIPAM is soluble in water and favorable interactions via hydrogen bonding between amide

---

This dissertation follows the style of *Journal of American Chemical Society*.

groups of the polymer and water molecules lead to the dissolution of polymer chains. Above the LCST, the hydrogen bonds are broken and water molecules are expelled from the polymer, resulting in precipitation of the polymer.[11] The phase transition of PNIPAM from a soluble to insoluble state can be seen on a nanometer scale using atomic force microscopy (AFM).[12] Confocal laser scanning microscopy (CLSM) has been used to probe the mesoscopic internal structures of network polymers, including those of poly(NIPAM), were shown to be composed of continuous two-domain structures with dense and sparse regions in the polymer network demonstrating fixed concentration fluctuations.[13] Copolymerization of NIPAM with hydrophobic comonomers, such as butylmethacrylate, decreases the LCST of aqueous copolymer solution. And copolymerization with hydrophilic comonomers, such as acrylic acid or hydroxy ethyl methacrylate, results in an increase of the LCST.[11]

PNIPAM gels and their derivatives have been tested for many biological applications such as separations, enzyme immobilization, gene delivery and cell culture.[14-18] PNIPAM polymers were investigated for the on–off control of avidin–biotin binding.[14] Below the transition temperature of 32°C, NIPAM copolymers forms favorable polymer–water interactions and the polymer interferes with the biotin-binding site on the avidin, whereas above the transition temperature, the polymers are collapsed and cannot interfere with the binding sites. In a related research, bioseparations of enzymes has been achieved using the PNIPAM conjugated to trypsin and chymotrypsin.[14,15] Although the enzyme activity decreased to <50% of the native enzyme activity, the ease of separation at high temperatures was demonstrated.

pH sensitive PNIPAM hydrogels have been used to develop controlled release formulations. Kumacheva et al. have reported novel bio-functionalized pH sensitive PNIPAM microgels that can specifically target tumor cells.[19] The site specific treatment involves the advantage of the receptor-mediated endocytosis process and use pH changes in the intracellular environment for targeted delivery of anticancer drug into the tumor

cells. Lyon et al. have reported folate-conjugated PNIPAM gels for specific targeting of cancer cells.[20] The conjugated folate-PNIPAM gel particles act as potential candidates for cytosolic drug delivery in addition to their large swelling capacity. Yang has demonstrated a pH sensitive PNIPAM gel that is stable in neutral media, but release drug in the acid media due to the deformation of the polymer gel.[21]

A novel cell co-culture method was investigated using thermosensitive grafted PNIPAM surfaces.[22] By covalently grafting PNIPAM onto tissue culture surfaces, cell adhesion and detachment were regulated by temperature.[23,24] Cell manipulation techniques using temperature responsive culture surfaces grafted with PNIPAM were also reported.[25] A decrease in culture temperature below the LCST resulted in the release of cardiac myocyte sheets from the cell culture dishes without enzymatic treatment. PNIPAM–acrylic acid copolymers were used for entrapping islets of Langerhans for a refillable biohybrid artificial pancreas.[18]

Hybrid materials containing magnetic nanoparticles and thermosensitive PNIPAM have received a lot of interest during the last few years due to their faster response.[26,27] The magnetic functionality can be used to guide the microgels in particular parts, thus opening up the possibility of their use as targeted dug delivery systems. PNIPAM gels seeded with ferromagnetic materials demonstrated magnetic-field-sensitive swelling–deswelling transition. The transition resulted from the heat released by magnets in a magnetic field, followed by the collapse of temperature-sensitive PNIPAM copolymer.[28]

PNIPAM polymers are also pH sensitive when copolymerized with ionizable functional groups such as poly(acrylic acid) or poly(allylamine)[29] etc. By generating the charge along the polymer backbone, the electrostatic repulsion results in an increase in the hydrodynamic volume of the polymer.

1.2 Phase Transition Studies in PNIPAM Colloidal Suspensions

In contrast to the conventional colloids, the inter-particle potential in aqueous dispersion of PNIPAM microgel particles is sensitive to the temperature changes. Consequently, the phase diagram of PNIPAM dispersions differs from those for ordinary colloids where the inter-particle potential in general is invariant with temperature.[30,31] Phase transitions in colloidal systems have been studied over past decades not only because of theoretical interests for addressing fundamental questions about the nature of liquids, crystals and glasses, but also for many practical applications of colloids, especially for the fabrication of nanostructured materials.[32-35] Previous investigations on the phase behavior of colloidal dispersions, however, are primarily focused on hard-sphere-like particles such as polymethylacrylate, silica, or polystyrene; only a limited number of studies are available on those colloids where the inter-particle potential is a strong function of temperature. Aqueous dispersions of poly-*N*-isopropylacrylamide (PNIPAM) microgel particles exhibit a reversible and continuous volume transition in water around 34°C.[36,37] The lower critical solution temperature behavior of a PNIPAM microgel could affect the inter-particle forces between microgels, resulting in drastic different phase behavior from those of conventional hard-sphere-like colloidal systems.

1.2.1 Volume Transition of PNIPAM Particles

The Flory and Rehner theory for gel swelling assumes uniform distributions of polymer segments and cross-linking points throughout the polymer network.[38] Due to the heterogeneous nature of PNIPAM particles,[37] an empirical modification of the Flory–Rehner theory has been proposed by Hino and Prausnitz.[39] This theory has been applied successfully to describe the volume transition of bulk PNIPAM gels. The same thermodynamic model for bulk polymer gels is also applicable to microgel particles because the physics for the volume transition is independent of the particle size as long as the surface effect is unimportant.

At swelling equilibrium, the chemical potential of water is equal inside and outside the microgel particle:

$$\mu_{water}^{gel} = \mu_{water}^{pure}. \quad (1)$$

The chemical potential inside the gel includes two contributions: one is the same as that in the aqueous solution of PNIPAM polymer, and the other arises from the cross-linking of polymer chains or from the gel elasticity:

$$\mu_{water}^{gel} = \mu_{solution}^{polymer} + \mu_{water}^{elasticity}. \quad (2)$$

The chemical potential of water in an aqueous PNIPAM solution can be calculated from the Flory–Huggins theory,

$$\left(\mu_{water}^{polymer} - \mu_{water}^{pure}\right)/kT = \ln(1-\phi) + \chi\phi^2. \quad (3)$$

Where φ is the volume fraction of PNIPAM polymer, and the Flory polymer–solvent energy parameter χ is given empirically as a function of temperature and composition,

$$\chi = \frac{3}{1-0.65\phi}\left[2\ln\left(\frac{5001}{1+5000\exp(2458.867/T)}\right) - \frac{4566.468}{T}\right] \quad (4)$$

Eq. (4) is obtained by fitting the Flory–Huggins theory with the phase-equilibrium data for non-cross-linked PNIPAM polymer in water.[39] For microgels, the volume fraction φ in Eq. (3) corresponds to that inside of individual particles.

The second term on the right-hand of Eq. (2) arises from gel elasticity. This term takes into account the effect of the network formation on the chemical potential of the solvent. According to the modified Flory-Rehner theory by Hino and Prausnitz,[39] the chemical potential of water due to gel elasticity is given by,

$$\mu_{water}^{elasticity}/(kT) = \frac{\phi_0}{m}\left[\left(\frac{\phi}{\phi_0}\right)^{1/3} - \left(\frac{\phi}{\phi_0}\right)^{5/3} + \left(\frac{\phi}{2\phi_0}\right)\right]. \quad (5)$$

where m is the average number of segments between two neighboring cross-linking points in the gel network, and ϕ_0 is the polymer volume fraction in the reference state where the conformation of the network chains is closest to that of unperturbed Gaussian chains. Approximately, ϕ_0 is equal to the volume fraction of polymer within the microgel particles at the condition of preparation. Substitution of Eqs. (2) – (5) into Eq. (1) yields

$$\ln(1-\phi) + \phi + \chi\varphi^2 + \frac{\phi_0}{m}\left[\left(\frac{\phi}{\phi_0}\right)^{1/3} - \left(\frac{\phi}{\phi_0}\right)^{5/3} + \left(\frac{\phi}{2\phi_0}\right)\right] = 0. \quad (6)$$

At a given temperature, Eq. (6) can be used to find the polymer volume fraction ϕ. Once we have ϕ, the diameter of PNIPAM particles can be found from,

$$\frac{\sigma}{\sigma_0} = \left(\frac{\varphi}{\phi_0}\right)^{1/3}, \quad (7)$$

where σ_0 is the particle diameter at the reference state. The average chain length m and the volume fraction of polymer ϕ_0 at the reference state are obtained by fitting Eqs. (6)

and (7) to the diameters of microgel particles obtained from static and dynamic light scattering experiments.

1.2.2 Inter-particle Potential and Osmotic Second Virial Coefficient

The inter-particle potential $U(r)$ is related to the osmotic second virial coefficient B_2 by

$$B_2 = 2\pi \int_0^\infty \left[1 - e^{-U(r)/kT}\right] r^2 dr , \tag{8}$$

where r is center-to-center distance between colloidal particles.

It is assumed that the interaction potential for PNIPAM particles can be represented by a function that includes a hard sphere repulsion and a van der Waals attraction. A similar potential was used by Senff and Richttering for representing the phase behavior of rheological properties of PNIPAM microgel dispersions.[37] The hard-sphere diameter is related to the swelling of gel particles and can be calculated from Eq. (7). The van der Waals attraction beyond the hard-sphere diameter can be represented by

$$U_A(r) = -\frac{H}{r^n}, \tag{9}$$

where H is the Hamaker constant, and n is assumed as 8 in considering that the range of attraction between colloidal particles (relative to the particle size) is shorter than that between atomic molecules. Approximately, the Hamaker constant of microgel particles is given by

$$H \propto \rho_m{}^2, \tag{10}$$

where ρ_m represents the number density of polymeric groups within each particle. The proportionality constant in Eq. (10) is independent of temperature and the polymeric group density ρ_m. From Eqs. (9) and (10), the attractive potential due to the van der Waals forces is,

$$U_A(r) = -k_A\left(\frac{T_0}{T}\right)\left(\frac{\sigma_0}{\sigma}\right)^{6+n}\left(\frac{\sigma}{r}\right)^n, \tag{11}$$

where k_A is a dimensionless constant and T_0 is a reference temperature that is introduced for the purpose of dimensionality. In Eq. (11), the parameters T_0, σ_0, and k_A are temperature independent, and they can be obtained by fitting Eq. (8) to the osmotic second virial coefficients obtained from static light scattering measurements.

1.2.3 Thermodynamic Model for the Fluid and Solid Phase

A first order perturbation theory is appropriate for a dispersion of microgel particles in the fluid state because higher order terms are insignificant when the perturbation arises only from short-range attractions.[40] The Helmholtz energy of the fluid phase includes a hard-sphere contribution that is given by the Carnahan–Starling equation of state and a perturbation that takes into account the van der Waals attraction (Eq. 11). In dimensionless units, the Helmholtz energy is given by

$$\frac{F}{NkT} = \ln(\eta) - 1 + \frac{4\eta - 3\eta^2}{(1-\eta)^2} + 12\eta\int_1^\infty x^2 g_F^{HS}(x)\frac{U_A(x)}{kT}dx, \tag{12}$$

where N represents the total number of particles, $\eta = \pi\rho\sigma^3/6$ is the particle packing fraction, ρ is the particle number density, and $g_F^{HS}(x)$ is the hard-sphere radial distribution function. The integral in Eq. (12) is correlated as a function of particle

packing fraction using the radial distribution function $g_F^{HS}(r)$ obtained from the Percus−Yevick equation,[41]

$$I_F(\eta) \equiv \int_1^\infty x^{-6} g^{HS}(x) = 0.027224\eta^2 + 0.1642\eta + 0.2007. \tag{13}$$

The quadric form as given in Eq. (13) is applicable to the reduced density $\rho\sigma^3 < 0.6$.

Replacement of the integral in Eq. (12) with $I_F(\eta)$ gives,

$$\frac{F}{NkT} = \ln(\eta) - 1 + \frac{4\eta - 3\eta^2}{(1-\eta)^2} - 12\eta I_F(\eta)\varepsilon^*, \tag{14}$$

where

$$\varepsilon^* = \frac{\varepsilon}{kT}\left(\frac{T_0}{T}\right)\left(\frac{\sigma_0}{\sigma}\right)^{6+n}. \tag{15}$$

Other thermodynamic properties can be derived from Eq. (14) following standard thermodynamic relations.

To describe the thermodynamic properties of the solid phase, a perturbation approach is followed similar to that for the fluid phase. The Helmholtz energy includes a contribution from the reference hard sphere crystal and a perturbation taking into account the van der Waals attraction,

$$\frac{F}{NkT} = \frac{F^{HS}}{NkT} + 12\eta\int_1^\infty x^2 g_S^{HS}(x)\frac{U_A(x)}{kT}dx, \tag{16}$$

where $g_S^{HS}(x)$ is the radial distribution function of the hard sphere solid. As in a hard-sphere system, an aqueous dispersion of PNIPAM microgel particles forms a face centered cubic (fcc) lattice in the solid phase even when the particles are at low cross-linking density.[42]

The Helmholtz energy of the hard-sphere solid is given by,

$$\frac{F^{HS}}{NkT} = \ln\left[\frac{8}{\sqrt{2}}\left\{\rho/\rho_0\right\}^{1/3} - 1\right]. \tag{17}$$

Compared with the original Lennard-Jones and Devonshire cell model,[43] the improved cell model introduces a factor of 8, taking into account the fact that the neighboring particles share partially the free space. The modified cell model provides accurate freezing and melting densities for the fluid–solid transition of uniform hard spheres. The hard-sphere radial distribution function $g_S^{HS}(r)$ can be calculated using a modified Gaussian model for density distributions.

The perturbation term in Eq. (16) is intergrated using the radial distribution function $g_S^{HS}(r)$ for the hard-sphere solid. The final expression for the Helmholtz energy of the solid phase is given by

$$\frac{F^{HS}}{NkT} = -\ln\left[\frac{8}{\sqrt{2}}\left\{\rho/\rho_0\right\}^{1/3} - 1\right] - 12\eta I_S(\rho)\varepsilon^*, \tag{18}$$

where,

$$I_S(\rho) \equiv \int_1^\infty x^{-6} g^{HS}(x) = 0.451\rho^2 - 0.5253\rho + 0.5514. \tag{19}$$

Eq. (19) is applicable for the solid phase with the reduced density $0.95 < \rho\sigma^3 < 1.27$.

1.2.4 Phase Equilibrium Calculations

The chemical potential μ and the osmotic pressure *P* can be derived following standard thermodynamic relations,

$$\mu = \left(\frac{\partial F}{\partial N}\right)_{T,V}. \tag{20}$$

$$P = -\left(\frac{\partial F}{\partial N}\right)_{T,N}. \tag{21}$$

where *V* stands for the total volume. A fluid-fluid coexistence curve is obtained from the criteria of phase equilibrium

$$\mu^{\alpha} = \mu^{\alpha}. \tag{22}$$

$$P^{\alpha} = P^{\alpha}. \tag{23}$$

where α and β represents two different fluid phases. For each temperature, the equilibrium densities ρ_{α} and ρ_{β} are solved using Eqs. (22) and (23). If no solution is found, the temperature is above the critical temperature for fluid-fluid equilibrium; in this case, there is only one fluid phase. For fluid-solid equilibrium, Eqs. (22) and (23) can be used. For liquid phase α, the Helmholtz energy in Eq. (14) and for the solid phase β, Helmholtz energy in Eq. (18) accounts for the fluid-solid phase transition. Again, the, the equilibrium densities ρ_{α} and ρ_{β} can be matched using Eqs. (22) and (23).

1.3 Design and Applications of Mechanically Oscillating PNIPAM Particles

The stimuli-responsive behavior is a temporary action toward an equilibrium state. In contrast, there are many physiological phenomena in our body that continue their own native cyclic changes such as brain waves and the pulsating secretion of hormones. If such self-oscillation could be achieved for gels, many possibilities would emerge for new biomimetic intelligent materials that exhibit autonomous rhythmical motion. Yoshida et al. developed a new design concept for polymer gels which exhibit spontaneous and autonomous periodic swelling and de-swelling changes under constant conditions without on–off switching of external stimuli will be introduced.[44] In the materials design, nonlinear dynamics of chemical reactions and characteristics of gels as open systems play an important role.[45]

The mechanical oscillation of the gel is produced via an oscillating chemical reaction, called the Belousov–Zhabotinsky (BZ) reaction.[46-48] The BZ reaction has a cyclic reaction network similar to the tricarboxylicacid (TCA) cycle which is a metabolic reaction in living systems. The BZ reaction is well known for exhibiting temporal and spatial oscillating phenomena with periodic redox changes of the catalysts in a closed solution. The overall process is the oxidation of an organic substrate such as citric or malonic acid (MA) by an oxidizing agent (bromate) in the presence of a metal catalyst under acidic conditions. Metal ions or metal complexes with high redox potentials (1.0–1.4 volts/standard hydrogen electrode), such as cerium ion, ferroin, or ruthenium tris(2,2'-bipyridine) [$Ru(bipy)_3^{2+}$] are widely used as catalysts. During the BZ reaction, the metal catalyst ion periodically changes its oxidation number to oscillate between the oxidized and reduced states. In a homogeneously stirred BZ reaction, the color of the solution periodically changes due to the redox changes of the metal catalyst. In an unstirred solution BZ reaction, concentric or spiral wave patterns appear in the solution as shown in Figure 1.1.

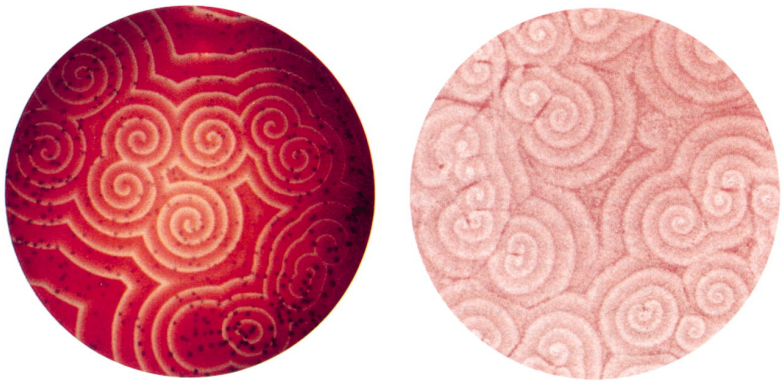

Figure 1.1 Spiral waves in the Belousov–Zhabotinsky reaction (*Left*) and in *D. discoideum* (*Right*).[49]

The significance of the BZ reaction has been recognized as a chemical model for understanding some aspects of biological phenomena, such as glycolytic oscillations or biorhythms,[50] cardiac fibrillation,[51] self-organization of amoeba cells,[52] pattern formation on animal skin,[53,54] visual pattern processing on retina,[55] etc. The chemical oscillation of the BZ reaction is converted into the mechanical changes of gels via direct linking of the polymer chains to the metal catalyst of the BZ reaction as illustrated in the Figure 1.2.

The PNIPAM-co-$Ru(bipy)_3^{+2}$ gel has a phase-transition temperature because of themosensitive constituent NIPAM. The oxidation of the $Ru(bipy)_3^{+2}$ moiety caused not only an increase in the swelling degree of the gel, but also a rise in the transition temperature (Figure 1.3). These characteristics may be interpreted by considering an increase in hydrophilicity of the polymer chains due to the oxidation of Ru(II) to Ru(III) in the $Ru(bipy)_3$ moiety. As a result, it is expected that the gel undergoes a cyclic swelling–deswelling alteration when the $Ru(bipy)_3$ moiety is periodically oxidized and

reduced under constant temperature. When the gel is immersed in an aqueous solution containing the substrate of the BZ reaction except for the catalyst, the substrates penetrates into the polymer network and the BZ reaction occurs in the gel. Consequently, periodical redox changes induced by the BZ reaction produce periodical swelling–deswelling changes of the gel.[56] The gel has the cyclic reaction network in itself to generate periodic mechanical energy from the chemical energy of the BZ reaction.

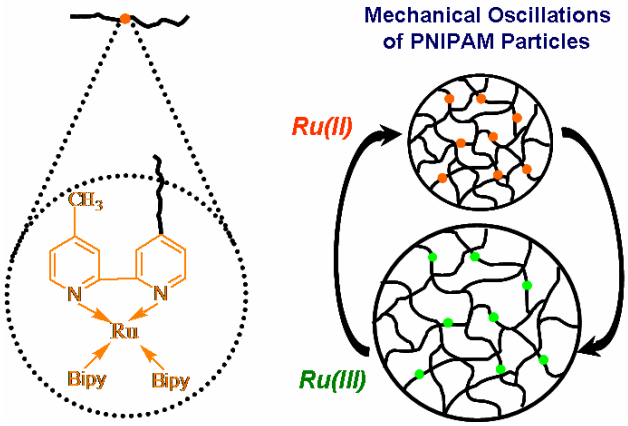

Figure 1.2 Mechanic self-oscillation for PNIPAM-co-Ru(bipy)$_3^{+2}$ gel coupled with the Belousov-Zhabotinsky reaction.

The cubic PNIPAM-co-Ru(bipy)$_3^{+2}$ gel (each length of about 0.5 mm) was found to oscillate mechanically when immersed into an aqueous BZ solution containing malonic acid (MA), sodium bromate ($NaBrO_3$), and nitric acid (HNO_3) at constant temperature. Therefore, the redox oscillation takes place with in the Ru(bipy)$_3$ the gel network which periodically changes between reduced and oxidized states. When the gel size smaller than the wavelength of the chemical wave, the redox changes of ruthenium catalyst occurs homogeneously without pattern formation.[57] Due to the redox oscillation of the

immobilized $Ru(bipy)_3^{+2}$, mechanical swelling-deswelling oscillation of the gel autonomously occurs with the same period as for the redox oscillation. The size changes are isotropic and the gel beats as a whole, like a heart muscle cell. The gel exhibits swelling during the oxidized state and deswelling during the reduced state. The chemical and mechanical oscillations are synchronized without a phase difference.

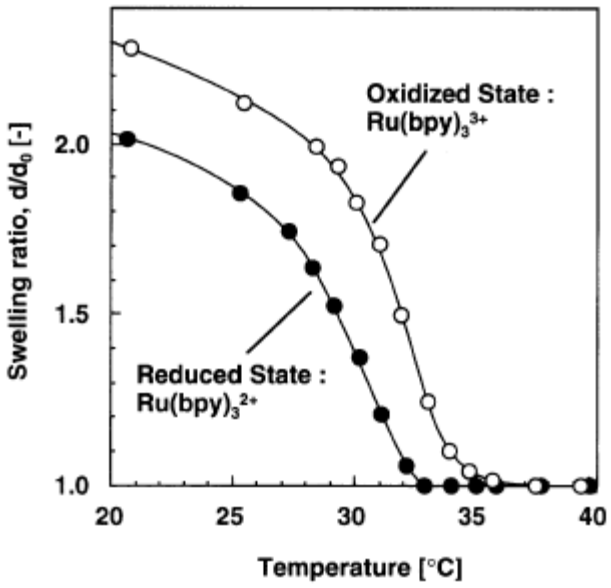

Figure 1.3 Temperature dependence of diameter for PNIPAM-co-$Ru(bipy)_3^{+2}$ gel particles under the conditions of reduced Ru(II) state [in Ce(III) solution] and oxidized Ru(III) state [in Ce(IV) solution].[58]

A rectangular PNIPAM-co-$Ru(bipy)_3^{+2}$ gel (1mm x 1mm x 20 mm) was immersed in an BZ solution containing MA, $NaBrO_3$, and HNO_3 solutions. The chemical waves propagate in the gel at a constant speed in the direction of the gel length as shown in Figure 1.4.[59,60]

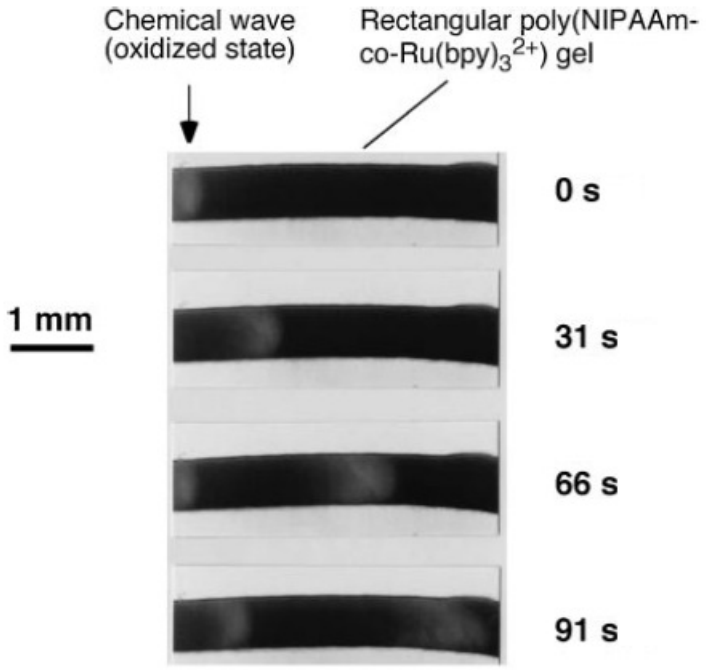

Figure 1.4 Propagation of chemical wave in rectangular PNIPAA-co- $Ru(bipy)_3^{+2}$ gel.[58]

The dark Ru(II) and light Ru(III) zones represent the shrunken and swollen parts respectively of the gel. The locally swollen and shrunken parts move with the chemical wave, like the peristaltic motion of living worms. The propagation of the chemical wave makes the free end of the gel move back and forth at a rate corresponding to the wave propagation speed. As a result, the total length of the gel periodically changes.

A novel biomimetic self-walking gel which is made up of self-oscillating gel was developed by Yoshida et al.[61] Directional movement of gel is produced by asymmetrical swelling–deswelling of the PNIPAM-co-$Ru(bipy)_3^{+2}$ gel. For these purposes, the hydrophilicity of the gel is increased by copolymerizing PNIPAM-co-$Ru(bipy)_3^{+2}$ gel with a third component, hydrophilic 2-acrylamido-2-methylpropanesulfonic acid (AMPS). The monomer solution during the polymerization was added between two different surfaces of plates; a hydrophilic glass surface and a hydrophobic Teflon

surface. Due to the hydrophobicity of $Ru(bipy)_3^{+2}$, it migrates to the Teflon surface side. As a result, a non-uniform distribution along the height is formed by the components, and the resulting the gel strip always bends in the direction of the surface which was facing the Teflon plate during polymerization.

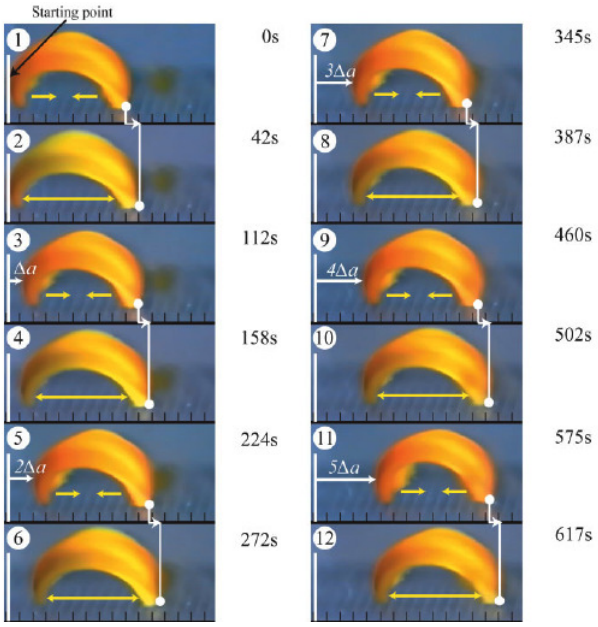

Figure 1.5 Time course of self-walking motion of the gel actuator. During stretching, the front edge can slide forward on the base, but the rear edge is prevented from sliding backwards. Oppositely, during bending, the front edge is prevented from sliding backwards while the rear edge can slide forward. This action is repeated, and as a result, the gel walks forward (the walking velocity: 170 μm/min). Outer solution: MA 62:5 mM, $NaBrO_3$ 84 mM, and HNO_3 0:894 M, 18°C.[61]

A ratchet mechanism was employed to convert the bending and stretching changes to one-directional motion. On the ratchet base, the gel repeatedly bends and stretches autonomously resulting in the forward motion of the gel, while sliding backwards is prevented by the teeth of the ratchet. Figure 1.5 shows forward movement of the self-

walking motion of the gel in the BZ substrate solution under constant temperature. The period of chemical oscillation and the velocity of the gel actuator was approximately 112 s, and 170 μm/min, respectively. The velocity of the gel can be controlled by changing the concentration of substrates in the outer solution.

A two dimensional close-packed array of thermo-sensitive microgel beads was prepared by double template polymerization.[62] First, a 2D colloidal crystal of silica beads with 10 μm diameter was obtained by solvent evaporation. This monolayer of colloidal crystal can serve as the first template for preparation of macroporous polystyrene. The macroporous polystyrene trapping the crystalline order was used as a negative template for fabricating a gel bead array (Figure 1.6). The fabrication method demonstrated was so versatile, and this method may be a key technology to create new functional surface.

A rapid swelling-deswelling response during the BZ reaction can be achieved by introducing porosity into the PNIPAA-co- $Ru(bipy)_3^{+2}$ gel membrane.[63] A closely packed 3D colloidal silica crystal is used as a template to obtain the periodically ordered PNIPAM-co-$Ru(bipy)_3^{+2}$ gel membrane with an interconnecting porous structure (Figure 1.7). If the porous gel precisely maintains the fine structure of the precursor colloidal crystal, the dynamic movement can be observed quantitatively through the structural color based on the reflection from the photonic bandgap in the gel. Because of its unusual and complex photochemical properties of ruthenium, the amplitude and the period of the gel membrane can also be controlled by illumination with visible light. Hence, photo-regulated worm like motion of the gel can be achieved by light irradiation.

The operating conditions for the self-oscillation are limited to conditions under which the BZ reaction occurs. For practical applications, it is necessary to design a self-

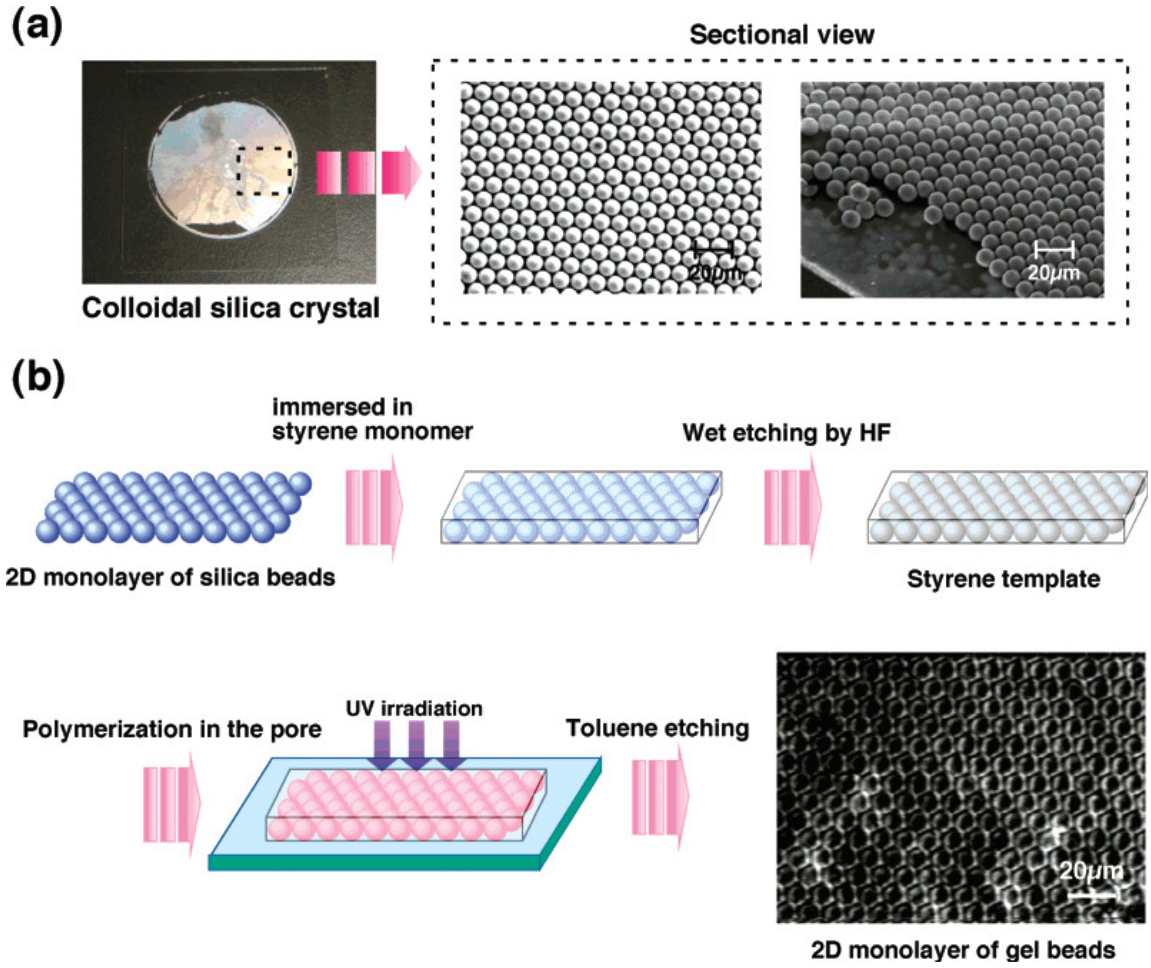

Figure 1.6 Preparation method for the ordered array of 2-D microgel beads. (a) Photograph and SEM images of the obtained silica colloidal crystal. (b) Fabrication process of a 2D monolayer of gel beads by the double-template polymerization method.[63]

oscillating polymer which acts under biological environments. The acid media such as nitric acid or sulfuric acid was substituted by directly incorporating a sulfonic acid group into the polymer.[64,65] The strong oxidant bromate was replaced with another compound that releases bromate ions through ion exchange.[66] For this purpose either 2-acrylamido-2-methylpropanesulfonicacid (AMPS) or Methacrylamidopropyltrimethylammonium-

chloride (MAPTAC) were incorporated into PNIPAM-co-Ru(bipy)$_3^{+2}$. Therefore, the self oscillations in the in porous PNIPAM-co-Ru(bipy)$_3^{+2}$ gels can be achieved without using strong acid or oxidizing agents.

1.4 Mechanism of the BZ Reaction: The Oregonator Model

The reactants for the simple BZ reaction are malonic acid (MA), Sodium bromate, Cerium (IV) sulfate and sulfuric acid. The original FKN (Richard J. Field, Endre Koros, and Richard M. Noyes) mechanism for the BZ reaction consists of 80 elementary steps in which the metal cation, cerium oscillates between +3 to +4 and *vice versa.*[47] Below is the overview of some of the key steps in FKN mechanism:

(1) $BrO_3^- + 5\,Br^- + 6\,H^+ \longrightarrow 3\,Br_2 + 3\,H_2O$

(2) $HOBr + Br^- + H^+ \longrightarrow Br_2 + H_2O$

(3) $BrO_3^- + Br^- + 2\,H^+ \longrightarrow HBrO_2 + HOBr$

(4) $Br_2 + MA \longrightarrow BrMA + Br^- + H^+$

(5) $2Ce^{+3} + BrO_3^- + HBrO_2 + 3\,H^+ \longrightarrow 2Ce^{+4} + 2\,HBrO_2 + H_2O$

(6) $2\,HBrO_2 \longrightarrow HOBr + BrO_3^- + H^+$

(7) $6Ce^{+4} + MA + 2\,H_2O \longrightarrow 6Ce^{+3} + HCOOH + 2\,CO_2 + 6\,H^+$

(8) $4Ce^{+4} + BrMA + 2\,H_2O \longrightarrow 4Ce^{+3} + Br^- + HCOOH + 2\,CO_2 + 5\,H^+$

(9) $Br_2 + HCOOH \longrightarrow 2Br^- + CO_2 + 2\,H^+$

In the above reaction mechanism, bromide (Br^-) reduces the bromate (BrO_3^-). This reaction is fast, quickly using up the available bromide. Once bromide drops to a critical level, bromous acid ($HBrO_2$) takes over the reduction of bromate in a reaction that auto catalytically produces more bromous acid (step 5). This leads to exponential growth in $HBrO_2$. This is eventually checked by a reaction that converts $HBrO_2$ to HOBr and

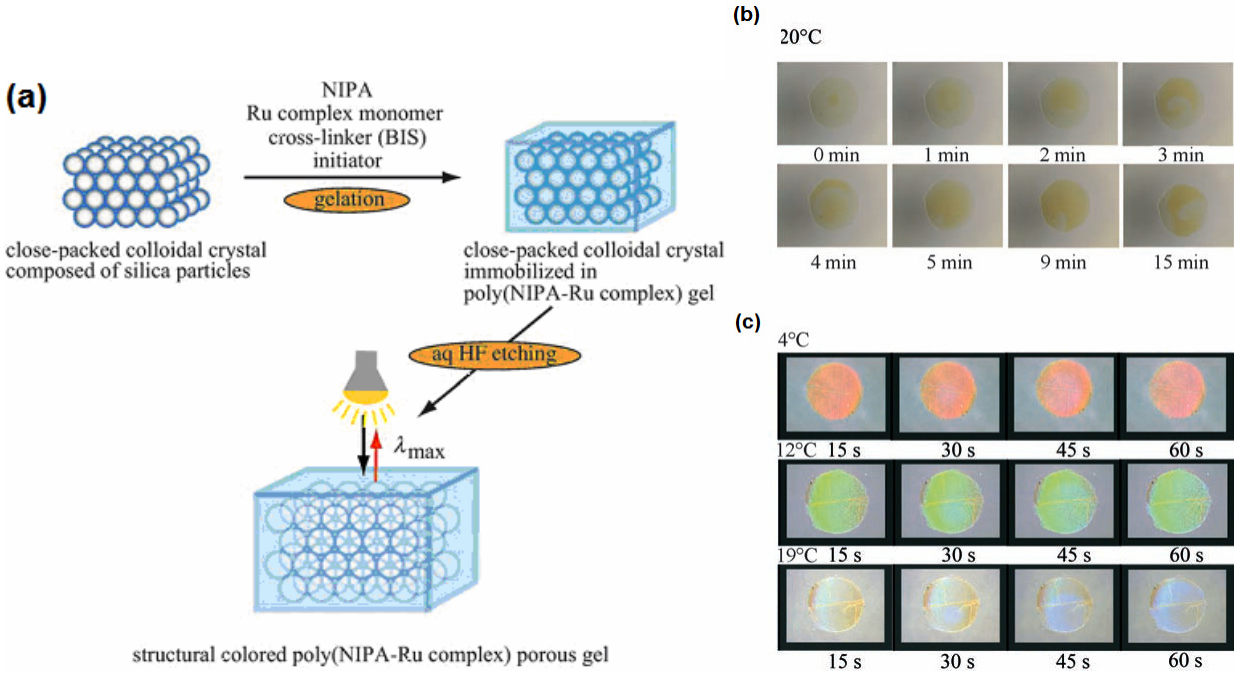

Figure 1.7 Three dimensional periodically ordered porous PNIPAM-co-Ru(bipy)$_3^{+2}$ gel. (a) Preparation scheme of a periodically ordered interconnecting porous PNIPAM-co-Ru(bipy)$_3^{+2}$ gel using a closest-packing colloidal silica crystal as a template. Spatiotemporal color patterns of oscillating behavior for a (b) bulk porous PNIPAM-co-Ru(bipy)$_3^{+2}$ gel, and for a (c) porous PNIPAM-co-Ru(bipy)$_3^{+2}$ gel. The pictures show the time change in the pigment color of the bulk gel and the structural color of the porous gel during the BZ reaction at several temperatures. The BZ reaction solution (20 mL) containing malonic acid (0.0625M), sodium bromate (0.084M), and nitric acid (0.890M) was used.[63]

bromate (step 6). The rate limiting steps (7), (8), and (9) reduce Ce^{+4} to Ce^{+3} and simultaneously increase bromide concentration. Meanwhile, the decomposition of malonic acid [$CH(COOH)_2$] in step 4 results in the reduction of bromine to bromide, nearly restoring the initial concentration of bromide. Once the bromide concentration is high enough, it reacts with bromate and HOBr in (1) and (2) to form bromine, and the process begins again. The two ionization states of the cerium produce two different absorption spectra and the change can be viewed by a color change from yellow to clear and vice versa.

The simpler version of the reaction model, namely the Oregonator model, can reproduce the essential characteristics of the reaction.[67,68] It used three composition variables, five irreversible reaction steps controlled by five rate constants and a stoichiometric factor, f (which is proportional to the ratio between the average number of bromide ions produced and the number of Ce^{4+} ions consumed during the malonic acid oxidation step).

The five equations that are representative of over all BZ reaction are,

$$A + Y \xrightarrow{k_1} X + P$$
$$X + Y \xrightarrow{k_2} 2P$$
$$A + X \xrightarrow{k_3} 2X + 2Z$$
$$2X \xrightarrow{k_4} A + P$$
$$B + Z \xrightarrow{k_5} \frac{1}{2} fY$$

$$X = [HBrO_2]$$
$$Y = [Br^-]$$
$$Z = [Ru(III)]$$
$$A = [BrO_3^-]$$
$$B = [CH_2(COOH)_2]$$
$$P = [HOBr]$$

The classical three dimensional Oregonator consists of the following kinetic equations:

$$\frac{dX}{dt} = k_1 H^2 AY - k_2 HXY + k_3 HAX - 2k_4 X^2 \qquad (24a)$$

$$\frac{dY}{dt} = -k_1 H^2 AY - k_2 HXY + k_5 hBZ \tag{24b}$$

$$\frac{dZ}{dt} = 2k_3 HAX - k_5 BZ \tag{24c}$$

where X = [$HBrO_2$], Y = [Br^-], Z = [Ce(IV)], A = [BrO_3^-], B = [$CH_2(COOH)_2$], H = [H^+], and h = 2*f*. The kinetic rate constants in Eq. (24) are labeled according to their original sequence.

The following dimensionless quantities are defined.

$$x = \frac{X}{X_0},\ y = \frac{Y}{Y_0},\ z = \frac{Z}{Z_0},\ \tau = \frac{t}{t_0},\ a = \frac{A}{A_0},\ \text{and}\ b = \frac{B}{B_0}. \tag{25}$$

With the subscript 0 denotes the reference values,

$$X_0 = \frac{k_3 HA_0}{2k_4},\ Y_0 = \frac{k_3 A_0}{k_2},\ Z_0 = \frac{(k_3 HA_0)^2}{k_4 k_5 B_0},\ t_0 = \frac{1}{k_5 B_0}. \tag{26}$$

Plugging Eqs. (25) and (26) into (24), the kinetic equations become:

$$\varepsilon \frac{dx}{d\tau} = qay - xy + ax - x^2 \tag{27a}$$

$$\delta \frac{dy}{d\tau} = -qay - xy + fbz \tag{27b}$$

$$\frac{dz}{d\tau} = ax - bz \tag{27c}$$

where $\varepsilon = \left(\frac{k_5 B_0}{k_3 HA_0}\right)$, $q = \left(\frac{2k_1 k_4}{k_2 k_3}\right)$, and $\delta = \left(\frac{2k_4 k_5 B_0}{k_2 k_3 H^2 A_0}\right)$

Using the pseudo-steady state approximation for y, i.e., $\delta(T) << \varepsilon(T)$, Eq. (27) is converted into a pair of ordinary differential equations:

$$\varepsilon \frac{dx}{d\tau} = -fbz\left(\frac{x-aq}{x+aq}\right) + ax - x^2 \tag{28a}$$

$$\frac{dz}{d\tau} = ax - bz \tag{28b}$$

The above equations can be solved for x and z.

1.5 Organization of the Dissertation

The dissertation is organized as follows. In Chapter II a novel technique has been developed to determine the freezing-melting boundaries of the thermo-sensitive neutral PNIPAM-co-acrylic acid microgel particles in the temperature-concentration plane. In addition, the phase behavior of the charged PNIPAM-co-acrylic acid has been investigated by tuning the inter-particle potential of the particles. Chapter III provides details of the automatic size oscillations of PNIPAM particles in coupling to a nonlinear chemical reaction, the Belousov-Zhabotinksy reaction. The BZ reaction characteristics such as the oscillatory frequency, induction time, and the oscillation amplitude are analyzed as a function of initial substrate concentrations. Then, the temperature dependency of the BZ reaction has been compared between polymer-immobilized and free ruthenium catalyst BZ reactions in Chapter IV. The overall activation energies of the BZ reaction are calculated for both induction and oscillatory phases. In Chapter V, the temperature response of the two-variable Oregonator model is investigated. The prediction of the temperature dependency of the BZ reaction response from the model is correlated to the experimental findings. This analysis provides insights into the role of temperature and can be extended to some biological oscillators. Finally, conclusions are presented in Chapter VI, together with projects in progress.

CHAPTER II
DETERMINATION OF FREEZING-MELTING BOUNDARIES OF POLY(N-ISOPROPYLACRYLAMIDE) GEL PARTICLES*

2.1 Synopsis

Phase boundaries for thermo-sensitive colloids are determined by UV Vis spectroscopy as an alternative to the time consuming sedimentation method. The Bragg attenuation peak from colloidal crystallites was monitored during the quasi-equilibrium colloidal crystal melting. The melting and freezing boundaries of the coexistence region were determined via a blue-shift of Bragg's peak and the disappearance of peak area. This method is demonstrated for poly(N-isopropylacrylamide) (PNIPAM) particles at different charge densities and temperatures far below the lower critical solution temperature. At low pH, the particles were neutral and behave as thermo-sensitive hard spheres, and at high ph, the PNIPAM particles behave as thermo-sensitive charged spheres.

2.2 Introduction

Colloidal suspensions are vital model systems for the investigation of not only the structure and dynamics of fluids, crystals, and glasses, but also the phase transitions between them.[37,69-71] Colloids are directly analogous to atoms and are advantageous to study owing to their larger sizes and hence slower diffusion rates. They can be visualized by microscopy methods[72-74] or analyzed using light scattering techniques.[31,75,76] Although hard-sphere like colloidal suspensions were the primary

---

*Reproduced with permission from the *Journal of Colloid and Interface Science,* **2008**, *317,* 96-100.

focus of crystal nucleation studies,[77-82] the crystallization kinetics and phase behavior of aqueous dispersions of PNIPAM particles have attracted increasing attention in recent years. Recently, the crystallization kinetics and phase behavior of aqueous dispersions of PNIPAM particles have attracted increasing attention,[83] partly due to their easier manipulation of volume fraction by changing local environmental conditions.[84-86]

Until now, the primary method for phase boundary analysis was carried out via sedimentation.[37,69,78] A suspension in the fluid and crystal coexistence region is analyzed over a period of time. The crystals are allowed to grow and settle under gravity. The height of the fluid-crystal interface is used to determine the crystallinity produced by the phase transition.[78] However, gravity also concentrates the suspensions and subsequently grows a thin layer of crystals at the fluid-crystal interface.[37] Thus a major drawback of this method is the extremely long time duration, weeks or even months, required for the measurement of thin layer growth in order to extract the effect of gravity. A more prompt method for analysis of phase boundaries and crystallization kinetics has been brought forth using UV-vis spectroscopy, where a small density difference between the PNIPAM colloidal particles and the medium elongated the sedimentation time.[31,75] However, that study did not determine the melting temperatures, and thus left the coexistence region undefined; the hard sphere interation between particles is therefore still an assumption. Yodh et al. found premelting of the crystals at grain boundaries and dislocations within the colloidal crystals where they utlized temperature responsive PNIPAM particles, viewed under real time video microscopy.[87] In this work, the fluid-crystal phase boundaries were probed by UV-vis. spectroscopy in a more time-efficient manner than the aforementioned sedimentation method. The present work is an extention to the previous measurements of phase boundaries by UV-vis spectroscopy.[88]

2.3 Experimental Section

All Chemicals were purchased from Sigma-Aldrich. N-isopropylacrylamide (NIPAM) (97% purity) was re-crystallized from 1:5 (v:v) toluene and n-hexane mixture. All other chemicals were used as received. The PNIPAM microgel samples containing 5 mole % of either acrylic acid or allylamine were prepared by precipitation polymerization. The following reagents were mixed in a three-neck flask and stirred for 1 hour at 300 rpm using a mechanic stirrer under nitrogen purge: 240 mL deionized (DI) water, 3.78 g N-isopropylacrylamide (NIPAM) monomer and 0.12 g acrylic acid (AA) as co-polymer, 0.0665 g methylene-bis-acrylamide (MBA) as cross-linker, and 0.106 g sodium dodecyl sulfate (SDS) as a surfactant. The reaction was initiated by adding a 0.166 g portion of potassium persulfate dissolved in 10 mL of degassed DI water and allowed to run for 4 hours at 70 ºC. The polymer suspension was then purified via dialysis against DI water for a week at room temperature, with the DI water changed twice per day. The molecular weight cut off of the dialysis membrane is 10000 kDa. The hydrodynamic diameter measured by dynamic light scattering (DLS) for dilute sample is 253 nm at pH 3.0 and at 23°C. The pH of the particle suspension was first changed to an appropriate value, followed by centrifugation at 30000 g for 2 hours at 34 °C. The particles were then re-dispersed in DI water having same pH to that of concentrated suspension. Four concentrated samples with pH values 2.80, 3.50, 3.90 and 4.20 were first made and using which, crystals were formed under different concentrations at coexistence region. The weight percentage of each sample was obtained by drying out the solvent completely.

A fiber optic UV-vis spectrometer EPP2000 (StellarNet Inc., Tampa, Florida), a halogen light source with an SL1 filter, and a temperature-controlled cuvette holder from Quantum Northwest (QNW, Spokane, Washington), were used for sample analysis. SpectraWiz software was used for spectra acquisition. To avoid water condensation inside the cuvette holder at lower temperatures, a nitrogen gas purge setup, equipped

with a Rego twin-gauge regulator and a ChemGlass air-free bubbler for visual flow rate observation, was employed.

The laboratory temperature was maintained at approximately 22 ºC. Visual observation of the samples provided a good basis for the freezing point estimation. To avoid shear melting, each sample was heated to a temperature at which only the fluid phase was seen, whereupon a reference spectrum was taken. Then, the cuvette temperature was maintained well below the estimated melting temperature for several hours so that the sample is fully crystallized and equilibrated. Beginning at this low temperature, the cuvette temperature was slowly increased in the increments of 0.25 ºC, allowing 30 minutes to equilibrate after each step. A UV-vis transmission spectrum was recorded at each temperature. With the fluid references taken well above the freezing temperatures for each sample, an intense Bragg attenuation peak evolves as crystallites form. As temperature was increased in measured increments, the Bragg peak started to shrink until it fully disappeared at or below the fluid reference temperature.

2.4 Results and Discussion

2.4.1 Determination of Freezing-Melting Boundaries of PNIPAM Colloidal Suspensions

The spectra gathered at different temperatures for a specific sample was compiled and overlaid on a single plot of transmittance versus wavelength using OriginLab 7.5 (Northampton, MA). Figure 2.1 plots the data for charged PNIPAM-co-allylmine spheres with pH=7.4. Most relevant to the determination of the melting and freezing points for the suspensions are the decrease in the peak integration and the blue-shift of the Bragg diffraction as temperature increases (Figure 2.2). Determination of the freezing point exploits the change in peak area (integration) as a function of temperature, which is plotted in Figure 2.2a. The Bragg peak area was calculated by fitting two Gaussian peaks to each spectrum and the value for the integration of the sharp, narrow

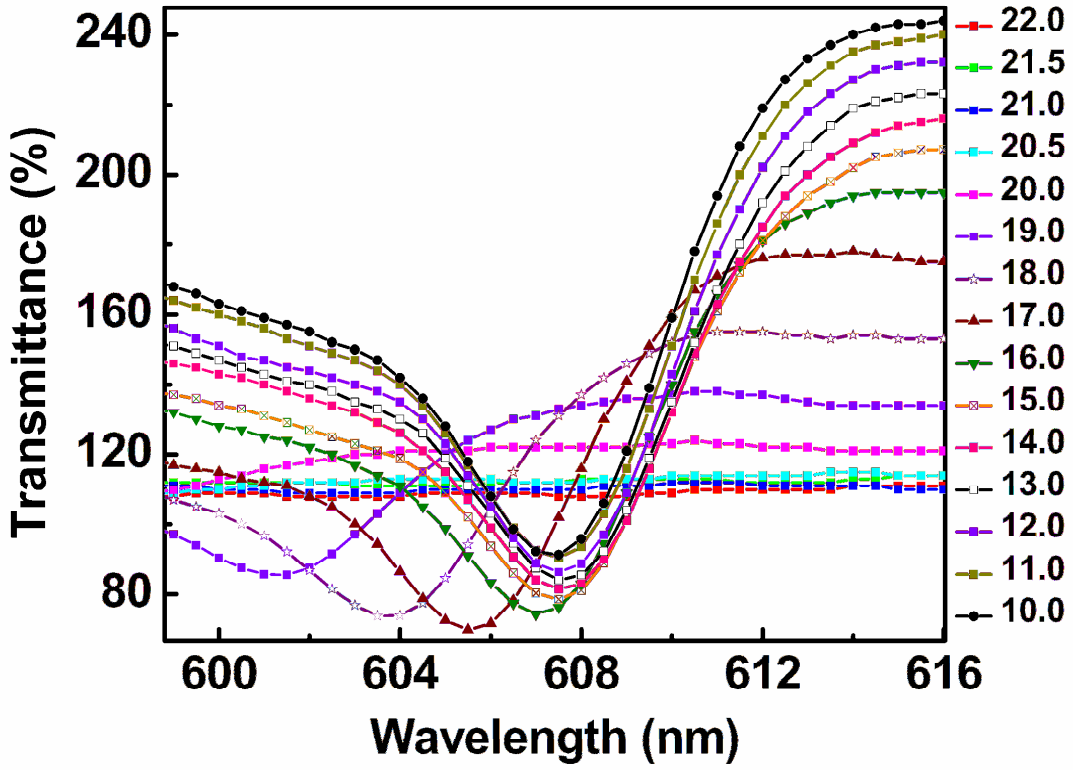

Figure 2.1 UV-vis transmission spectra of the PNIPAM-co-allylamine microgel dispersions of pH=7.4 at different temperatures. With a fluid reference at 22º C, the Bragg peak blue-shifts and disappears with the melting of crystallites.

peak is used in Figure 2.2a, which indicates that the freezing point is located between 20ºC and 20.5ºC. By fitting the data on both sides to a linear and third order polynomial line, the freezing point is calculated to be at their intersection, 20.2 $\pm$ 0.1ºC. Notice that the area is not linearly dependent on temperature in the coexistence regime because the volume fraction of the suspension is not linearly dependent on temperature. The melting point determination utilizes the temperature responsive shrinkage of the PNIPAM particles and the resulting blue shift of Bragg scattering as the particles move closer. The peak position is described by the dynamic diffraction theory.[89]

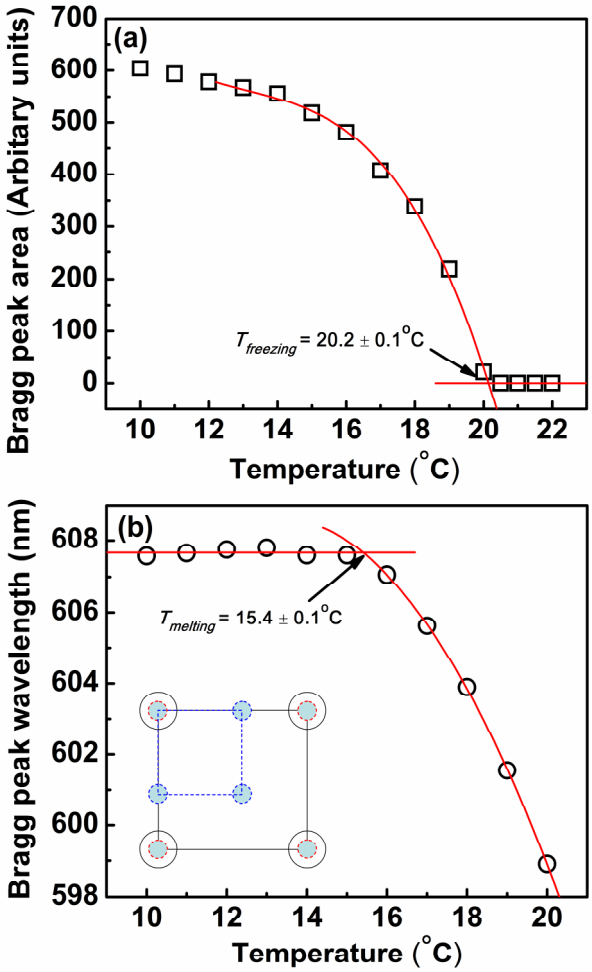

Figure 2.2 Determination of phase boundaries using PNIPAM-co-acrylic acid by UV-vis spectroscopy (a) Area of the Bragg peak. The Bragg peak disappears completely when the last of the crystallites has melted. Intersection of the two trend lines yields the precise melting temperature. (b) Wavelength of the peak position. The Bragg peak begins to shift to a lower wavelength as the crystallites begin to melt. The precise melting point is shown to be at the intersection of the two trend lines. The particles move closer when the crystallites melt as illustrated by inset diagram.

$$\lambda_b = \frac{2n_{water}\sin\theta}{\left(h^2+k^2+l^2\right)}\left[1+\frac{\psi_0}{2\sin^2\theta}\right]\left[\frac{2\pi}{3\varphi}\right]^{1/3} D. \tag{29}$$

where n is the refractive index of the suspension, ψ_0 is photonic scattering strength of the particles, which is almost zero due to the high porosity of the hydrogels. D is the diameter of the colloidal particles, ϕ is the volume fraction of the particles inside the crystallites, θ is the averaged Bragg angle, and h,k,l are the indices of the scattering plane. Considering the quasi-equilibrium nature of the melting and the random orientation of the crystallites, the average scattering angle can be assumed to be the same as the temperature increases. Figure 2.2b shows that the melting point separates two distinct behaviors of the crystallites, i.e. the retaining of a constant Bragg peak position at lower temperatures and the strong blue-shifting right above the melting point.

Below the melting temperature, no crystallites were melted even though the particle diameter is reduced. Because all particles shrink simultaneously, the relative positions among the particles remain constant. Hence, $\phi \propto D^3$, which leads to

$$\lambda_{b,below\ melting} = A\frac{D}{\varphi^{1/3}} = \text{Constant.} \tag{30}$$

where,

$A = \frac{2n_{water}\sin\theta}{(h^2+k^2+l^2)}\left[1+\frac{\psi_0}{2\sin^2\theta}\right]\left[\frac{2\pi}{3}\right]^{1/3}$, which is a constant for the same sample.

On the contrary, the particle volume fraction of the crystallites inside the coexistence regime is constant, $\varphi_{crystal,coexistence} = \varphi_{crystal\ melting}$. Therefore,

$$\lambda_{b,above\ melting} = A\frac{D}{\varphi^{1/3}} = A\frac{D}{\varphi_{melting}^{1/3}} \tag{31}$$

As illustrated by the inset of Figure 2.2(b), as crystallites melt, the further shrunken particles (red positions) need to move closer (blue positions) to maintain the proper osmotic pressure of the crystallites. This close-packing motion creates tighter lattice planes, hence shorter Bragg scattering wavelength. When the crystallites begin to melt, the peak begins to shift; this point is taken as melting point. In a similar manner to the freezing point determination, the intersection of a linear trend line to the left and a second degree polynomial trend line to the right of these temperatures yields a precise melting temperature of 15.4 $\pm$ 0.1 ºC.

Figure 2.3a plots the determined transition temperatures versus polymer concentration for PNIPAM-co-acrylic acid particles at pH=2.8. Using the precise melting and freezing temperatures, an accurate depiction of the phase diagram for PNIPAM particles was provided far below their lower critical solution temperature, which is around 34^{o}C. Following a horizontal path across the diagram, the width of the coexistence region was determined to be approximately 7% relative to the freezing concentration at room temperature. This value is consistent with hard sphere boundaries with 5% polydispersity in size.[5,90] The polymer concentration was converted into the corresponding volume fraction for PNIPAM hard spheres at room temperature by calibrating the particle volume fractions at the freezing transition to be 49.4% (Figure 2.3b). The corresponding diameter of the particles with temperature is shown in the inset. The diameter of the particles used were in agreement with the dynamic light scattering measurement of the particles. To investigate the interaction between the particles, we systematically change the pH of PNIPAM-co-acrylic acid suspension. Figure 2.4 plots the relative width of the coexistence region at room temperature as a function of pH. The width increases from pH 2.8 to 3.9 and then decrease upto pH 6.5 for PNIPAM-co-acrylic acid spheres. With pH rise, the particles are physically charged up. An initial increase and then decrease for the relative width is observed. The initial increase in the width is due to the increase in the debye length of the particles and the decrease in the width after 3.9 is due to the increase in the charge of the particles.

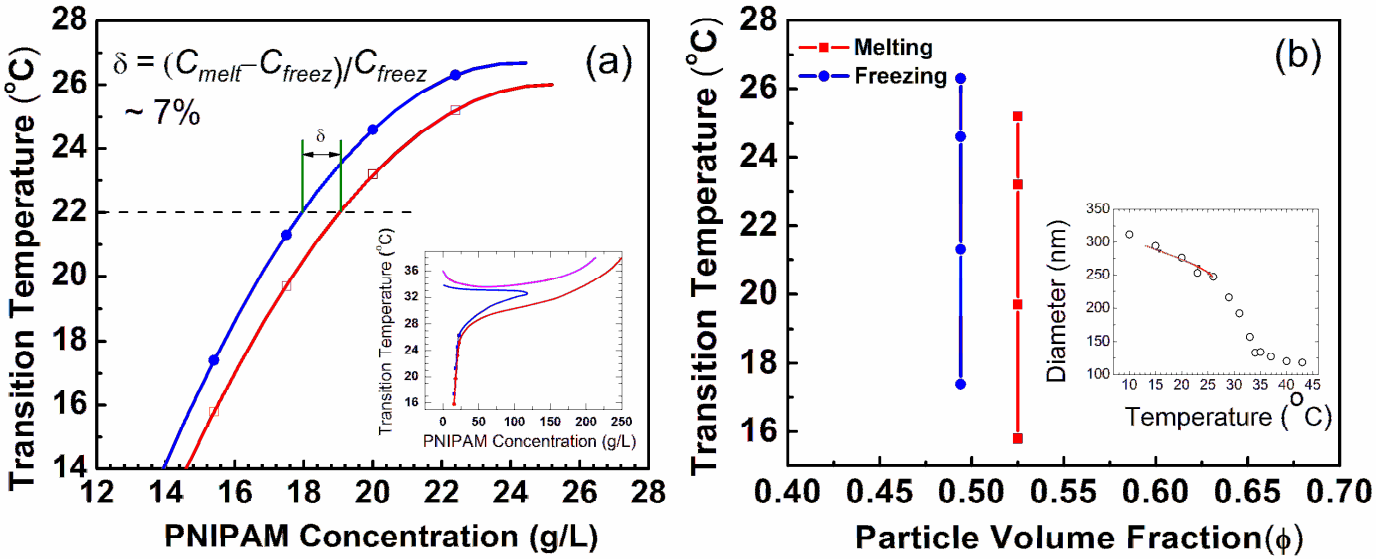

Figure 2.3 Phase diagram of the PNIPAM-co-acrylic acid microgel dispersions at pH=2.8 measured via UV-vis spectroscopy. a) Temperature-concentration representation. At room temperature, the fluid-crystal transition width normalized to the freezing transition concentration is approximately 7%, consistent with hard sphere models with 5% polydisperisity. Inset: Illustration of the phase diagram in a broader concentration and temperature range. b) Temperature-particle volume fraction φ representation. Inset: Particle diameter with temperature (open circles are dynamic light scattering measurement). Red solid line indicates the diameter of the particles used to transfer from temperature-concentration representation to temperature-volume fraction representation.

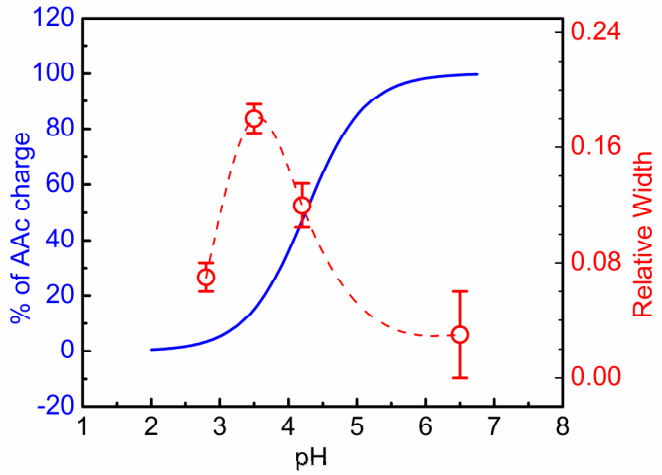

Figure 2.4 Plots of acrylic acid dissociation (solid line) and relative width of coexistence region (dotted line) normalized to the freezing concentration as a function of pH at room temperature.

2.4.2 Phase Behavior of Charged PNIPAM Spheres

The size of the charged PNIPAM spheres measured by dynamic light scattering as a function of temperature is shown in Figure 2.5. The volume phase transition is between 30 - 34°C. The line in the graph is merely a guide to the eye. Below the volume phase-transition temperature, the PNIPAM dispersion exists as a clear liquid at low polymer concentration, and a crystalline solid at high polymer concentration. Above the volume transition temperature of the microgel particles, the sample appears turbid due to the phase transition, where no crystals are observed. Figure 2.6 plots the experimental phase behavior of hard and charged PNIPAM spheres on temperature-concentration plane. The surface charge of PNIPAM particles are controlled by varying pH of the microgel dispersions. At pH 2.80, all the acid groups in the acrylic acid are protonated and the PNIPAM particles acts as hard spheres. At a higher pH of 4.20, the acrylic acid is 50%

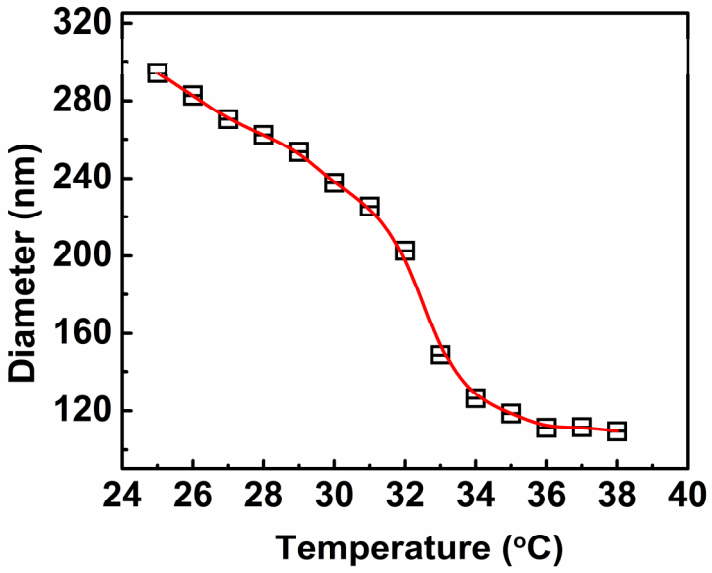

Figure 2.5 Diameter of charged PNIPAM spheres at pH 4.20, determined by the dynamic light scattering measurements for different temperatures.

dissociated and the PNIPAM particles behave as soft spheres.

Figure 2.6a show the experimental equilibrium phase behavior of charged PNIPAM particles, and the phase diagram of PNIPAM hard spheres calculated by perturbation theory is graphed in Figure 2.6b. For hard PNIPAM spheres, the coexistence region is extended up to a concentration of 250 g/L, whereas the coexistence region spans up to a concentration of 28 g/L. The experimental phase diagram for charged spheres is different to that of hard spheres, in the sense that the particles crystallize at lower volume fractions. The movement of the coexistence region towards lower concentrations is due to the increase in the Debye length of the particles. The effective diameter of the charged spheres can be calculated from equation (30) along the melting curve of the coexistence region. The diameters obtained from the experiments are being compared to that of hard spheres in Figure 2.7. The data from the Figure 2.7 is suggestive of less degree of shrinkage for charged spheres at high temperatures. As the particles shrink at higher

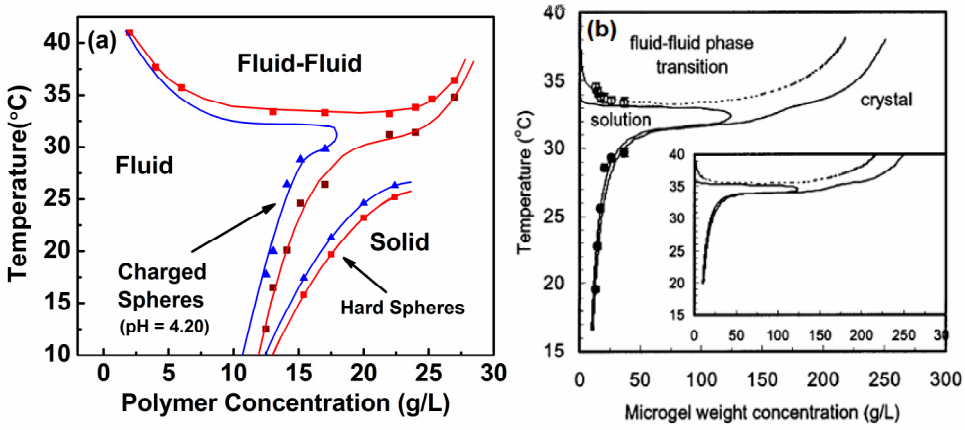

Figure 2.6 The equilibrium phase diagram of thermo-sensitive PNIPAM colloids. (a) Experimental phase behavior of charged PNIPAM particles probed by UV Vis spectroscopy, and (b) Prediction of phase diagram of hard PNIPAM spheres from the thermodynamic perturbation theory.[31]

temperatures, the surface charge density on the particles increases to a much higher degree, resulting in the high Debye length compared to those at lower temperatures.

The future work investigates into the application of perturbation theory to interpret charged spheres phase behavior. Prediction of phase equilibrium with the perturbation theory requires calculating osmotic pressure (π) and Gibbs free energy (G), as functions of volume fraction (ϕ), for both fluid and solid states. The hard sphere diameter is being replaced by the effective diameter for the charged spheres.

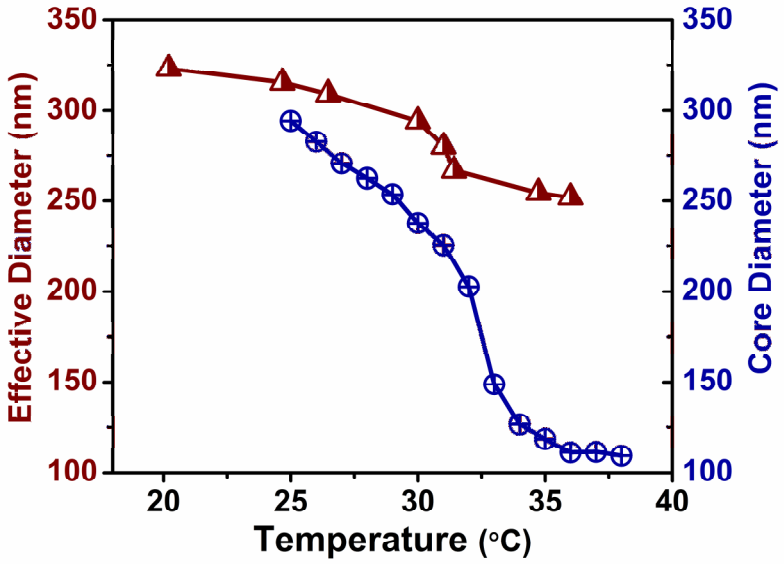

Figure 2.7 Comparison of diameters between hard and charged PNIPAM spheres at different temperatures.

2.5 Conclusions

A critical technique was developed in this chapter to characterize the melting and freezing temperatures for a PNIPAM microgel dispersions using UV-visible transmission spectroscopy. This method provides an accurate and time-efficient method of phase boundary analysis for temperature-sensitive polymers, and a valuable technique for inter-particle potential characterization. At low pH, the PNIPAM-co-acrylic acid microgel particles behave as thermo-sensitive hard spheres, and at high pH, the particles behave as charged spheres.

The determination of freezing-melting boundaries by UV Vis spectroscopy method can be broadly applicable to “intelligent” colloidal systems in which the effective hard-sphere particle diameter during phase transition is sensitive to control variables such as

temperature, pH, and salt. This method can also offer an analytical tool for direct size measurement for the particles in the coexistence regime if $\phi_{melting}$ and the dominant Bragg scattering angle are determined. For example, we can measure the de-swelling of the hydrogels under osmotic pressure at the fluid-crystal phase transition. The coexistence region for the chaged spheres moved towards lower concentrations, and the effective diameter of the charged particles increases with temperature due to the increase in the charge density.

CHAPTER III
A TERNARY PHASE DIAGRAM FOR THE BELOUSOV-ZHABOTINSKY REACTION INDUCED MECHANICAL OSCILLATION OF INTELLIGENT PNIPAM COLLOIDS*

3.1 Synopsis

Belousov-Zhabotinsky reaction-induced mechanical oscillation of poly(N-isopropyl-acrylamide) (PNIPAM) gel particles was investigated by systematic variation of BZ substrate concentrations. The correlation between the dynamic behavior and substrate concentrations was presented in a ternary phase diagram. The phase diagram shows that the oscillatory and steady state regimes coexist and are separated by a high frequency oscillation band. Dependence of oscillation frequency and induction time on the substrate concentrations was also studied. To achieve size uniformity, these PNIPAM gel particles with covalently-bound tris(bipyridyl)ruthenium(II) were synthesized via the coordination chemistry between a ruthenium complex and the monodispersed PNIPAM gel particles bearing bipyridine ligands. The study of the dynamic behavior of this intelligent colloid is beneficial to the BZ-reaction-facilitated dynamic self-assembly of colloids.

3.2 Introduction

The Belousov-Zhabotinsky (BZ) reaction is a well-known non-linear dynamic chemical system that exhibits fascinating phenomena such as periodic and chaotic temporal oscillations, traveling waves, and Turing structures.[46,47,49,91-95] It includes a series of metal-ion-catalyzed oxidative reactions of organic substrates, such as malonic acid, by an acidified bromate solution. The complex nature of this system, as well as its profound

---

*Reproduced with permission from the *Journal of Physical Chemistry A,* **2007**, *111,* 12081-12085.

significance in understanding the biological oscillators related to some basic aspects of life, have attracted extensive attention from both experimentalists and theoreticians. A detailed chemical mechanism, the Field-Körös-Noyes (FKN) mechanism, was established as the framework for understanding and modeling the complicated phenomena of this system. Recent studies of BZ reactions in a variety of microheterogeneous media,[94,96-99] such as PDMS-separated BZ compartments,[100] water-in-oil microemulsions[98] and catalyst-loaded resin-exchange beads,[97,99,101] have brought insights into the communication and self-organization of large quantities of individual relaxation oscillators through the concentration of chemicals in the external media, mimicking living systems such as ventricular cells and neurons.[102]

Recently, the BZ reaction has been used to induce mechanical oscillation in polymeric systems to mimic biological materials.[57,103] Yoshida and his coworkers reported the development of a self-oscillating gel composed of stimuli-responsive poly(N-isopropylacrylamide) (PNIPAM) polymer with grafted tris(bipyridine)ruthenium ($Ru(bipy)_3$) moiety as the BZ catalyst.[104-109] The schematics of the mechanical oscillation of the PNIPAM-co-$Ru(bipy)_3$ microgel particles, induced by the BZ reaction, is shown in Figure 3.1. The actual FKN mechanism consists of many BZ reaction intermediate species; however, only a few of those are shown in the scheme. Initially, the metal catalyst ruthenium (II) is in the reduced state (orange color), and the gel particles remain in the shrink state. With the introduction of BZ substrates, after some time, and during the rest of the induction time, ruthenium switches to its oxidized form, ruthenium (III) (green color). In this state, the microgel becomes swollen. During the oscillatory stage, the gel exhibits rhythmic volume changes. It was found that the chemical oscillation induced a periodic volume oscillation in the PNIPAM gel. This discovery stimulated our interest in the study of colloidal interactions coupled with BZ oscillations, with the long-term goal being to control colloidal self-assembly. Currently, ubiquitous domain defects pose great challenges to the fabrication of large colloidal crystals. We envision that these defects can be annealed by the introduction of

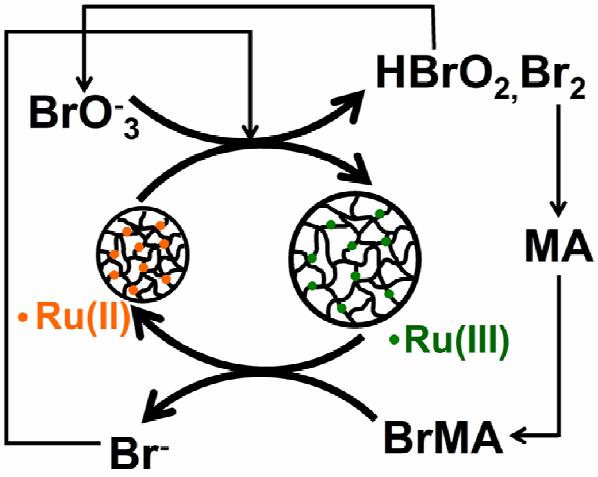

Figure 3.1 Schematics of the mechanical oscillation of PNIPAM particles loaded with $Ru(bipy)_3$.

controlled autonomous mechanical oscillations as in the self-oscillating PNIPAM gel particles via the BZ reaction.

It is well known that the BZ reaction can exhibit a variety of dynamic regimes, such as steady state, periodic oscillation, and chaos in both open and closed systems, depending on reagent concentrations and a number of external factors such as temperature, speed of agitation, and flowing rate. As shown by Yoshida and his coworkers, factors such as temperature and substrate concentrations not only turn on or off of the Hopf bifurcation, [60,66,110,111]but also control the frequency and magnitude of the mechanical oscillation of the self-oscillating gel. For the practical application of the self-oscillating microgels to colloidal crystal annealing, it is therefore important to identify the main 'tuning knobs' for self-assembly, and understand the interplay between the polymer system and the BZ reaction. In this study,[112] we focused our attention on controlling the oscillation dynamics of colloids by varying the BZ substrate concentrations.

3.3 Experimental Section

3.3.1 Materials

N-isopropylacrylamide (NIPAM) (Aldrich, 97%) was purified by recrystallization from 1:5 (v:v) toluene and n-hexane mixture. 4-vinyl-4'-methyl-2,2'-bipyridine (vmbipy) was synthesized according to a reported procedure.[113] The crosslinking monomer N, N-methylene-bis-acrylamide (Aldrich, 99%), initiator 2,2'-azobis-(amidinopropane) dihydrochloride (V50) (Sigma-Aldrich, 97%), and emulsifier cetyltrimethylammonium chloride (CTAC) (Aldrich, 25 wt%) were used as received.

3.3.2 Preparation of Poly(NIPAM-co-Ru(vmbipy)(bipy)$_2$) Particles

Since the size uniformity of the colloid particles is essential for crystallization,[5,114,115] we prepared the PNIPAM particles with covalently-bound Ru(bipy)$_3$ catalyst using an approach different from that of Yoshida[110] and his coworkers (Figure 3.2). First, uniform gel particles of poly(NIPAM-co-vmbipy) were prepared by emulsion polymerization, which crystallize at high a concentration in the proper temperature range. The bipyridyl groups were then converted into Ru(bipy)$_3$ by a subsequent reaction with cis-Ru(bipy)$_2$Cl$_2$. The following synthetic procedure was used.

The copolymer gel particles of poly(NIPAM-*co*-vmbipy) were prepared by emulsion polymerization. Reagents of the following quantities were mixed in a flask at a stirring rate of 350 rpm for about an hour with continuous nitrogen purge: 0.628 gram NIPAM, 0.014 gram MBA, 0.035 gram vmbipy, 3.3 µl CTAC, and 42 ml 50 mM acetic acid buffer (PH at 3.9). The mixture was then maintained in an oil bath at 75°C for 5 minutes. The reaction was initiated with a 2ml aqueous solution of 0.026 gram of V50, and was continued for 6 hours.

The poly(NIPAM-*co*-Ru(bipy)$_2$vmbipy) gel particles were prepared according to the following procedure. 0.080 gram *cis*-RuCl$_2$(bipy)$_2$ (Acros) was dissolved in 120 ml

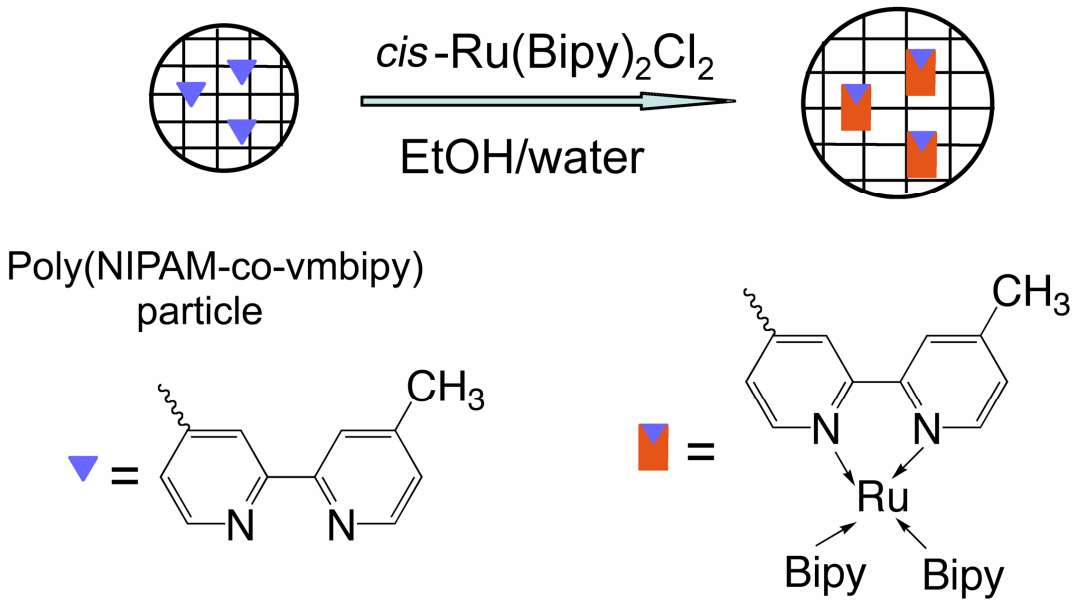

Figure 3.2 Scheme for the preparation of uniform PNIPAM particles with covalently bound $Ru(bipy)_3$ catalyst via coordination chemistry. The uniform poly(NIPAM-co-vmbipy) gel particles, as represented by the checked spheres, are prepared by emulsion polymerization. Subsequent coordination with *cis*-$Ru(bipy)_2Cl_2$ converts the bipy ligand group into $Ru(bipy)_3$ moiety.

ethanol (95%). To this solution was added 20 ml of the poly(NIPAM-*co*-vmbipy) emulsion. The mixture was refluxed under nitrogen for 2 days. The product was purified via dialysis against continuously stirred deionized (DI) water for 6 days at room temperature. The dialysis membrane has a cutoff molecular weight of 10000 kDa.

3.3.3 Characterization of PNIPAM-co-Ru(vmbipy)(bipy)$_2$) Particles

The hydrodynamic diameter (D_h) and size distribution of the PNIPAM particles were characterized by 90 degree dynamic light scattering (DLS) (ZetaPALS, Brookhaven Instrument Corporation, Holtsville, NY) measurements. The experimental setup includes a 35 mW He-Ne laser source (wavelength λ = 632.8 nm) and a Brookhaven digital

correlator BI9000AT. The hydrodynamic diameters for the poly(NIPAM-*co*-vmbipy) and poly(NIPAM-*co*-Ru(bipy)$_2$vmbipy) particles are 386 ± 10 nm and 425 ± 16 nm at 25 ºC, based on ten and fifteen measurements, respectively. The DLS measured polydispersity (PDI) is below 7% for the poly(NIPAM-*co*-vmbipy) particles, and 13% for the poly(NIPAM-*co*-Ru(bipy)$_2$vmbipy) particles, demonstrating good monodispersity for both particles.[83]

A suspension of the poly(NIPAM-*co*-vmbipy) particles was centrifuged at 34ºC and 30000*g* for 2 hours. A hydrogel pellet with strong iridescence was obtained after decantation of the supernatant (Figure-3.3), indicating a very narrow size distribution of the poly(NIPAM-*co*-vmbipy) particles.

The sample of poly(NIPAM-*co*-Ru(bipy)$_2$vmbipy) gel particles for confocal scanning laser microscopy (CSLM) imaging was prepared by sandwiching the predried gel particles (20 hrs, in air) between a micro slide (3×1, Corning) and a cover slip (No. 1, Gold Seal) and subsequent sealing with Scotch tape. A Leica TCS SP5 confocal scanning laser microscope (Leica, NJ) in combination with an argon laser (λ_0 = 488 nm) and an oil-immersion lens (Leica 63X) was operated in both fluorescence and reflectance modes. A scanning speed of 400 Hz was applied. The CSLM images of the poly(NIPAM-*co*-Ru(bipy)$_2$vmbipy) gel particles are shown in Figure-3.4. The fluorescence image (Figure 3.4a) shows discrete poly(NIPAM-co-Ru(vmbipy)(bipy)$_2$) particles with relatively uniform fluorescent emission from the Ru(bipy)$_3$ centers. The reflectance image (Figure 3.4b) shows the particles after natural solvent evaporation. The particles are relatively uniform and ordering was seen in some domains. UV-vis characterization of the PNIPAM particles was conducted by use of a fiber optic UV-visible spectrometer (EPP2000, StellarNet Inc., FL) equipped with SL1 halogen and SL3 Deuterium double light sources and a temperature controlled cuvette holder (Quantum Northwest, WA). The SpectraWiz software was used for spectrum acquisition. The UV-vis spectrum of the poly(NIPAM-*co*-Ru(bipy)$_2$vmbipy) gel particles was compared with those of *cis*-RuCl$_2$(bipy)$_2$, Ru(bipy)$_3$(PF$_6$)$_2$, pure PNIPAM and the poly(NIPAM-*co*-

vmbipy) gel particles (Figure 3.5). The characteristic absorbance peak in the 400–500 nm region corresponds to the metal to ligand charge transfer of the $Ru(bipy)_3$ group, hence convincingly supports the conversion of bipyridyl moiety into $Ru(bipy)_3$ after the coordination reaction.

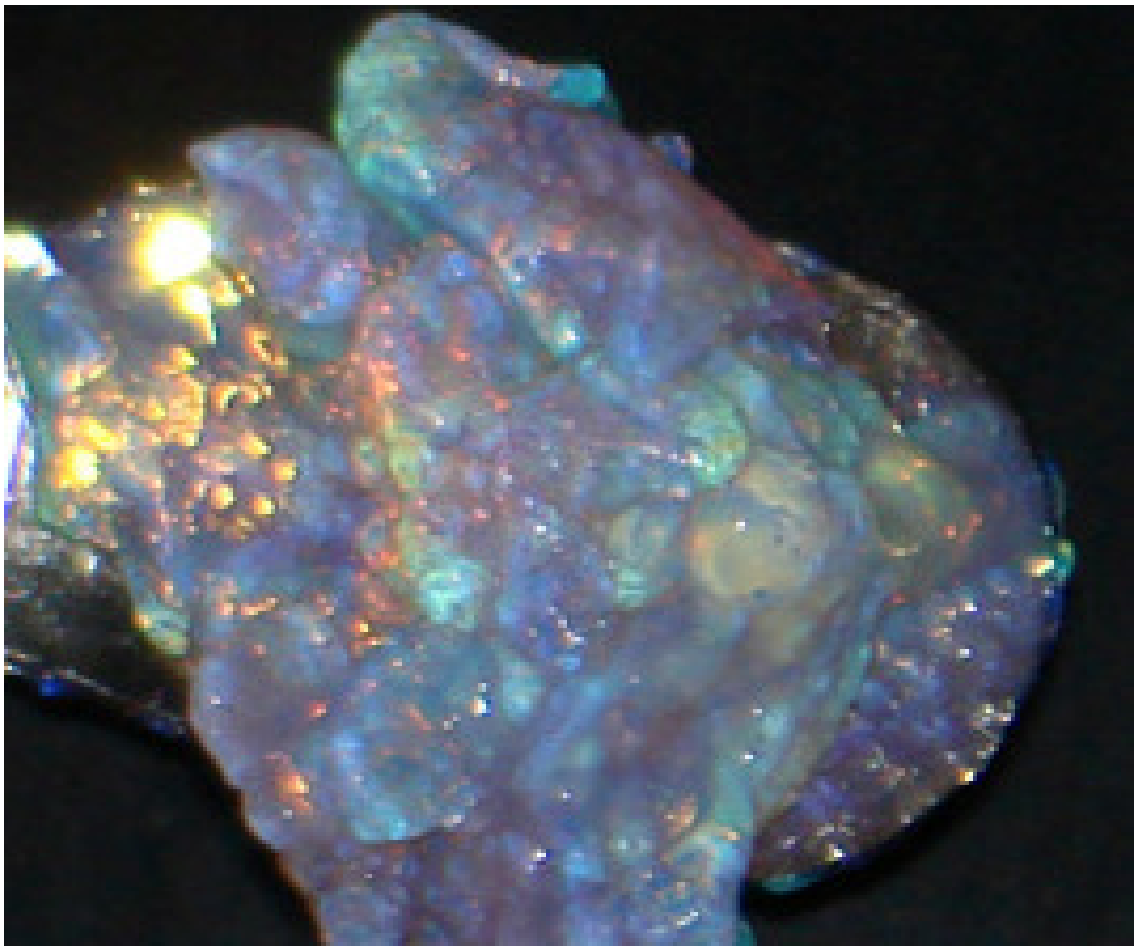

Figure 3.3 A centrifuged pellet of poly(NIPAM-*co*-vmbipy) particles on a spatula. The strong iridescence of the pellet indicates a high degree of size uniformity of the particles.

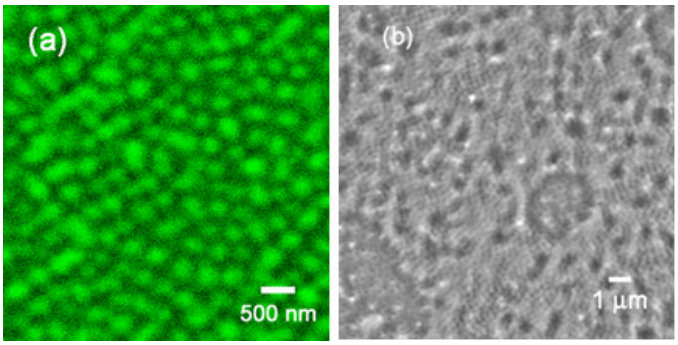

Figure 3.4 Confocal images of the poly(NIPAM-*co*-Ru(bipy)$_2$vmbipy) gel particles measured in (a) fluorescence and (b) reflectance modes (Argon laser $\lambda_0 = 488$ nm). The particles are approximately 300 ~ 400 nm in size.

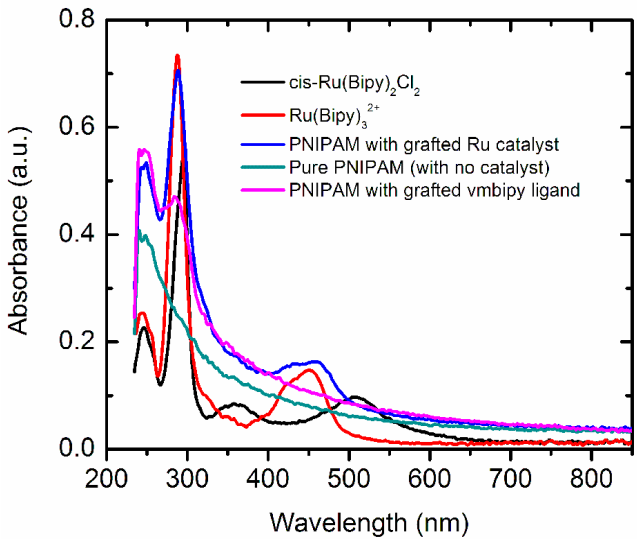

Figure 3.5 UV-vis spectrum of the Poly(NIPAM-*co*-Ru(bipy)$_2$vmbipy) gel particles, in comparison to the spectra of the starting materials and the pure Ru(bipy)$_3^{2+}$ complex. The characteristic absorbance peak in the 400–500 nm region convincingly supports the conversion of bipyridyl moiety into Ru(bipy)$_3$.

The conversion percentage of the bipyridyl groups is estimated based on the UV-vis measurements described below. Figure 3.6a shows the UV-vis absorbance of the poly(NIPAM-*co*-Ru(bipy)$_2$vmbipy) particles after correction of the absorbance from the PNIPAM polymer. The two most intense peaks, at 287 and 452 nms, arise from the π–π^* transition of the bipyridyl group and the metal to ligand charge transfer of the Ru(bipy)$_3$, respectively, with the latter being characteristic to the coordinated bipyridyl group. The intensity ratio between the two peaks was used to quantify the molar ratio between the uncoordinated and coordinated bipyridyl groups.

A series of dilute solutions of 4,4'-dimethyl-2,2'-bipyridine (dmbipy) and Ru(bipy)$_3$(PF$_6$)$_2$ in mixed solvent of ethanol and water (v:v = 6:1) were prepared. The molar concentrations of the solutions are in the range of 10^{-5} and 10^{-6} M. From the UV absorbance vs. concentration working curves, the molar absorption coefficients ($\varepsilon_{L\text{-}282}$) are determined to be 7.9×10^3 L·mol^{-1}·cm^{-1} at 282 nm for the dmbipy ligand, 5.8×10^4 L·mol^{-1}·cm^{-1} ($\varepsilon_{R\text{-}282}$) and 1.3×10^4 L·mol^{-1}·cm^{-1} ($\varepsilon_{R\text{-}452}$) at 282 and 452 nms for the Ru(bipy)$_3$ groups. For a solution of dmbipy and Ru(bipy)$_3$(PF$_6$)$_2$ mixture, the molar percentage of Ru(bipy)$_3$(PF$_6$)$_2$ (P_{Ru}) and the relative intensity of the UV-vis absorbance at 282 and 452 nms (A_{282}/A_{452}), can be correlated using the following equation,

$$\begin{aligned}\frac{A_{282}}{A_{452}} &= \frac{\varepsilon_{L-282}\cdot C_L + \varepsilon_{Ru-282}\cdot C_{Ru}}{\varepsilon_{Ru-452}\cdot C_{Ru}} \\ &= \frac{\varepsilon_{Ru-282}}{\varepsilon_{Ru-452}} + \left(\frac{\varepsilon_{L-282}}{\varepsilon_{Ru-452}}\right)\cdot\left(\frac{C_L}{C_{Ru}}\right) \\ &= \frac{\varepsilon_{Ru-282}}{\varepsilon_{Ru-452}} + \left(\frac{\varepsilon_{L-282}}{\varepsilon_{Ru-452}}\right)\left(\frac{1}{P_{Ru}} - 1\right)\end{aligned} \tag{32}$$

where C_L and C_{Ru} stand for the concentrations of dmbipy and Ru(bipy)$_3$(PF$_6$)$_2$, respectively. A series of solutions with mixed dmbipy and Ru(bipy)$_3$(PF$_6$)$_2$ were prepared at certain molar ratios, and the UV-vis absorbance for these solutions was

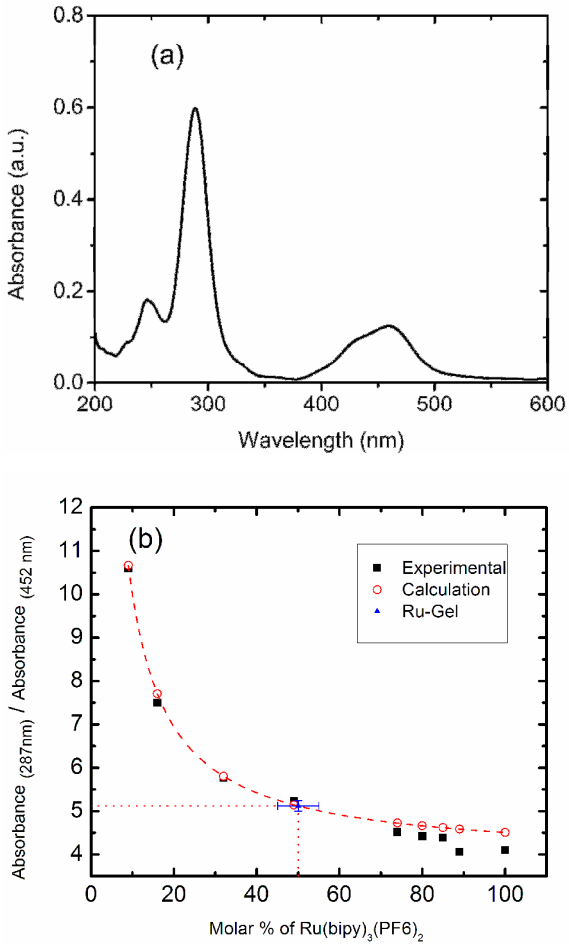

Figure 3.6 Estimation of molar percentage of $Ru(bipy)_3$ on the PNIPAM gel particles. (a) UV-vis absorbance spectrum of the poly(NIPAM-*co*-$Ru(bipy)_2$vmbipy) gel particles. The absorbance from the PNIPAM polymer was corrected for using a reference sample of 0.02 wt% pure PNIPAM polymers in a mixed solvent of ethanol and water. (b) The intensity ratio of the absorbance at 282 nm (A_{282}) and 452 nm (A_{452}) with the change of molar percentage of $Ru(bipy)_3(PF_6)_2$ in a series of mixed solutions of 4,4'-dimethyl-2,2'-bipyridine (dmbipy) and $Ru(bipy)_3(PF_6)_2$. The dashed line was calculated using Eq. (32). The blue triangle denotes the poly(NIPAM-*co*-$Ru(bipy)_2$vmbipy) sample. The molar percentage of the $Ru(bipy)_3$ on the gel particles was estimated to be 50 ± 5%.

measured. The ratios A_{282}/A_{452} from the measurements were plotted against the molar percentages of $Ru(bipy)_3(PF_6)_2$ (Figure-3.6b). Also plotted in Figure-3.6b were the A_{282}/A_{452} values of these solutions calculated using Eq. (32). As shown in Figure-3.6b, the measured and the calculated values agree well at low $Ru(bipy)_3(PF_6)_2$ percentage ($P_{Ru} < 50\%$), but differ more at higher $Ru(bipy)_3(PF_6)_2$ percentage. Overall, this method provides a fairly accurate estimation of the $Ru(bipy)_3(PF_6)_2$ molar percentage for mixtures with low to medium $Ru(bipy)_3(PF_6)_2$ molar percentages. Whereas at higher $Ru(bipy)_3(PF_6)_2$ percentages, the estimation error may be quite high due to the diminishing slope of the function. Assuming the influence of the PNIPAM matrix on the absorbance of the bipyridyl and $Ru(bipy)_3$ groups can be neglected, the molar percentage of $Ru(bipy)_3$ on the poly(NIPAM-*co*-$Ru(bipy)_2$vmbipy) particles, *i.e.*, the conversion percentage of the coordination reaction, can be estimated. With the measured peak ratio A_{282}/A_{452} being 5.1 ± 0.1, the conversion percentage is estimated to be 50 ± 5% from Figure 3.6b.

3.3.4 Measurement of Mechanical Oscillation of Poly(NIPAM-co-Ru(vmbipy)(bipy)$_2$) Particles

Mechanical oscillation of the gel particles during BZ reactions was studied by UV-vis spectroscopy. The UV-vis measurement utilized the aforementioned setup, with the difference that only the SL1 halogen was used for the light source. The poly(NIPAM-*co*-$Ru(bipy)_2$vmbipy) gel suspension and the reactants, including nitric acid, sodium bromate, and malonic acid were mixed in a 4 ml UV-vis cuvette. At controlled temperature and under constant stirring, the transmittance of the mixture was recorded in the episodic data capture mode. The time interval between the episodes is 400 ms and the spectrum spans 190–856 nm. Data acquired was processed using the SwDemo and Origin programs (OriginLab 7.5, Northampton, MA). The oscillation frequency was analyzed using the Fast Fourier Transformation (FFT) algorithm in the OriginLab 7.5 program. For a systematic study, the experiments were conducted at 22 °C and the bulk solution was 0.30 M nitric acid. The original substrate concentrations are as follows:

malonic acid 0.30 M, sodium bromate 0.75 M, and net $Ru(bipy)_3^{2+}$ 1×10^{-4} M. A number of samples with different substrate concentrations were prepared by diluting each of the three original solutions, followed by mixing of the diluted solutions. For each sample, the dilution ratios relative to the original solutions sum to 1. The mixed solution was then loaded in the UV-vis cuvette and the transmittance of the solution with change of time was monitored by UV-vis spectroscopy.

3.4 Results and Discussion

3.4.1 Analysis of Mechanical Oscillation of PNIPAM-co-Ru(vmbipy)(bipy)$_2$) Particles

Uniform self-oscillating microgel particles are produced with a diameter of 425 nm, and with PDI 7%. UV-vis spectroscopy convincingly supported the conversion of bipyridyl moiety into $Ru(bipy)_3$ via coordination chemistry. Confocal scanning laser microscopy showed discrete poly(NIPAM-co-Ru(vmbipy)$(bipy)_2$) particles with relatively uniform fluorescent emission from the $Ru(bipy)_3$ centers. We foresee that this approach can be utilized for preparation of uniform polymer gel particles with different sizes and various catalytic metal centers.

An example chemical and mechanical oscillation profile probed by UV-vis spectrometer is plotted in Figure 3.7. The oscillations at 460 nm and 685 nm represent chemical oscillations due to the redox changes of the ruthenium at the reduced and oxidized states, respectively. The oscillations at the isobestic wavelength 570 nm in Figure 3.7b are due to the mechanical swelling and shrinking of the polymer network, in contrast to homogeneous $Ru(bipy)_3^{+2}$ system, where the transmission spectrum shows no oscillations at 570 nm (Figure 3.7a). This observation confirms that the oscillations at 570 nm for the PNIPAM polymer gels truly arise from the mechanical oscillation of the gel particles induced by the BZ reaction and the chemical and mechanical oscillations are well synchronized in the oscillatory phase. The polymer and the catalyst together act as a chemical-to-mechanical energy transformer, similar to the function of muscles of a

living body. The chemical and mechanical oscillations critically depend on the substrate composition, as also noted by Biosa and Yoshida.[60,91] We were therefore motivated to analyze the concentration dependence of the BZ oscillation in these poly(NIPAM-co-Ru(vmbipy)(bipy)$_2$) particles. Concentrations of the BZ substrates, including malonic acid, $NaBrO_3$, and the PNIPAM polymer with Ru(bipy)$_3$ catalyst, were systematically changed by dilution of the original bulk solutions, as detailed in the experimental section. For practical purposes, we imposed a restriction that the dilution ratios of the three solutions always sum to 1. The dynamic behavior of the samples was monitored by UV-vis spectroscopy. For the oscillating samples, the frequency and induction time were also analyzed.

3.4.2 Dependence of Oscillatory Frequency on Substrate Concentrations

A ternary phase diagram (Figure 3.8) summarizes the concentration dependence of the oscillating behavior in this MA-$NaBrO_3$-Ru(bipy)$_3$ (grafted) system. Each of the three axes on the diagram corresponds to a dilution ratio of a BZ reactant with respect to its original solution. It is clearly shown that the phase diagram can be separated into oscillating and non-oscillating regions, with the oscillating region mostly located in the area where the dilution ratio of $NaBrO_3$ is below 50%. Moreover, there exists a minimum concentration of the Ru(bipy)$_3$ catalyst below which no oscillation was observed. A series of control experiments were conducted in which the grafted PNIPAM polymer suspension was replaced by a Ru(bipy)$_3$$SO_4$ solution with a similar catalyst concentration. The phase diagram of the latter system is overlaid with that of the polymer system (Figure 3.8). The dashed line separates the oscillating and non-oscillating regions for the Ru(bipy)$_3$$SO_4$ catalyzed system. Judging from the similarity between the two phase diagrams, it is clear that the separation between the oscillatory and steady state regimes for the oscillating gel demonstrates the intrinsic Hopf bifurcation in the MA-$NaBrO_3$-Ru(bipy)$_3$ system. The shrinkage of the oscillatory region for the PNIPAM system at high $NaBrO_3$ concentration conditions, relative to the Ru(bipy)$_3$$SO_4$ system, can be accounted for by the colloidal aggregation of the polymer

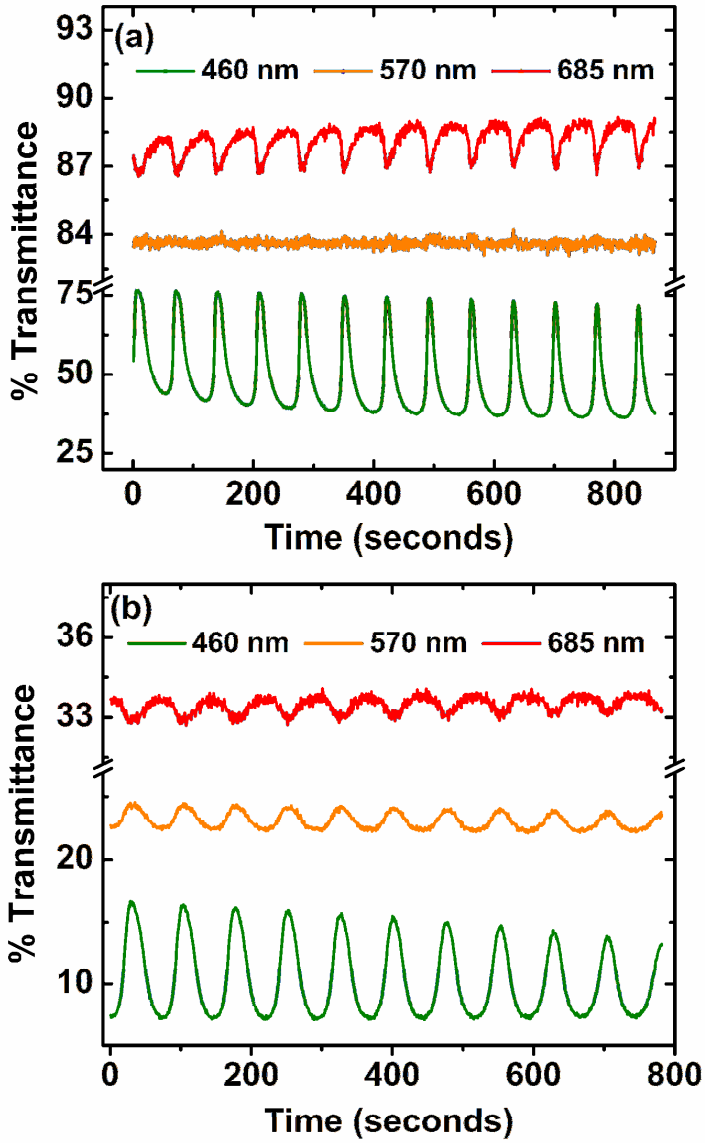

Figure 3.7 UV-vis spectrographs of (a) chemical oscillation of $Ru(bipy)_3$, and (b) mechanical oscillation of PNIPAM loaded with $Ru(bipy)_3$.

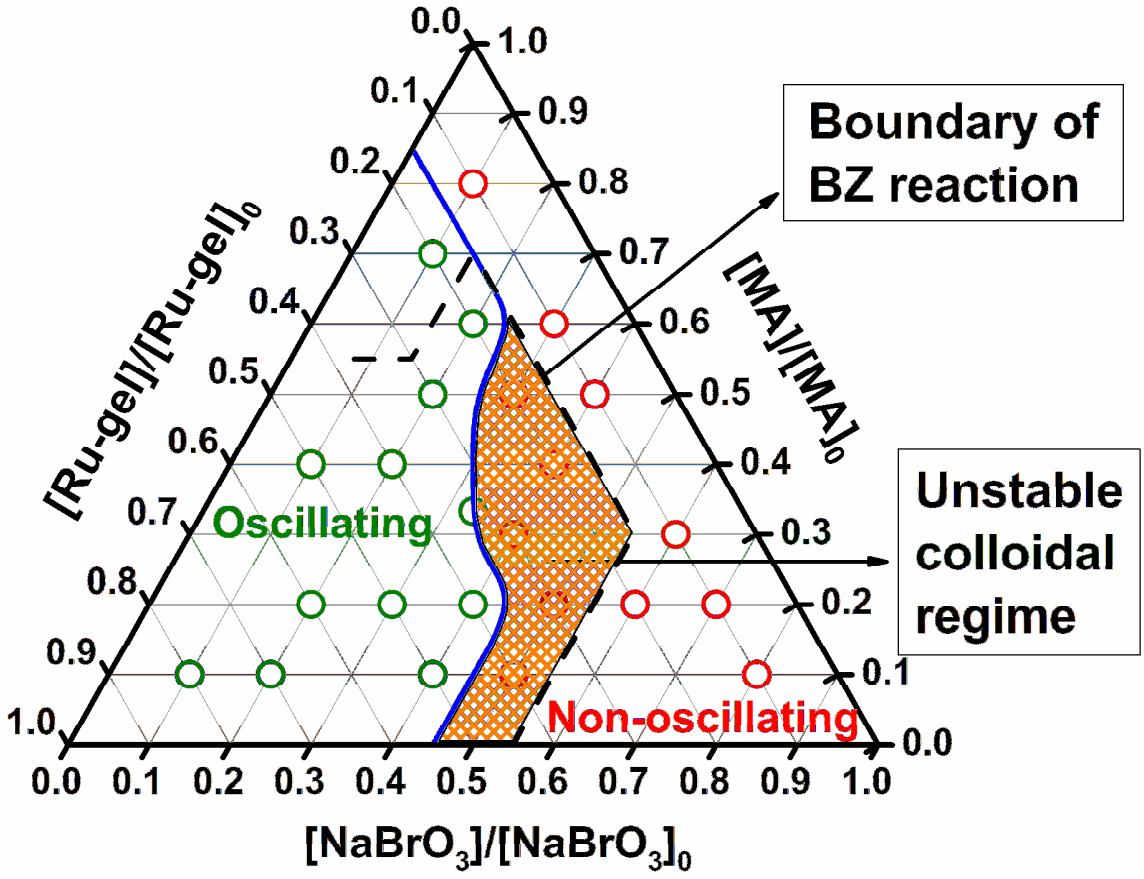

Figure 3.8 A ternary phase diagram for the BZ reaction induced mechanical oscillation of poly(NIPAM-co-Ru(vmbipy)(bipy)$_2$) gel particles with variation of substrate concentrations. The solid line inside the triangle was added for the guidance of the eye to separate the oscillating and non-oscillating regions. The dashed line shows the borderline of the oscillatory-steady state regimes for a control study using non-polymerized Ru(bipy)$_3$SO$_4$.

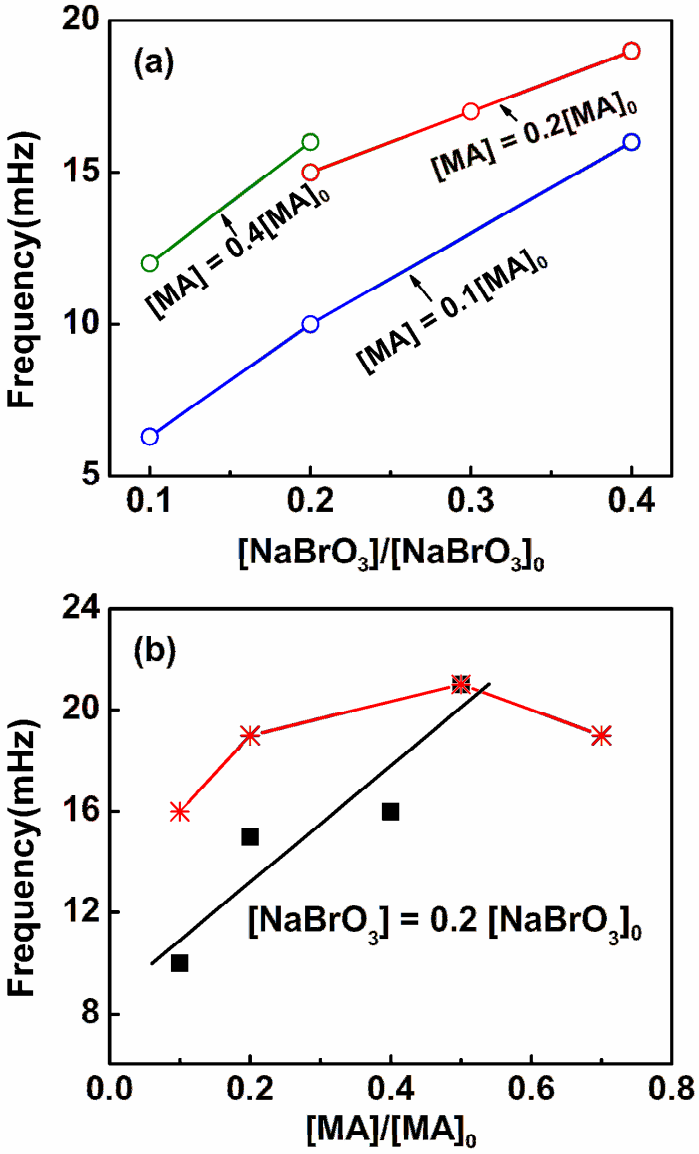

Figure 3.9 Dynamic behavior of BZ reactions in PNIPAM gel particles with covalently-bound Ru(bipy)$_3$. (a) Dependence of oscillating frequency on the sodium bromate concentration. (b) Dependence of oscillating frequency on the malonic acid concentration. Squares denote samples with [$NaBrO_3$] = 0.2 [$NaBrO_3$]$_0$ and stars denote samples near the oscillation, non-oscillation boundary.

gels due to enhanced screening of coulombic interactions and the subsequent increase in the van der Waals attraction. The dependence of oscillation frequency on the malonic acid (MA) and $NaBrO_3$ concentrations is plotted in Figures 3.9a and 3.9b. At constant MA concentrations it was found that the oscillation frequency increases linearly with the $NaBrO_3$ concentration (Figure 3.9a). While at fixed $NaBrO_3$ concentrations, the oscillation frequency increases monotonically with the MA concentration (Figure 3.9b). This trend was fit linearly with a simplified two variable Oregonator model.[48] The correlation between frequency and substrate concentration reported here bears a similar trend with the findings of Yoshida and his coworkers[116] on the poly(NIPAM-co-$Ru(bipy)_3$) gel beads, with the difference that a power law relationship was found in the latter case. We did not use the power law fitting due to the limited data range. Nevertheless, it is interesting to note that the oscillation frequency does not vary much for the samples near the oscillating and non-oscillating borderline (Figure 3.9b). Hence, a high frequency band separates the two dynamic regimes.

3.4.3 Amplitude Analysis of Poly(NIPAM-co-Ru(vmbipy)(bipy)$_2$) Particles

To verify the proposed Hopf bifurcation, we performed an analysis on the oscillation amplitude of transmittance across the ternary phase diagram for three series of samples. They each consisted of several data points on a line parallel to one of the three axes of the ternary phase diagram, *i.e.*, with one of the three substrate concentrations fixed and the other two are allowed to vary. The oscillation amplitude was plotted against one of the variable concentrations. The results are shown in Figure-3.10. In each subdiagram, as the concentration changes, the oscillation amplitude gradually decreases to zero with the system turning from the oscillatory state to stationary state (denoted in the direction of the red arrows). This trend is contrary to that of the oscillation frequency which changes discontinuously across the borderline. Therefore, we conclude that the phase change has the Hopf bifurcation characteristics. Special attention was paid to the pink area on subdiagram 3.10(b), which is a non-oscillatory region arising from the colloidal aggregation at high salt concentration, but not the bifurcation.

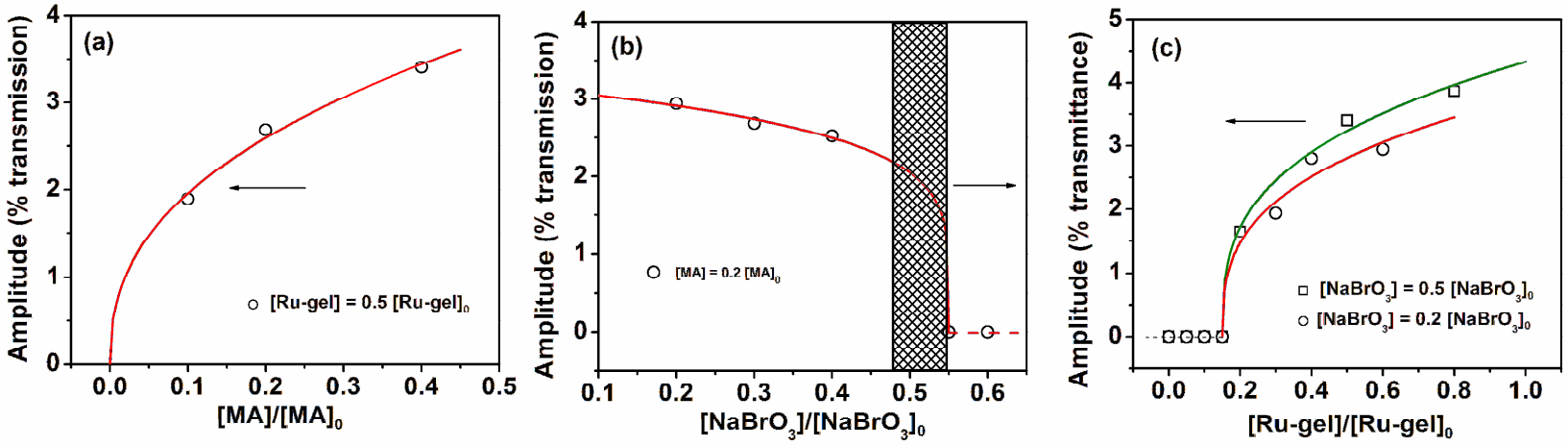

Figure 3.10 Trend of the oscillation amplitude across the ternary phase diagram. In each subdiagram, one substrate concentration was fixed and the other two were variable. The oscillation amplitude of transmittance was plotted against one of the two variable concentrations. The oscillation amplitude decreases continuously to zero as the system progresses from the oscillatory state to the stationary state (noted in the direction of the red arrows). The area of the fill pattern on diagram (b) is a non-oscillatory region due to colloidal aggregation at high salt concentration.

3.4.4 Induction Time of Poly(NIPAM-co-Ru(vmbipy)(bipy)$_2$) Catalyzed BZ Reaction with Substrate Concentrations

More interestingly, we observed that the preoscillatory time, i.e., the induction time, is dramatically longer for the gel supported system when compared to the conventional non-polymerized Ru(bipy)$_3$ system. The dependence of induction time on the MA and $NaBrO_3$ concentrations for the gel supported system is shown in Figure 3.11. Figure 3.11a shows that the $NaBrO_3$ concentration is the predominant factor for determining the induction time at low MA concentration (the MA dilution ratio is no greater than 40%). The induction time increases monotonically with the increase in $NaBrO_3$ concentration, and an approximate exponential correlation can be found. At a fixed $NaBrO_3$ concentration, the induction time remains almost constant when the malonic acid concentration is below 40% of the original, while increases abruptly with the change in malonic acid concentration beyond that critical point (Figure 3.11b). A similar dependence of induction time on the $NaBrO_3$ and malonic acid concentrations was observed for the cerium catalyzed BZ reactions in bulk system. Here, we offer a rather qualitative explanation by pointing out the important inhibition effects to the $HBrO_2$ autocatalysis process. It is known that bromide competes with $HBrO_2$ for bromate and the autocatalysis process would not start until the $[Br^{-}]$ drops to a certain critical value. We assume that an increase in bromate concentration demands longer time for the reduction of $[Br^{-}]$ to the threshold value. Accordingly, an increase in bromate concentration would lead to an increase of induction time. At high $[MA]_0/[BrO_3^{-}]_0$, the effect of another inhibitor, i.e., the organic radicals, MA·, generated by the catalyst, becomes increasingly important, as noted by Field et al.[93] This explains the dramatic increase of induction time with malonic acid concentrations beyond the critical [MA] at a fixed bromate concentration. Overall, BZ reactions catalyzed by the Ru(bipy)$_3$ catalyst immobilized in the responsive gel can be considered as being conducted in nano-sized open reactors. Hence, mass diffusion and the local chemical and mechanical environment of the supporting gel might play very important roles in the chemical kinetics of the reaction. Quantitative studies bring more insights to this system.

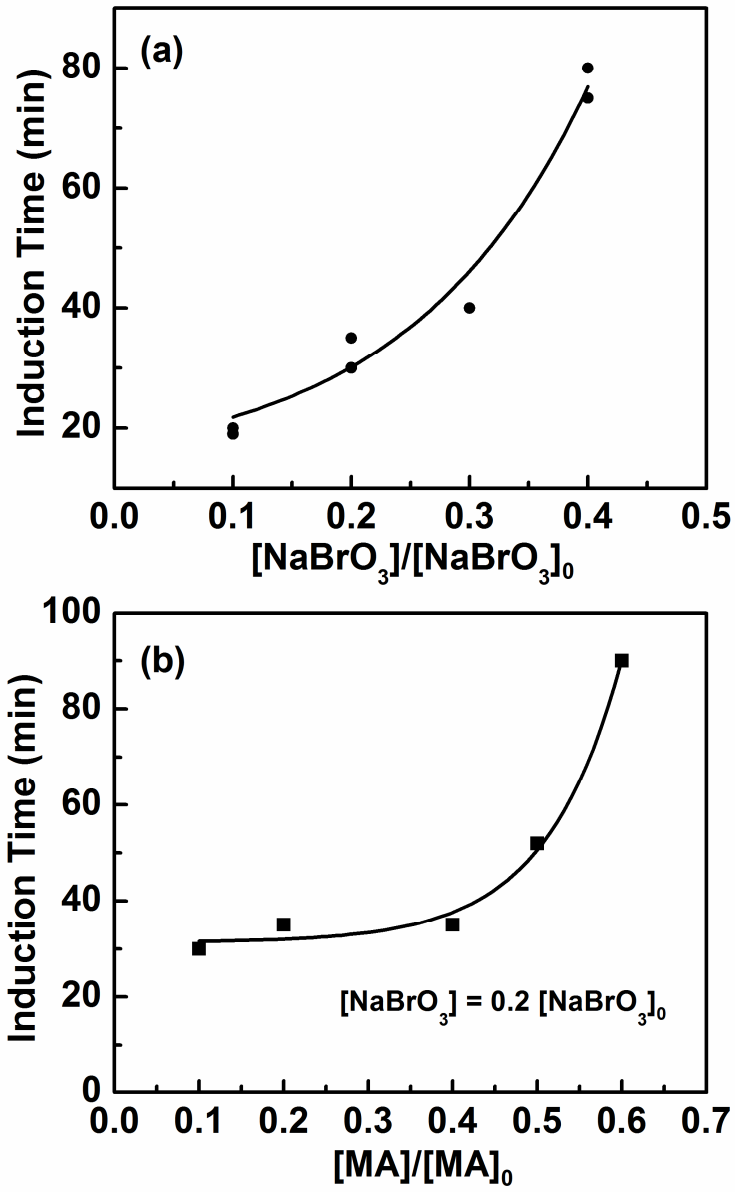

Figure 3.11 Dependence of induction time on the BZ substrate concentrations. (a) Samples with low [MA] ([MA] ≤ 0.4[MA]$_0$). Note that samples at the same [$NaBrO_3$] have different [MA]. (b) Samples with fixed [$NaBrO_3$] ([$NaBrO_3$] = 0.2 [$NaBrO_3$]$_0$.

3.5 Conclusions

A systematic study was presented on the BZ reaction induced mechanical oscillation of PNIPAM gel particles by varying the malonic acid, sodium bromate, and the imbedded $Ru(bipy)_3$ catalyst concentrations. A ternary diagram was created to show the correlation between the dynamic behavior of the system and the substrate concentrations. It was found that the oscillating and steady state regimes coexist on the ternary diagram and are separated by a high frequency oscillation band. The dependencies of the oscillation frequency and induction time on the substrate concentrations were analyzed and tentatively explained by the inhibition effects. This study provides guidance for tuning induction time and frequency, the two important parameters in mechanical-oscillation-facilitated colloidal assembly.

CHAPTER IV
A COMPARATIVE STUDY OF TEMPERATURE DEPENDENCE OF INDUCTION TIME AND OSCILLATORY FREQUENCY IN POLYMER-IMMOBILIZED AND FREE CATALYST BELOUSOV-ZHABOTINSKY REACTIONS*

4.1 Synopsis

Environment-sensitive poly(N-isopropylacrylamide) (PNIPAM) microgel particles with covalently bonded ruthenium(4-vinyl-4'-methyl-2,2'-bipyridine) bis (2,2'-bipyridine) [Ru(vmbipy)$(bipy)_2$] display periodic size changes when placed in Belousov-Zhabotinsky (BZ) reaction substrates. The temperature dependency of the induction time and oscillatory frequency of the BZ reaction in this polymer- immobilized catalyst system were compared to the bulk BZ reaction with the catalyst in the solution phase. Prolonged induction times are observed for the immobilized catalyst, compared with free catalyst, while little difference is observed on the oscillation frequency. The Arrhenius frequency factor calculated using the induction time for the immobilized catalyst BZ reaction is about seven times smaller than that for the free catalyst $Ru(bipy)_3^{+2}$ case. On the other hand, the Arrhenius frequency factors calculated using the oscillatory frequency are almost the same, showing similar reaction kinetics during the BZ oscillations. The tunability of the induction time using a polymer matrix, as we observed here, while maintaining similar oscillatory behavior, should provide a new dimension to control the self-assembling of BZ active particles.

4.2 Introduction

It is well known that temperature has a pronounced effect on the bromide-driven BZ reaction.[117-119] In this paper, the characteristics of the temperature dependent self-oscillations are investigated, *particularly* the induction time of BZ reaction, which is least studied in dilute suspensions of PNIPAM gel particles embedded with ruthenium catalyst. Here, to clarify the factors that influence induction time, experiments are performed between 5°C and 26°C for both the uniform microgel particles loaded with $Ru(bipy)_3^{+2}$ which are prepared by emulsion polymerization, and the normal $Ru(bipy)_3^{+2}$ solutions. Here, the temperature response of the induction and the oscillatory phases of the BZ reaction in both immobilized and free catalyst systems is analyzed by using Arrhenius plots.

The self-oscillating microgels have potential applications in developing smart functional materials that display autonomous response. Examples include self-walking actuator,[61] micropumps with autonomous beating or peristaltic motion,[120] devices for signal transmission utilizing propagation of chemical waves,[63] and oscillatory drug release synchronized with cell cycles or human biorhythms.[56] It is important to understand how proper control over the self oscillations can be achieved.

4.3 Experimental Section

4.3.1 Materials

All chemicals were purchased from Sigma-Aldrich (Milwaukee, Wisc.). N-isopropylacrylamide (NIPAM, 97%) was recrystallized from 1:8 (v:v) toluene and n-hexane mixture. 4-vinyl-4'-methyl-2,2'-bipyridine (vmbipy) was synthesized according to a reported procedure. The crosslinking monomer N, N-methylene-bis-acrylamide (MBA, 99%), initiator 2,2'-azobis-(amidinopropane) dihydrochloride (V50, 97%), and

the emulsifier cetyltrimethylammonium chloride (CTAC, 25 wt%) were used as received.

4.3.2 Preparation and Characterization of Poly(NIPAM-co-Ru(vmbipy)(bipy)$_2$) Particles

Uniform PNIPAM gel particles bearing tris(bipyridyl)ruthenium(II) were synthesized as illustrated in Chapter III. Measured by dynamics light scattering, the hydrodynamic diameters were 386 ± 10 nm for the PNIPAM-co-vmbipy particles, and 425 ± 16 nm for the PNIPAM-co-Ru(bipy)$_3$ particles at 25ºC.

For all comparison experiments, equal concentrations of the initial BZ substrates ($Ru(bipy)_3^{+2}$ (2.5 mM), bromate 0.15 M, and malonic acid 0.09M) were maintained in both immobilized and free catalyst systems. The approximate concentration of $Ru(bipy)_3^{+2}$ (0.0025M) in PNIPAM-co-Ru(bipy)$_3$ suspension was determined by comparing the absorption peak intensities due to $Ru(bipy)_3^{+2}$ at 454 nm (after correcting the absorption due to PNIPAM), with a known concentration of $Ru(bipy)_3^{+2}$ solution. For the solution phase experiments, $Ru(bipy)_3^{+2}$ solution was initially made using solid $Ru(bipy)_3SO_4$ crystals, prepared from commercially available $Ru(bipy)_3Cl_2$.[121] Solutions of 0.3 M malonic acid, 0.75 M sodium bromate, 5 mM $Ru(bipy)_3^{+2}$, and 1.5 wt% of PNIPAM-co-Ru(bipy)$_3$ suspension with about 5 mM net $Ru(bipy)_3^{+2}$ concentration were prepared using 0.3 M HNO_3 solution. The BZ reaction for each catalyst system at various temperatures was performed by mixing 0.6 ml of 0.75 M sodium bromate, 0.9 ml of 0.3 M malonic acid, and 1.5 ml of PNIPAM-co-Ru(bipy)$_3$ suspension (which has a net 5 mM $Ru(bipy)_3^{+2}$ content) or 1.5 ml of 5 mM $Ru(bipy)_3^{+2}$ solution (a total of 3 ml) in a 4.5 ml quartz cuvette, and stirred at 350 rpm. The oscillation frequency and the induction time were measured between 5°C and 26°C with an increment of 2°C for PNIPAM-co-Ru(bipy)$_3$ and 5°C for $Ru(bipy)_3^{+2}$ reaction systems.

Oscillations of the BZ reaction were detected via the transmission changes in a fiber optic UV-vis spectrometer (EPP2000, StellarNet Inc., Tampa, Fla.) equipped with SL1

halogen light source, and a temperature controlled cuvette holder (Quantum Northwest, Liberty Lake, Wash.). SpectraWiz software was used for spectrum acquisition. The transmittance data was recorded in the episodic mode. The time interval between the episodes was 400 ms, and the spectrum spans, 190–856 nm. Data acquired was processed using the SwDemo (StellarNet Inc., Fla.) and Origin programs (OriginLab 7.5, Northampton, Mass.). The oscillation frequency was calculated by the Fast Fourier's transform (FFT) of UV-vis transmission.

4.4 Results and Discussion

4.4.1 Comparison of Induction Time and Oscillatory Frequency at Different Temperatures in Polymer-Immobilized and Free Ruthenium Catalyst BZ Reaction

Uniform self-oscillating microgel particles are produced with a diameter of 425 nm, and with PDI 7%. Two important reaction features are investigated in this paper: (a) oscillation frequency, and (b) induction time, both of which depend critically on the initial concentration of the reagents. Our aim is to understand what factors, such as the catalyst immobilization, presence of the polymer, or adsorption of BZ reaction species, contribute to the increased induction times and how temperature influences the oscillatory and induction phase for PNIPAM-co-Ru(bipy)$_3$ microgels.

The temperature dependency of the oscillation frequency and induction time is obtained from 5^{o}C to 26^{o}C. The oscillation frequency of the BZ reaction in response to the changes in temperatures is observed at 460 nm is shown in the Figure 4.1. For a given temperature, same oscillation frequencies are observed within the experimental error, in both free and immobilized catalyst BZ reaction. The BZ reaction stays much longer time

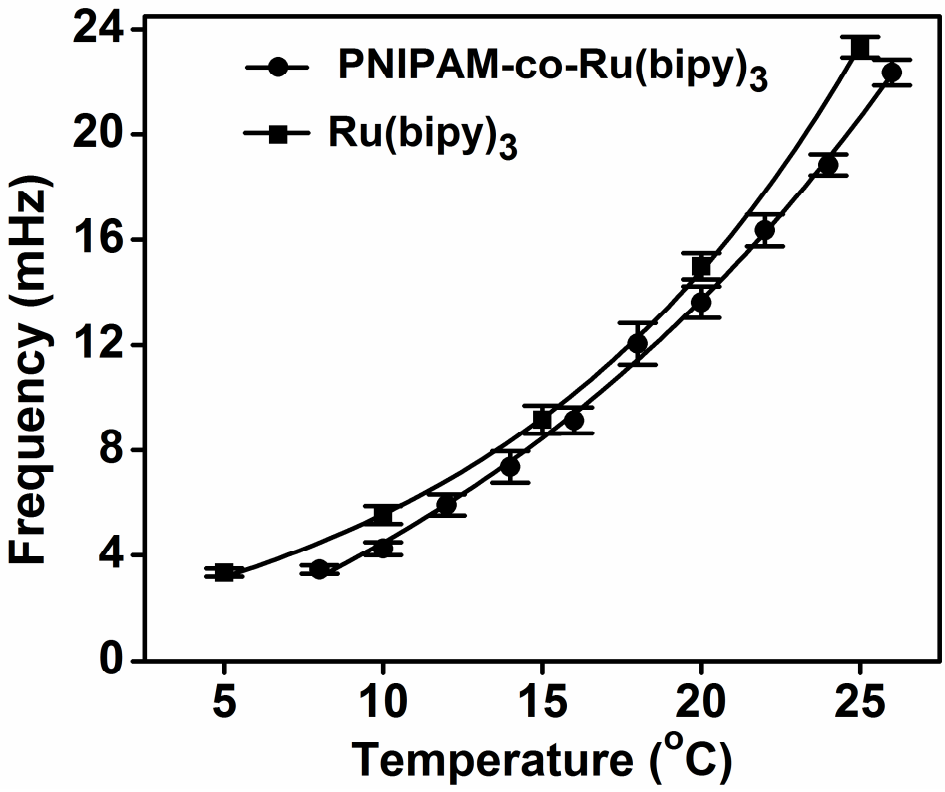

Figure 4.1 The temperature dependence of oscillatory frequency of the mechanical oscillation of PNIPAM spheres with covalently bound $Ru(bipy)_3$ in comparison to the chemical oscillations by $Ru(bipy)_3^{+2}$.

in the reduced state of the ruthenium than in the oxidized state, and the switch between two states is relatively fast. Therefore, the consumption of the bromide ion is the frequency determining step, which is given by the following equation.[122,123]

$$BrO_3^- + Br^- + 2[H]^+ \longleftrightarrow HOBr + HBrO_2 .$$

Even though the reaction kinetics may become slow with the polymer immobilized catalyst (due to the chemical and physical reasons pointed out in the next paragraph), yet

it is not the rate determining step for oscillation frequency because we observed same frequencies in both catalyst systems and the oscillation frequency is not influenced by the interaction of the catalyst with the polymer. At high temperatures, faster bromide ion consumption shrinks the duration of the reduced state, and hence the reaction exhibits high frequency.

Induction time as a function of temperature is plotted in Figure 4.2, which shows a drastic difference between the immobilized and free catalyst systems. For a given temperature, compared with free $Ru(bipy)_3^{+2}$, longer induction times are observed with PNIPAM-co-$Ru(bipy)_3$. In the free catalyst case, ruthenium can directly produce bromide ions (Br^-) by the interaction with bromide containing sources such as bromate ions (BrO_3^-), and hypobromous acid (HOBr) due to its high standard reduction potential.[55,97] Therefore, the BZ reaction quickly returns to the reduced state from an oxidized state, resulting in almost no induction time at room temperatures. In the case of PNIPAM-co-$Ru(bipy)_3$, the chemical bonding of the ruthenium with the polymer possibly lowers its standard reduction potential[116] such that it may not oxidize bromide containing species effectively as it could in the free catalyst BZ solution. Due to a decrease in the standard reduction potential of the ruthenium, the immobilized catalyst BZ reaction might behave similar to those reaction mechanisms observed in cerium or manganese catalyzed reactions, requiring a critical amount of bromomalonic acid (BrMA) for the onset of oscillations.[124] Therefore, the polymer immobilized ruthenium system displays an induction time. In addition, the dramatic increase in the induction time in ruthenium immobilized catalyst BZ reaction can be attributed to the reduced diffusion and local mass transfer of BZ species from bulk to the polymer immobilized catalyst. We elaborate this assumption as follows. According to the GTF model,[93] BrMA is produced mainly by the following reactions. (We used the same notation as used in the original GTF model.)

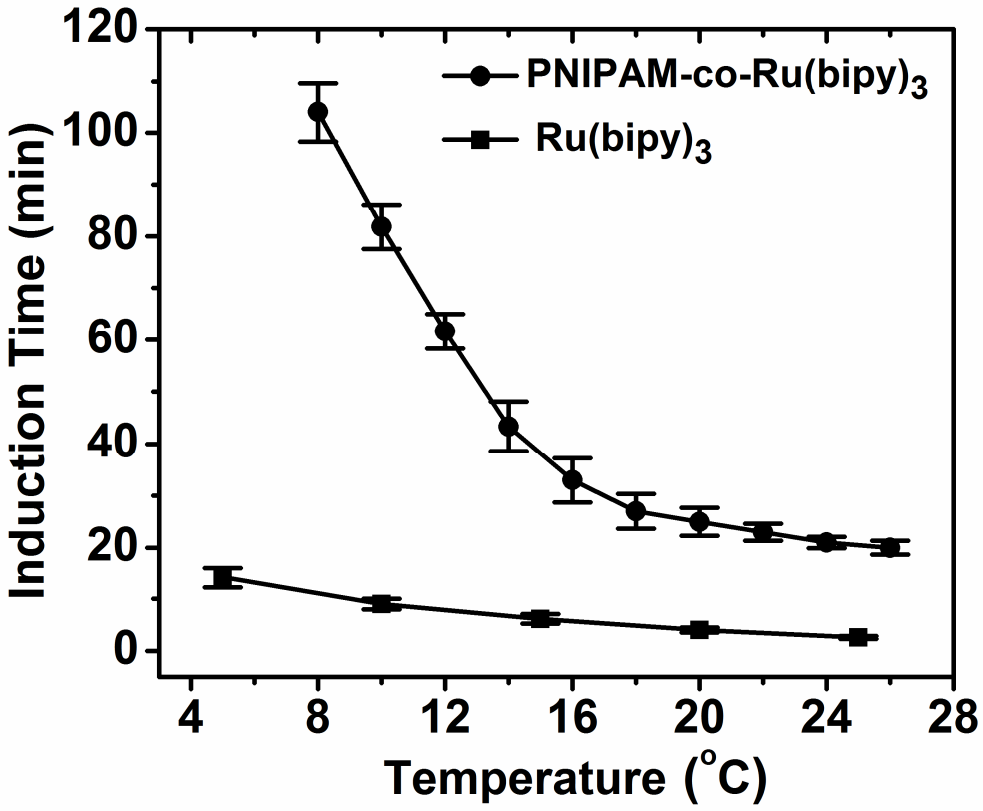

Figure 4.2 Induction time the mechanical oscillation of PNIPAM spheres with covalently bound $Ru(bipy)_3$ in comparison to the chemical oscillations by $Ru(bipy)_3^{+2}$ at various temperatures.

(R1, R2): $HOBr + Br^- + H^+ \leftrightarrow Br_2 + H_2O$

(R5, R6): $BrO_3^- + Br^- + 2H^+ \leftrightarrow HOBr + HBrO_2$

(R15, R16): $MA \leftrightarrow MA(enol)$

(R17): $MA(enol) + Br_2 \rightarrow BrMA + Br^- + H^+$

(R25): $Ru^{3+} + BrMA \rightarrow Ru^{2+} + BrMA^{\circ} + H^+$

(R44): $MA^{\circ} + Br^{\circ} \rightarrow BrMA$

(R26, R45): $Ru^{3+} + MA \leftrightarrow Ru^{2+} + MA^{\circ} + H^+$

(R56): $MA^{\circ} + Br_2 \rightarrow BrMA + Br^{\circ}$

The reactions R25, R26, and R45 involve the use of the catalyst. If the metal catalyst is attached to the crosslinked PNIPAM particles, the diffusion of BZ species from the bulk to the gel phase becomes difficult. The kinetic characteristics of the BZ reaction using immobilized catalyst can be considered similar to those characteristics of immobilized biocatalysts such as enzymes.[125] The reaction rate with immobilized catalyst can be altered considerably by the following effects to cause a difference in the concentrations of some reaction species in the immediate vicinity of the immobilized catalyst: (i) steric effects, due to the hindrance of polymer; (ii) partitioning effects, due to the electrostatic and hydrophobic interactions of the polymers with reaction; and (iii) mass-transfer effects, which resist the reaction species to move from bulk phase to the immobilized catalyst. Therefore, the rates of the reactions R25, R26, and R45 with immobilized catalyst decrease drastically, resulting in much longer induction times. The quantitative nature of these effects in case of immobilized BZ reaction catalyst is yet to be elucidated.

There is an additional temperature influence on induction time due to the temperature sensitivity of PNIPAM microgels. At low temperatures, especially below 15^{o}C, the production of BrMA is significantly delayed due to the slow reaction kinetics.[126] At low temperatures, the PNIPAM microgel particles are well swollen, allowing increased access to the metal catalyst for the BZ reaction substrates to react. In the meantime, the incoming BZ substrates experience a decreased catalyst concentration because of the polymer swelling. We have shown that there exists a minimum concentration of the PNIPAM-co-Ru(bipy)$_3$ catalyst below which no oscillation was observed. Therefore, in addition to the slow reaction kinetics, and reduced mass transport due to the gel network, a decrease in the catalyst concentration due to the swelling at low temperatures might contribute to prolonged induction times.

Another possibility of high induction time is due to gradual reaction of PNIPAM with the acidic bromate to produce bromous acid $HBrO_2$. The continuous production of this

autocatalytic intermediate will retain the BZ system longer in the oxidized state, hence lengthening the induction time. A control experiment was performed in which the BZ reaction system with free catalyst $Ru(bipy)_3^{+2}$ was perturbed by the added PNIPAM gel particles with no covalently bonded catalyst. As shown in Figure 4.3, the free catalyst with added PNIPAM spheres did not alter any of the temperature characteristics of the reaction showing the same frequency and induction time at the same temperature as the free catalyst BZ reaction does. Therefore, the hypothesis of a possible chemical reaction between the polymer and BZ substrates is over thrown by this experiment, which otherwise could influence the induction time.

4.4.2 Measurement of Activation Energies and Collision Factors of the BZ Reaction in Polymer-Immobilized and Free Ruthenium Catalyst BZ Reaction by Oscillatory Frequency and Induction Time

To make quantitative characterization, we plotted BZ reaction oscillations in the Arrhenius format,

$$f = A_i \exp\left(\frac{-E_i}{RT}\right) \tag{33}$$

where f is frequency of oscillations, A_i represents the pre-exponential factor, which is also known as frequency or collision factor and which is equal to the average number of collisions between the reacting molecules. E_i is effective activation energies, R is the gas constant (R = 8.314 J $K^{-1}mole^{-1}$), and T is temperature in Kelvin. The induction time of nonlinear oscillatory reaction might also be interpreted using Arrhenius rate equation,[122,127]

$$1/T_{ind} = A_j \exp\left(\frac{-E_{ind}}{RT}\right) \tag{34}$$

where E_{ind} is effective activation energy for the reactions responsible during induction time. The activation energy obtained from induction time measurement is very likely attributable to a sub reaction system that produces BrMA. Figure 4.4 shows the fittings

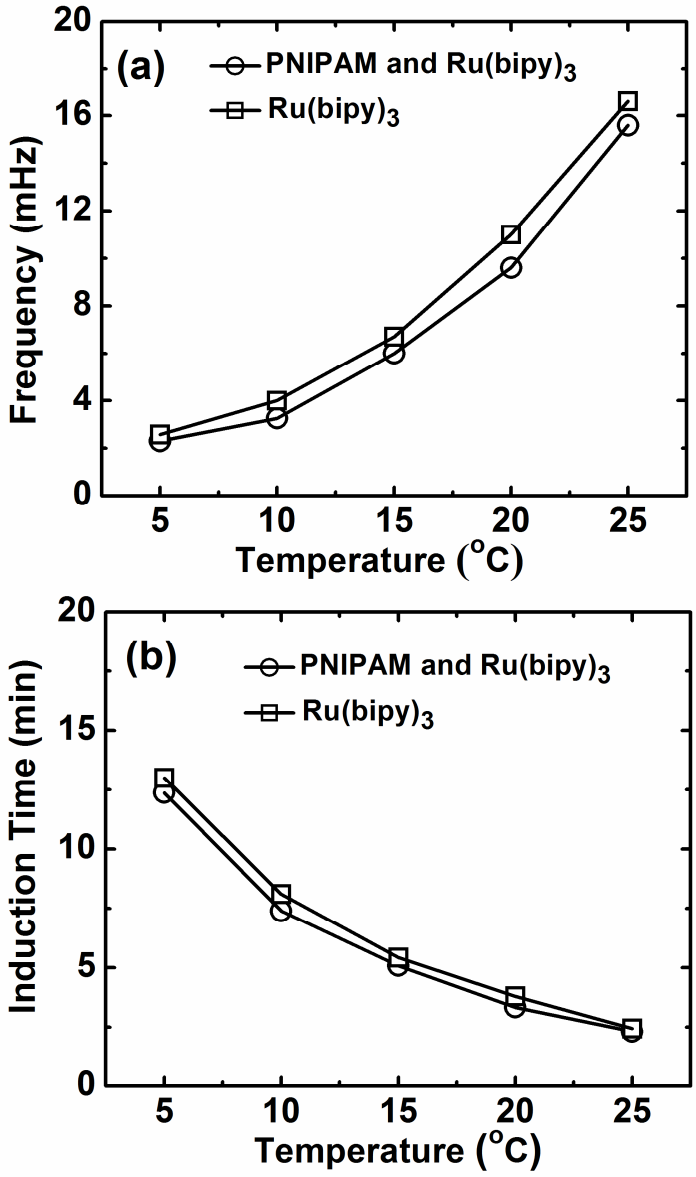

Figure 4.3 The dynamics of the temperature dependent BZ reaction. Comparison of BZ chemical oscillations using the catalyst $Ru(bipy)_3$ to that of oscillations with external addition of PNIPAM spheres in the BZ reactants. (a) Frequency, and (b) induction time.

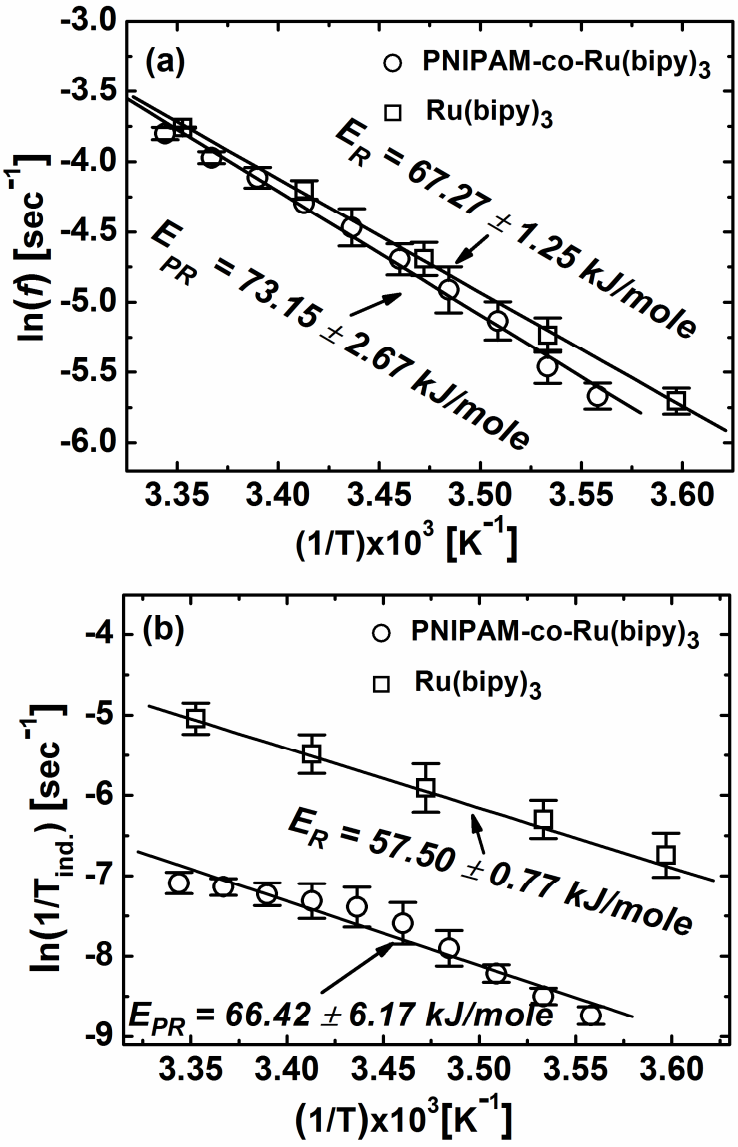

Figure 4.4 Arrhenius plots for the oscillatory and pre-oscillatory phases of the BZ reactions, yielding the apparent activation energies when the catalyst $Ru(bipy)_3$ is immobilized on PNIPAM spheres in comparison to that of conventional BZ chemical oscillations using the catalyst $Ru(bipy)_3^{+2}$. Calculated from (a) frequency, and (b) induction time. E_{PR} and E_R are the activation energies of PNIPAM-co-$Ru(bipy)_3$ and $Ru(bipy)_3^{+2}$ reaction systems, respectively.

to obtain the activation energies for immobilized and free catalyst BZ reactions. From the frequency and induction time measurements, the calculated activation energies for the immobilized catalyst are slightly higher than that of free catalyst. With the addition of polymer network, the reaction species experience a transport hindrance. Therefore, a higher amount of energy is required to cross the barrier, and hence higher activation energy for PNIPAM-co-Ru(bipy)$_3$ reaction system.

The collision factors A_i, and A_j, calculated from the Arrhenius plots (Figure 4.4) are listed in Table 4.1. The values of A_i in both immobilized and free catalysts systems for the oscillatory phase are found to be about one thousand times higher than those calculated from the induction phase (A_j), possibly due to the faster kinetics during the oscillation phase. Also, the collision factor for the immobilized catalyst system during the induction phase is found to be seven times smaller, compared with the free catalyst system. Even though a small A_j for the PNIPAM-co-Ru(bipy)$_3$ compared to free Ru(bipy)$_3^{+3}$ may suggest slow reaction kinetics between the catalyst and reactant molecules in the pre-oscillation phase, it is difficult to interpret the exact meaning of the pre-exponential factors in the case of complex reactions due to the multiple elementary

Table 4.1 Arrhenius collision factors for both oscillatory and induction phase of the BZ reaction.

Catalyst system	Oscillatory Phase, (A_i) (sec^{-1})	Induction Phase, (A_j) (sec^{-1})
Ru(bipy)$_3^{+3}$	$(1.63 \pm 0.78) \times 10^{10}$	$(7.32 \pm 2.2) \times 10^{7}$
PNIPAM-co- Ru(bipy)$_3$	$(1.44 \pm 0.68) \times 10^{10}$	$(1.08 \pm 0.33) \times 10^{7}$

steps and large calculation errors. These experimental findings revealed that the temperature has a strong influence on induction time when the catalyst is immobilized on PNIPAM gel particles, yet has a negligible effect on oscillations kinetics.

4.4.3 Temperature Dependent Comparison Analysis of BZ Oscillation Amplitude in Polymer-Immobilized and Free Ruthenium Catalyst BZ Reaction

In Figure 4.5, the amplitude of the BZ oscillations is compared at different temperatures between polymer immobilized and free ruthenium catalysts at 460 nm, specific to Ru(II) oxidation state. The amplitude of polymer size oscillation (measured at 570 nm) is overlaid into the plot. The oscillation amplitude specific to Ru(II) in the polymer-catalyst system is found to be smaller than that observed using the solution phase BZ catalyst. However, the amplitude gradually decreased with temperature for both catalytic systems, a general trend observed in normal BZ reaction. The amplitude decrease with temperature in the polymer-immobilized BZ reaction is found to be more pronounced at high temperatures compared to that of amplitude decrease in the free ruthenium catalyst case. The large decrease of amplitude at higher temperatures in the polymer case is due to the reduced transmission of light through the phase separated PNIPAM particles from aqueous BZ reaction. The size oscillation of the polymer, observed at 570 nm does not follow the amplitude trend observed at 460 nm. Instead, the amplitude increases with temperatures (Figure 4.6a). This behavior can be understood by plotting LCST curves for the catalyst immobilized polymer gel in both oxidized and reduced states of the ruthenium. Figure 4.6b shows the transmittance changes of PNIPAM-co-Ru(bipy)$_3$ gel beads as a function of temperature under the different conditions of the reduced Ru(II) state and oxidized Ru(III) state. The oxidized or reduced states of the ruthenium were maintained by dissolving PNIPAM-co-Ru(bipy)$_3$ in 0.3M HNO_3 containing either 0.005M Ce(IV)$(SO)_4$ or 0.005M Ce(III)$(SO)_4$, respectively.

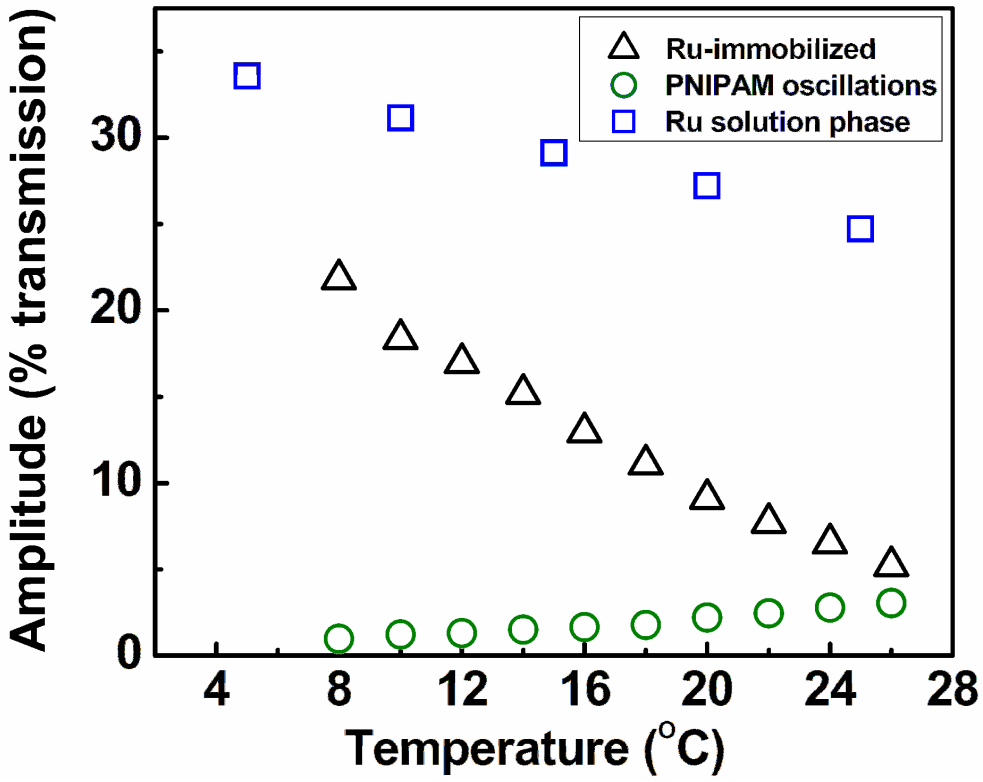

Figure 4.5 The amplitude dependence with temperature for the chemical and mechanical oscillations of the PNIPAM-co-Ru(bipy)$_3$ particles, in comparison with solution phase BZ reaction.

Due to the characteristics of thermo-sensitive NIPAM component, the transmittance decreases as the temperature increases, due to the increase in the turbidity. The transmittance in the oxidized state is larger than that in the reduced state all over the temperature range because the hydrophilicity of the polymer increases in the oxidized state. From the differences of the transmittance between the Ru(II) and the Ru(III) states, we may expect that the gel beads undergo periodical swelling-deswelling changes when the Ru(bipy)$_3$ moiety is oxidized and reduced periodically by the BZ reaction at constant

temperature. These periodic changes of gel beads can be detected as cyclic transparent and opaque changes for the suspension accompanying color changes due to the redox oscillation of the catalyst. It is observed that the difference in the transmittance increases with temperature between the oxidized and reduced states of the BZ reaction. Consequently, the amplitude increases with temperature.

4.5 Conclusions

The BZ reaction characteristics were compared between polymer immobilized and bulk catalyst systems at various temperatures. We found that the immobilization of the catalysts lengthens the induction time of the BZ reaction and this effect is more pronounced at lower temperatures. The high induction time for the immobilized catalyst case can be attributed to possible chemical (lowering of standard reduction potential of the ruthenium), and diffusional changes (due to the presence of a polymer network) of the BZ species due to the polymer addition. However, the rate determining step for the oscillation frequency is not affected by the polymer-catalyst interaction. Arrhenius pre-exponential factors and activation energies are calculated for both induction and oscillatory phase.

It is observed that the chemical bonding of PNIPAM spheres with BZ reaction catalyst can tailor the induction time while without effect on oscillation kinetics. The existence of a prolonged BZ reaction induction period with the immobilized catalyst in colloidal suspensions offers a temporal separation between the colloidal phase transition kinetics and the nonlinear dynamics of particle's size oscillation. For example, during the prolonged induction time of the BZ reaction, colloids can make the conventional phase transition (i.e. crystallization) from the metastable state into the crystalline state. Hence, the sample will be made up of a collection of small colloidal crystallites. The coarsening process will anneal the crystallites into larger crystals, with the smallest crystallites disappearing first. During the oscillatory state of the BZ reaction, the volume fraction of

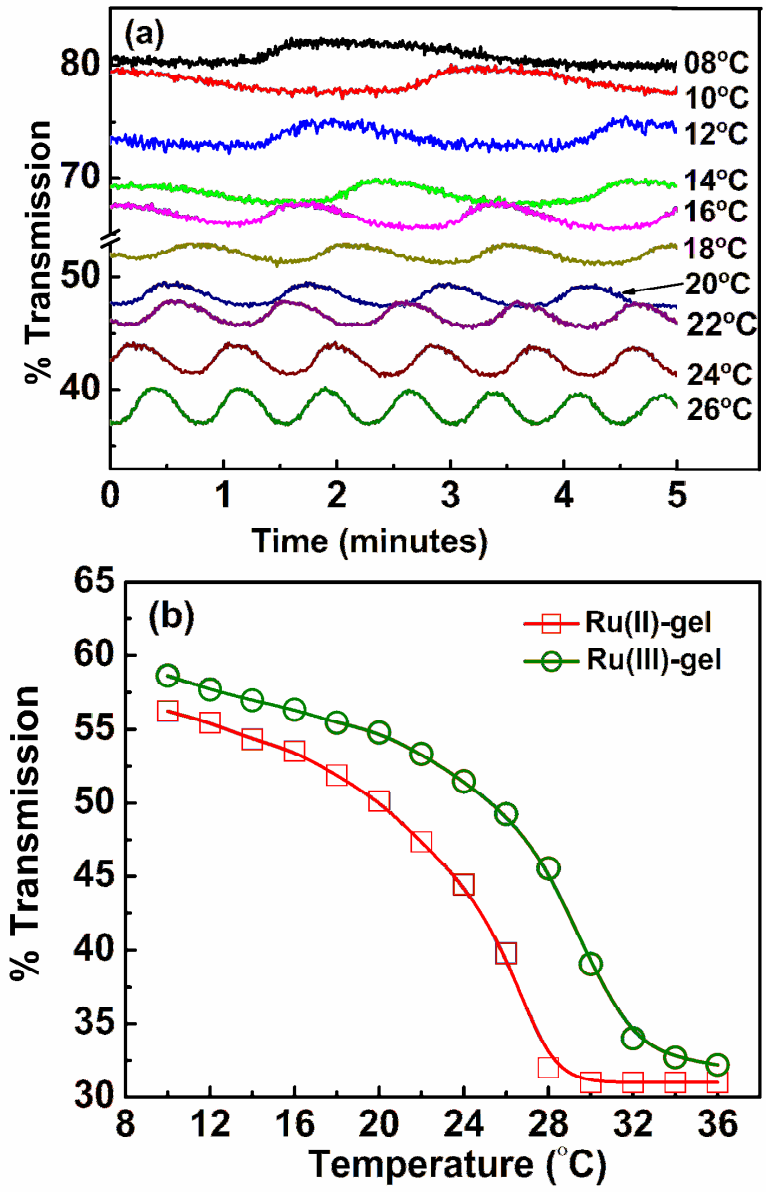

Figure 4.6 Temperature dependence of the transmittance for PNIPAM-co-Ru(bipy)$_3$ gel beads. (a) Size oscillations of PNIPAM-co-Ru(bipy)$_3$ particles, and (b) transmittance of PNIPAM-co-Ru(bipy)$_3$ in the (i) reduced Ru(II) state [in Ce(III) solution] and (ii) oxidized Ru(III) state [in Ce(IV) solution].

the particles decreases due to the reduced state of the metal catalyst. As a result, the volume fraction of the particles inside the crystallites also decreases, perhaps even to the degree that the crystallites become metastable (superheated), and melt. The smallest crystallite should melt first. Later, at the oxidized state of the BZ reaction, as the volume fraction increases again, the sample will recrystallize, and the larger crystallites have the advantage of growing faster. This melt-recrystallization process repeats during the BZ oscillatory phase. Therefore, BZ reaction should accelerate crystal annealing process. Currently, experiments are in progress in our lab to fabricate BZ active colloidal crystals.

CHAPTER V
TEMPERATURE DEPENDENCE OF THE OREGONATOR MODEL FOR THE BELOUSOV-ZHABOTINSKY REACTION*

5.1 Synopsis

It is well known that temperature plays an important role in the chemical dynamics of Belousov-Zhabotinsky (BZ) reactions. The five step Oregonator model of the BZ reaction has been elaborated here to investigate the temperature effect. The bifurcation dynamics has been calculated in the phase space spanned by initial reagents concentration ratio, stoichiometric factor and temperature. The combination of activation energies of the individual reaction steps governs the dependence of oscillation period and amplitude with temperature. The analysis reveals the existence of the temperature limits beyond which no oscillations occur.

5.2 Introduction

Every living system contains hundreds of chemical oscillators in which concentrations of the intermediate species vary periodically and the overall chemical reaction moves towards equilibrium. Chemical oscillators are often regarded as the model systems for biological rhythms such as heart beat, pulse etc. Temperature is one vital parameter that has a significant influence on the dynamics of oscillations. It is known that some bacteria such as pyrolobu fumarii, and strain 121 are capable of surviving up to 130°C,[128] due to the presence of stable enzymes that can function at high temperatures. It is always assumed that there might be an upper temperature limit for the biological systems. Yet,

---

*Reproduced by permission of the *Physical Chemistry Chemical Physics* Owner Societies, In press, **2009**, DOI: 10.1039/b820464k. Copyright 2009 Royal Society of Chemistry.

the precise upper temperature limit for life has not been found. The upper temperature limit where the molecular repair and resynthesis becomes unsustainable is predicted to be the region of 140-150°C.[129] Knowledge about the upper temperature limit of the biological oscillators is essential to answer some of the fundamental questions about the biological evolution on the hot early earth, the depth in the sea to which life might exist and a potential life in hot, extraterrestrial environments. In this work, it is our fundamental interest to investigate the dynamics of nonlinear oscillatory processes at high temperatures. We used a simple non-living chemical reaction, the Belousov-Zhabotinksy (BZ) reaction as a model system to study how temperature controls the reaction dynamics.

The complex nature of the BZ reaction, and its similarities to the biological oscillators, has attracted extensive attention from both experimentalists and theoreticians.[93,98,118,130-134] A well supported mechanism of the reaction, given by Field, Koros, and Noyes (FKN), supplied an intellectual framework for the experimental and theoretical investigation of the BZ reaction dynamics.[47,67,135,136] The simpler version of the reaction model, namely the Oregonator model, can reproduce the essential characteristics of the reaction. It used three composition variables, five irreversible reaction steps controlled by five rate constants and a stoichiometric factor, f (which is proportional to the ratio between the average number of bromide ions produced and the number of Ce^{4+} ions consumed during the malonic acid oxidation step). The modified Oregonator model can display complex dynamics such as excitability,[133,137] bistability,[138] target or spiral wave patterns,[139,140] chaos,[141] amplitude death or even mixed mode oscillations.[134,142]

The bromide driven chemical oscillators highly depend on temperature. The history of research on the temperature dependent BZ oscillations dates back to 1974 when Koros first time reported the dependence of oscillatory frequency on temperature.[117] Since then many efforts have been made to understand the oscillatory dynamics with temperature.[122,123,127,143-147] The reaction was studied at different temperatures, ranging

from 15°C to 88°C.[127,146] In general, frequency increases with temperature and the BZ rate constants follow the Arrhenius law. For the classical cerium catalyzed BZ reaction, the overall activation energy of about 70 kJ/mole was determined.[117,148] However, limited studies are available about the temperature influence of the BZ reaction due to the unknown rate constants and the complexity of the reaction.

The stability of the steady states in the Oregonator model has been analyzed using either the rate constant k_5 of the bromide regeneration step or f as the bifurcation parameter.[67,134,149] A change in the value of the parameter makes the system passes from a stable to an unstable state, or vice versa. Although, the Oregonator model and its modified versions revealed many interesting features of the BZ reaction, the oscillation dynamics over a wide range of temperatures has not been fully explored. Here, we have investigated the stability of the steady states in a *three* dimensional phase space spanned by the temperature T, f, and the initial reagent concentration ratios (b, malonic acid divided by a, sodium bromate). We have included temperature in rate constants by using the Arrhenius equation and analyzed the stability of the system while changing f and T.

The activation energies of the individual reaction steps of the Oregonator model mainly govern the temperature dependent oscillation dynamics. For the case of the ferroin catalyzed BZ reaction, experimental values of the activation energies of the BZ reaction are reported recently.[150] However, due to the complexity of the reaction, the activation energies of the individual reaction steps are usually associated with large errors. We selected two sets of activation energies and calculated the associated bifurcations along the T, f, and b/a plane. Activation energies of set (ii) in Table 5.1 are used to reduce the maximum upper temperature limit, calculated using activation energies of set (i) in Table 5.1 to a value closer to the observation in the experiments. A temperature dependent bifurcation in both cases estimates the upper temperature limits for different b/a and f, which may provide insights into the understanding of the theoretical upper temperature limits exhibited by the systems that display nonlinear chemical dynamics.

5.3 Theory

5.3.1 Oregonator Model with Temperature Dependent Rate Constants

The classical three dimensional Oregonator consists of the following kinetic equations:[136,137]

$$\frac{dX}{dt} = k_1 H^2 AY - k_2 HXY + k_3 HAX - 2k_4 X^2 \quad (35a)$$

$$\frac{dY}{dt} = -k_1 H^2 AY - k_2 HXY + k_5 hBZ \quad (35b)$$

$$\frac{dZ}{dt} = 2k_3 HAX - k_5 BZ \quad (34c)$$

where,

$X = [HBrO_2]$, $Y = [Br^-]$, $Z = [Ce(IV)]$, $A = [BrO_3^-]$,
$B = [CH_2(COOH)_2]$, $H = [H^+]$,

and

$h = 2f$.

The kinetic rate constants in Eq. (35) are labeled according to their original sequence. The Arrhenius equation for the rate constant is given by,

$$k_i = k_i^* \exp\{(-E_i / R)[(1/T) - (1/T_0)]\}, \quad (36)$$

where i=1…5. T_0 is room temperature. k_i^* is rate constant of the ith reaction step at T_0, which is taken using the "Lo" values proposed by Tyson.[68] E_i is the activation energy of i^{th} reaction step in the Oregonator. And R is the gas constant, R = 8.314 J K^{-1}mol^{-1}. For simplicity, the frequency factor in the Arrhenius equation is assumed to be constant over a wide range of temperature.

The following widely accepted scaled dimensionless parameters and variables are adopted here:[151,152]

$$x = \frac{X}{X_0},\ y = \frac{Y}{Y_0},\ z = \frac{Z}{Z_0},\ \tau = \frac{t}{t_0},$$
$$a = \frac{A}{A_0},\ \text{and}\ b = \frac{B}{B_0}. \tag{37}$$

With the subscript 0 denotes the reference values,

$$X_0 = \frac{k_3 H A_0}{2k_4},\ Y_0 = \frac{k_3 A_0}{k_2},$$
$$Z_0 = \frac{(k_3 H A_0)^2}{k_4 k_5 B_0},\ t_0 = \frac{1}{k_5 B_0}. \tag{38}$$

Table 5.1 lists the values of the kinetic parameters[151] and two sets of activation energies for the individual reaction steps. Also, $[H]^+$ = 1M and $A_0 = B_0 = 1$M.

Plugging Eqs. (36)-(38) into (35), the kinetic equations become,

$$\varepsilon(T)\frac{dx}{d\tau} = q(T)ay - xy + ax - x^2 \tag{39a}$$

$$\delta(T)\frac{dy}{d\tau} = -q(T)ay - xy + fbz \tag{39b}$$

$$\frac{dz}{d\tau} = ax - bz \tag{39c}$$

where

$$\varepsilon(T) = \left(\frac{k_5 B_0}{k_3 H A_0}\right) = \varepsilon_0\, e^{\frac{E_3 - E_5}{R}\left(\frac{1}{T} - \frac{1}{T_0}\right)},\ q(T) = \left(\frac{2k_1 k_4}{k_2 k_3}\right) = q_0\, e^{\frac{E_2 + E_3 - E_1 - E_4}{R}\left(\frac{1}{T} - \frac{1}{T_0}\right)},$$

Table 5.1 Selected kinetic rate constants at room temperature and two sets of activation energies of the Oregonator elementary steps.

Kinetic rate constants at 298K	k_1^*	k_2^*	k_3^*	k_4^*	k_5^*
	$2\ M^{-3}S^{-1}$	$10^6\ M^{-2}S^{-1}$	$10\ M^{-2}S^{-1}$	$2000\ M^{-1}S^{-1}$	$1\ M^{-1}S^{-1}$
Activation energies	E_1 (kJ/mole)	E_2 (kJ/mole)	E_3 (kJ/mole)	E_4 (kJ/mole)	E_5 (kJ/mole)
Set (i)	54	25	60	64	70
Set (ii)	60	25	60	75	70

$$\delta(T) = \left(\frac{2k_4 k_5 B_0}{k_2 k_3 H^2 A_0} \right) = \delta_0 \, e^{\frac{E_2 + E_3 - E_4 - E_5}{R}\left(\frac{1}{T} - \frac{1}{T_0}\right)},$$

$$\varepsilon_0 = \left(\frac{k_5^* B_0}{k_3^* H A_0} \right) = 0.10,\ q_0 = \left(\frac{2k_1^* k_4^*}{k_2^* k_3^*} \right) = 8 \times 10^{-4},\ \text{and}\ \delta_0 = \left(\frac{2k_4^* k_5^* B_0}{k_2^* k_3^* H^2 A_0} \right) = 4 \times 10^{-4}.$$

Eq. (39) retains the same format as in the original model[135] except that the variables, $\varepsilon(T), \delta(T), \text{and}\, q(T)$ are now temperature dependent. Their values at different temperatures are listed in Table 5.2.

Using the pseudo-steady state approximation for *y*, i.e., $\delta(T) << \varepsilon(T)$, Eq. (39) is converted into a pair of ordinary differential equations:

$$\varepsilon(T)\frac{dx}{d\tau} = -fbz\left(\frac{x - aq(T)}{x + aq(T)}\right) + ax - x^2, \tag{40a}$$

$$\frac{dz}{d\tau} = ax - bz. \tag{40b}$$

The positive steady state of this equation is given by,

$$x_s = a\alpha(T),\ y_s = a\beta(T), \text{ and } z_s = \frac{a^2\alpha(T)}{b}$$

where,

$$\alpha(T) = \frac{1}{2}\left[(1 - f - q(T) + \left\{(1 - f - q(T)\right\rangle^2 + 4q(T)(1 + f)\right\}^{1/2}\right], \tag{41a}$$

and,

$$\beta(T) = \frac{f\alpha(T)}{\alpha(T) + aq(T)}. \tag{41b}$$

5.3.2 Numerical Methods

Equation (40) is made up of stiff differential equations. We carried out the numerical calculations using routine ode23s in Matlab V6.R12, which is a one-step solver based on a modified Rosenbrock formula of order 2, capable of solving moderate stiff problems. The relative and absolute error tolerance of ode23s solver was set to 10^{-6} and 10^{-10}, respectively, for high accuracy. To test the validity of the calculation, we have also calculated the time series with the ode15s routine, which is a multistep variable-order solver with higher accuracy than ode23s, but less efficient. The results were found to be the same when compared to the time series calculations with the ode23s routine. Therefore, to calculate the time series over a long time spans, the ode23 routine was used for adequate accuracy and efficiency.

Table 5.2 Parameter values for dimensionless quantities at various temperatures, calculated using the activation energies of set (i) in Table 5.1. The initial reagent concentration ratio b/a is set to 1.

Temperature(K)	$\varepsilon(T)$	$q(T)$	$\delta(T)$
300	0.10251	8.68×10^{-04}	4.172×10^{-04}
325	0.13955	2.40×10^{-03}	7.048×10^{-04}
350	0.18178	5.75×10^{-03}	1.104×10^{-03}
375	0.22858	1.22×10^{-02}	1.630×10^{-03}
400	0.27932	2.37×10^{-02}	2.293×10^{-03}
425	0.33337	4.25×10^{-02}	3.97×10^{-03}
450	0.39013	7.15×10^{-02}	4.46×10^{-03}

5.4 Results and Discussion

5.4.1 Nullcline Analysis and Trajectories in the x-z Plane

Unless otherwise stated, activation energies of set (i) (in Table 5.1) are used in the results and discussion section. The phase plane analysis involving two variables x and z, is carried out to gain insights into how the oscillations rise and disappear with temperature. The x and z nullclines are

$$-fbz\left(\frac{x-aq(T)}{x+aq(T)}\right)+ax-x^2=0 \tag{42a}$$

$$ax-bz=0 \tag{42b}$$

Figure 5.1 plots x, z nullclines of Eq. (42) for different *f*, and T with b/a ratio equal to 1.0. The z-nullcline (Eq. 41b) is a straight line with slope a/b, is independent of temperature, whereas the shape of x-nullcline (Eq. 41a) changes with temperature. The position of the steady state (intersection of the nullclines) depends on *f* and T. As temperature increases, the steady state S moves from an unstable state (on the middle branch of the x-nullcline) to a stable state. (on the right or left branch). In some cases, the middle branch of the x-nullcline disappears at high temperatures (e. g. at 470K in the Figure 5.1b) and the function of x decreases monotonically.

From Eq. 8a,

$$z = \frac{(ax - x^2)\,(x + aq(T)}{fb[x - aq(T)]} \tag{43}$$

The sufficient condition for Eq. (43) to decrease monotonically in the range x > $q(T)$ is that the derivative of this function, dz/dx has no positive roots. Through $q(T)$, dz/dx depends on temperature. The product $(dz/dx)\, fb[x - aq(T)]^2$ is a third order function of x. With increasing $q(T)$, at approximately $q(T)$ = 0.08 (when a = 1), the two positive roots disappear. Hence, at high temperature, only steady states exist as the x-nullcline becomes a monotonically decreasing function of x. Therefore, a bifurcation from oscillation to steady state exists at a high temperature, which is the upper limit for the existence of the oscillations. However, in other cases, the middle branch of the x-nullcline will not disappear at high temperatures when the steady state exists, as shown in Figure 5.1a for f = 0.6.

Trajectories in the x-z plane are shown in the Figure 5.2(a-d) for selected temperatures. Figure 5.2a plots the case for f = 0.6, and b/a=1. Since $\varepsilon(T)$ is very small, the trajectories move faster along the x direction compared with those in the z direction. When the

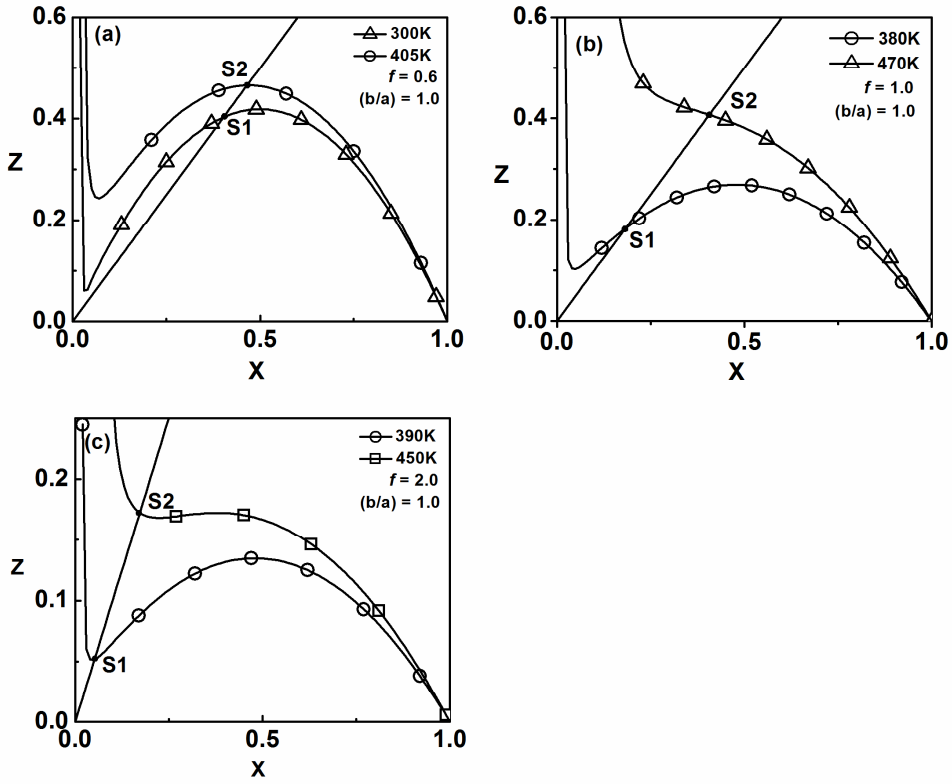

Figure 5.1 The temperature dependence of the nullclines in the Oregonator model at various stoichiometric factors. The initial reagent concentration ratio, b/a = 1. The activation energies are chosen from set (i) in Table 5.1. For each *f*, as the temperature rises, the reaction moves from an unstable state (S1) to a stable steady state (S2). Hence, there is an upper temperature limit for the oscillatory state.

temperature is raised from 298 to 340K, the size of limit cycles (amplitude of oscillations) decrease gradually, which in turn results in the more number of cycles per second (the frequency of oscillations). The further temperature increase to 360K will make the system reach a stable steady state. These analyses confirm the existence of an upper temperature limit above which the system rests in its non-oscillatory stable state.

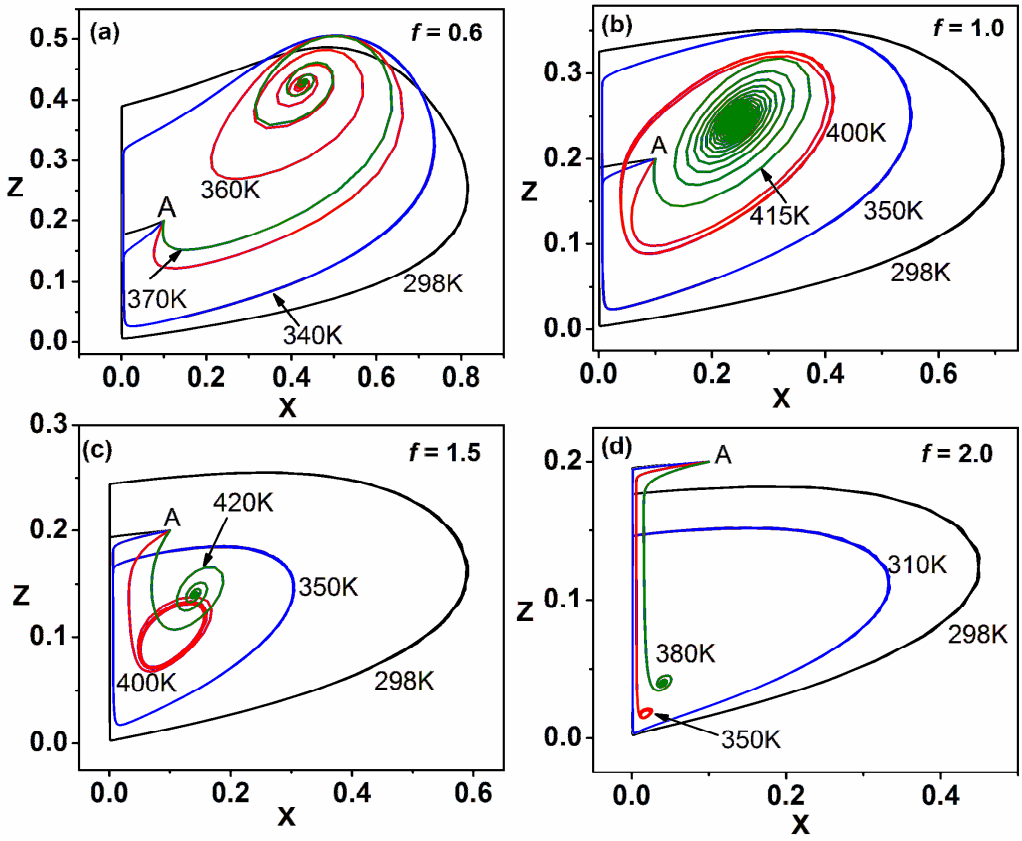

Figure 5.2 Trajectories in the x-z plane for the two variable Oregonator model at different temperatures and stoichiometric factors. Initial concentrations are taken as b/a = 1. The activation energies of set (i) in Table 5.1 are chosen. Point A is the initial point which is set to x = 0.1 and z = 0.2.

Figure 5.2(b-d) plots trajectories for f = 1.0, 1.5, and 2.0, respectively. The corresponding upper temperature limits are 415, 420 and 370K. Clearly, the upper temperature limits also strongly depend on the stoichiometric factors. Moreover, an increase in f at a constant temperature results in a decrease in the amplitude of the oscillations for both x and z. The trajectories of limit cycle oscillations profiles of x and z with time are shown in Figure 5.3. The amplitude of oscillations decreases with an increase in temperature and decays to zero after 80 seconds at 415K. Also the oscillation

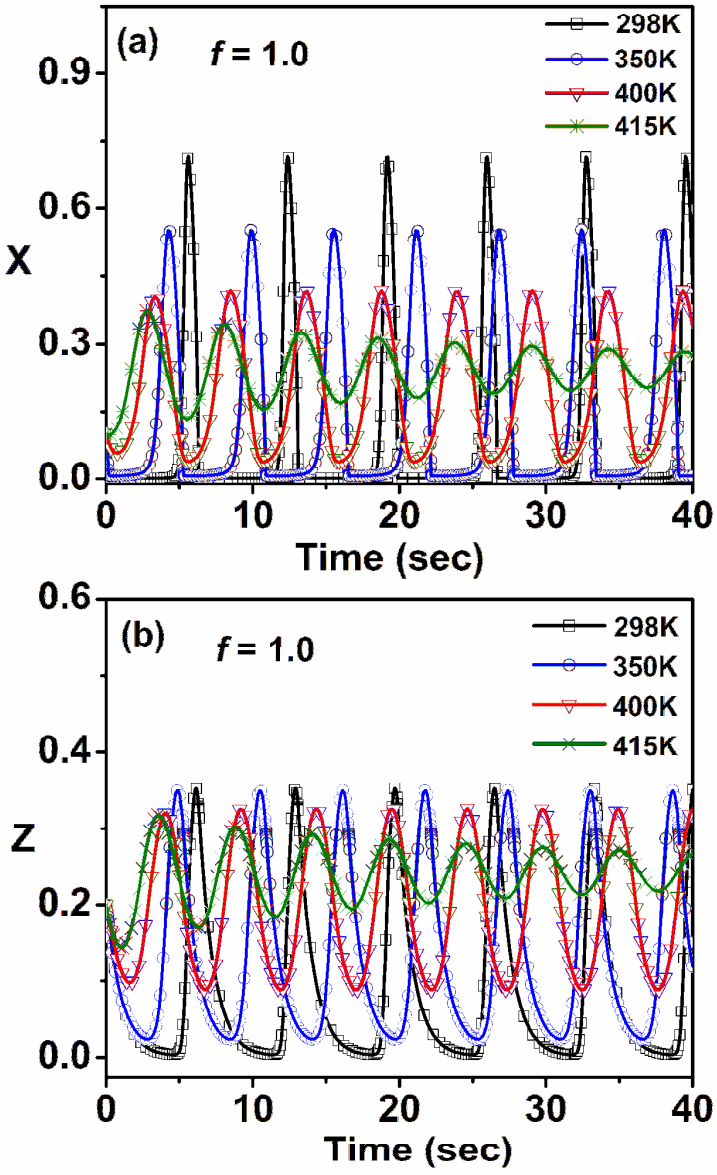

Figure 5.3 Temperature dependent oscillations for the reduced Oregonator model using the activation energies of set (i) in Table 5.1. The stoichiometric factor f = 1.0, and b/a = 1.

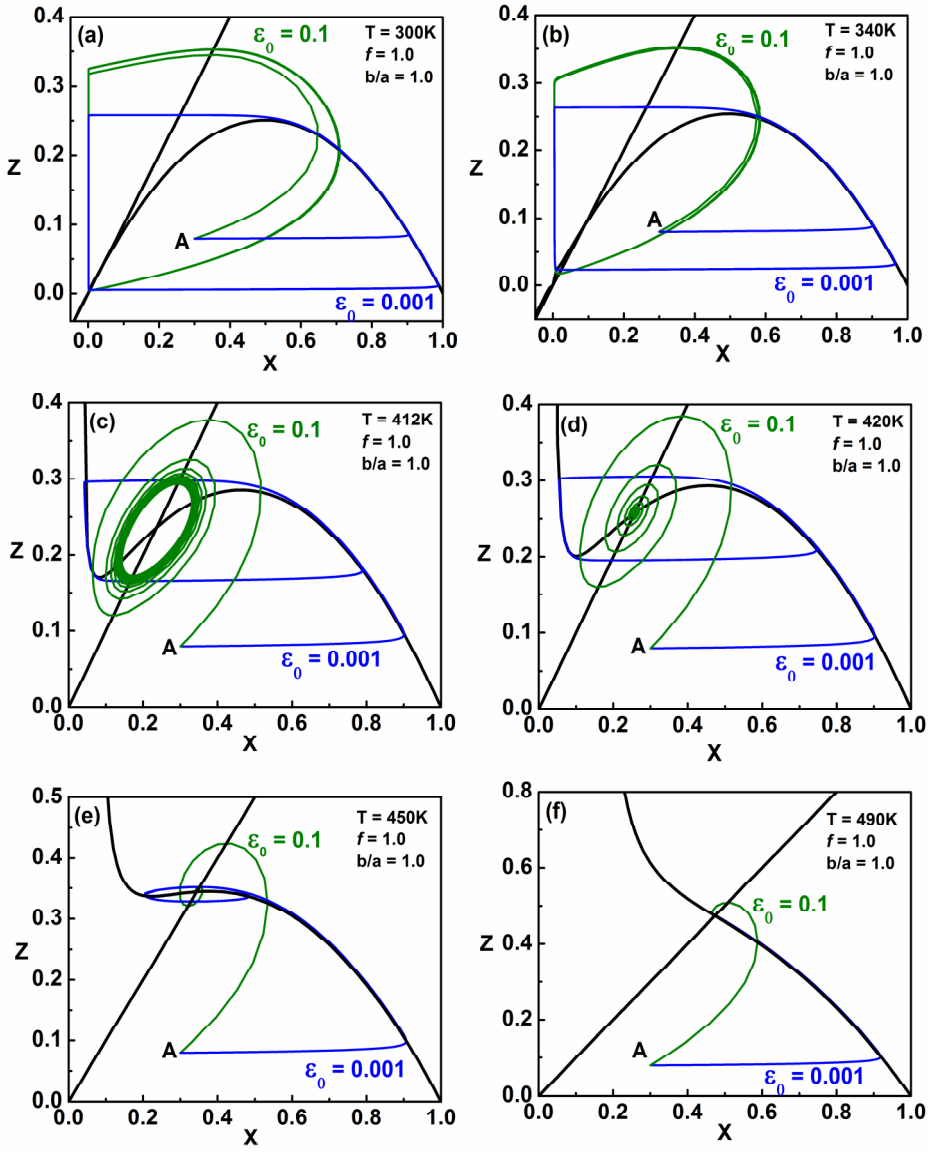

Figure 5.4 Overlaid graphs of nullclines and trajectories of limit cycle oscillations with $\varepsilon(T)$ changing from 0.1 to 0.001 at different temperatures, (a) 300K, (b) 340K, (c) 412K, (d) 420K, (e) 450K, and (f) 490K, using the activation energies of set (i) in Table 5.1. The stoichiometric factor f = 1.0, and b/a = 1. The initial conditions at point A are x_0 = 0.3 and z_0 = 0.08.

frequency increases with temperature and finally reduces to zero at the high temperature limit, which is a characteristic of supercritical Hopf bifurcation.

The nullclines and the corresponding limit cycle oscillations are overlaid in a single plot in Figure 5.4(a-f) with $\varepsilon(T)$ changing from 0.1 to 0.001 at different temperatures. For each temperature, the b/a, and f are fixed at 1.0. The initial conditions at point A are, x_0 = 0.3 and z_0 = 0.08. The BZ model system reaches steady state at about 415K when $\varepsilon(T)$ = 0.1, and 465K when $\varepsilon(T)$ is 0.001. It is evident from the plots that the nullcline analysis is incomplete and inconclusive. As the nullclines are insensitive to the changes in $\varepsilon(T)$, they cannot measure the accurate steady state temperatures. For example, in Figure 5.4d, the trajectories move towards the stable steady state when $\varepsilon(T)$ = 0.1, whereas the nullclines show that the steady state is unstable. The nullcline analysis only gives intuition about the stability of the steady state. When $\varepsilon(T)$ = 0.1, limit cycle oscillations surrounds the equilibrium point at temperatures below a maximum temperature limit. However, the path of trajectories is not parallel to either x or z axis. As $\varepsilon(T)$ is reduced to 0.001, the trajectories jumps faster along x direction, but the steady state is achieved at a higher temperature compared with those when $\varepsilon(T)$ = 0.1. In the later case, the time scale due to the product $\varepsilon(T)\,dx/d\tau$ is thousand times smaller in the x direction compared to those time scales in the z direction, resulting in the increases stiffness of the differential equations (40).

5.4.2 Stability Analysis for the Reduced Oregonator Model

To determine the stability of the steady state of the Oregonator at different temperatures and to find out the conditions when the steady state loses its stability to exhibit limit cycle oscillations, asymptotic stability techniques are applied.[153,154] In order for a chemical system to exhibit limit cycle oscillations, it is necessary that the steady state is unstable to an infinitesimal perturbation. Linearizing equation (40) around its steady

state (x_s, z_s) yields a Jacobian matrix *J*. The trace of *J* at (x_s, z_s), is given by the following expression,

$$\mathrm{Tr}(J) = \frac{a}{\varepsilon(T)}\left(1 - 2\alpha(T) - \frac{2q(T)f\alpha(T)}{\left(\alpha(T)+q(T)\right)^2}\right) - b, \tag{44}$$

and,

$$\det(J) = \frac{ab\left[\alpha(T)^2 + q(T)\alpha(T) + 2q(T)\beta(T)\right]}{\varepsilon(T)\left[\alpha(T)+q(T)\right]}, \tag{45}$$

which is positive. The criteria for a Hopf bifurcation (for a positive determinant *J*) is set by Tr(*J*) = 0. The analysis presented by Gray and Scott[153] is followed for classifying the behavior of two dimensional systems based on the nature of the solutions to Tr(*J*) = 0.

Therefore, the condition for the Hopf bifurcation is given by,

$$\frac{b}{a} = \frac{1}{\varepsilon(T)}\left(1 - 2\alpha(T) - \frac{2q(T)f\alpha(T)}{\left(\alpha(T)+q(T)\right)^2}\right). \tag{46}$$

The Hopf bifurcation boundaries are presented in Figure 5.5. In Figure 5.5a, a boundary surface divides two regions, below which the Tr(*J*) is positive and the steady state is unstable. Above the surface, the Tr(*J*) is negative and the steady state is stable. Also, for each *f* and b/a, we can compute the temperature limits below which an unstable steady state prevails. Figure 5.5b represents a projection of the bifurcation surface in the *f*-T plane. The oscillatory region is shown below the bell shaped line, where the Tr(*J*) is positive. A shift from the blue to red colored regions indicates a higher b/a value. A low malonic acid, b or/and a high bromate concentration, a favors oscillations over a wide range of *f*. On the other hand, a high b/a value reduce the oscillation region in the *f*-T plane. The bifurcation curves with two parameters *f* and b/a for different temperatures

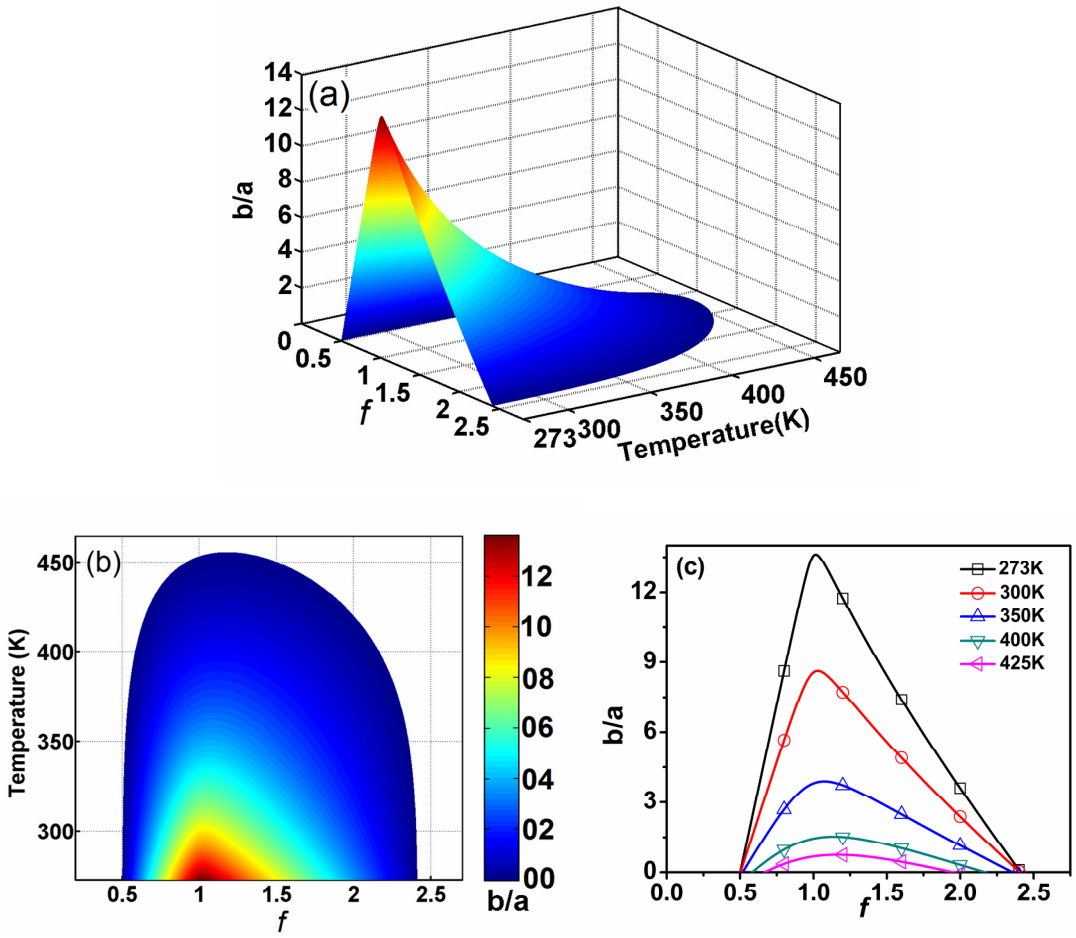

Figure 5.5 Bifurcation diagram for the temperature dependent two variable Oregonator model. The activation energies of set (i) in Table 5.1 are used. (a) The upper temperature limit surface in the phase space of temperature, initial reagent concentration ratio and stoichiometric factor. The model exhibits limit cycle oscillations below the colored bifurcation surface. (b) Plot of oscillatory region in the plane of temperature and stoichiometric factor. The color bar indicates different values of initial concentration ratios b/a. Each b/a cuts a curve in the *f*-T plane which encloses the oscillation region below it. The maximum upper temperature limit is about 455K when b/a is close to zero. (c) Bifurcation curve in the plane of stoichiometric factor and initial reagent concentration ratios at various temperatures. Below the curves are the regions of oscillations.

are plotted in Figure 5.5c. For every point below the curve, the Tr(J) is positive and the steady state is unstable. With a rise in temperature, the area of the oscillatory region shrinks and no oscillations are observed when the temperature reaches 455K. This is the maximum upper temperature limit when the concentration ratio b/a is close to zero.

The maximum upper temperature limit (455K) for the existence of oscillations is well above the physical limit (100°C at 1 atm) of aqueous BZ reaction system. In spite of the numerous efforts to unfold the oscillation dynamics of the BZ reaction, little information is available in the literature on the high temperature oscillatory dynamics. The experimental findings so far are inconclusive. Misra[146] has showed that the cerium catalyzed BZ reaction in a flow reactor displays an upper temperature limit of about 361K when b/a is equal to 1.83. Here, we notice that the activation energies of the elementary reaction steps of the Oregonator model significantly influence the upper temperature limits for the existence of oscillations. As a result, we select another set [set (ii) in Table 5.1] of activation energies to correlate the model prediction to those observed in the experiments.

The three dimensional bifurcation diagram in the Figure 5.6a uses activation energies of set (ii) in Table 5.1. Compared to Figure 5.5a, the bifurcation surface in (b/a)-T plane is flatter. The calculated upper temperature limit is adjusted to 361K when b/a is equal to 1.83 (Figure 5.6b). Since both $q(T)$ and $\varepsilon(T)$ contain temperature dependent parameters, the sign of the combinations of activation energies control the temperature dependence of amplitude and period of oscillations. When $E_2+E_3-E_1-E_4$, and E_3-E_5 are negative, an upper temperature limit exists. The upper temperature limit reduces to a lower value when $E_2+E_3-E_1-E_4$ and E_3-E_5 become more negative. Under these conditions, the BZ reaction exhibits Arrhenius oscillatory behavior. The period and amplitude of the oscillations decreases with temperature, as shown in Figure 5.7. The temperature compensation (an interesting phenomena of unchanged oscillatory period and amplitude over a wide range of temperature), occurs when $E_2+E_3-E_1-E_4$ and E_3-E_5 equals to zero.

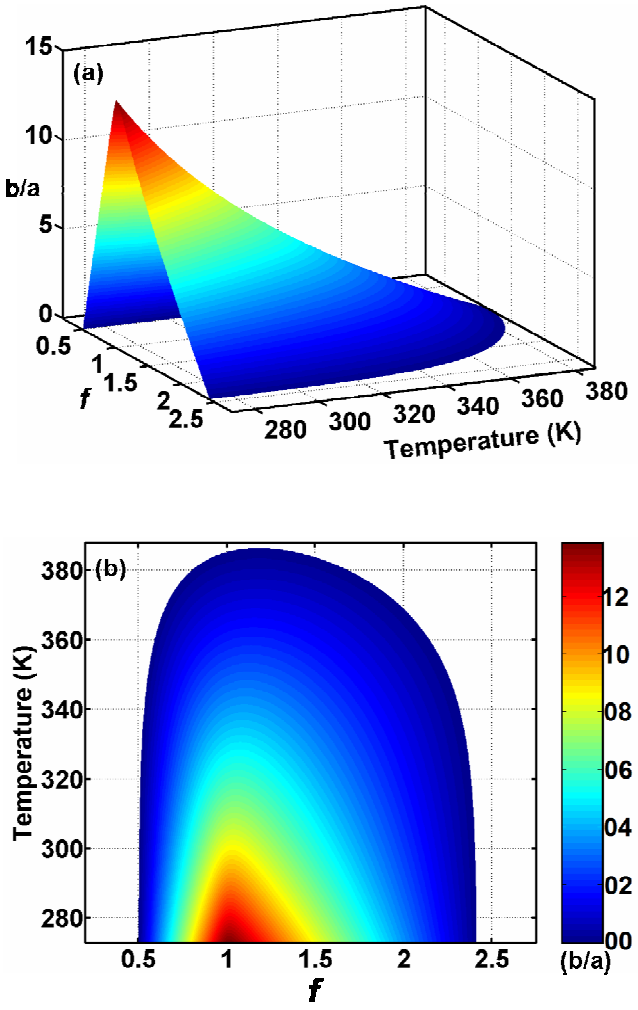

Figure 5.6 Bifurcation diagram for the temperature dependent two variable Oregonator model. The activation energies of set (ii) in Table 5.1 are used. (a) The upper temperature limit surface in the phase space of temperature, initial reagent concentration ratio and stoichiometric factor. The model exhibits limit cycle oscillations below the colored bifurcation surface. (b) Plot of oscillatory region in the plane of temperature and stoichiometric factor. The color bar indicates different values of initial concentration ratios b/a. Each b/a cuts a curve in the *f*-T plane which encloses the oscillation region below it. The maximum upper temperature limit is about 387K when b/a is close to 0, and 361K when b/a is equal to 1.83.

Therefore, the positive feed back loops are counterbalanced by negative feedback loops for a given set of activation energies.

Recent experiments show a non-Arrhenius oscillation behavior during the catalytic oxidation of formic acid[155] on a polycrystalline platinum electrode unlike the oxidation in methanol.[156] At high applied currents, temperature compensation is observed and at low applied currents, both period and amplitude increases with temperature (temperature over-compensation). The authors point out that the non-Arrhenius behavior arises from the interplay among reaction steps than the actual temperature dependence of the individual steps. In our model, when $E_2+E_3-E_1-E_4$ and E_3-E_5 are positive, temperature over-compensation is observed. The amplitude and period of oscillations increases with temperature, and the reaction follow non-Arrhenius oscillation behavior where a lower temperature limit exists. It is noteworthy that the Oregonator model here can display all three important phenomena, the temperature compensation, Arrhenius, and non-Arrhenius oscillatory behavior. Due to the multiple reaction steps of the BZ reaction and uncertainty of temperature dependent parameters, the results presented here illustrates the qualitative characteristics of the BZ reaction.

5.4.3 Characteristics of Hopf Bifurcation with Temperature

In Hopf bifurcations when the bifurcation parameter p increases to a value p_c the steady state looses its stability and a limit cycle forms surrounding the steady state. In a supercritical Hopf bifurcation, the limit cycle is stable and the steady state loses its stability and any small perturbation will cause the system to produce sustained oscillations. The amplitude grows gradually with increasing p. In a subcritical Hopf bifurcation, the steady state maintains its stable steady state, but becomes surrounded by a pair of limit cycles, an unstable inner one which exists when p is less than p_c and a stable outer one. The character of Hopf bifurcation is determined by applying normal form analysis. For the two variable Oregonator, normal form analysis yield the following expression for the coefficient $a_1(T)$ as,[149]

$$a_1(T) = \frac{1}{16\omega(0)}\left[\omega(0) f_{111} - b_H f_{112} + f_{11}\left\{f_{12}(1-\phi_0{}^2) + \phi_0 f_{11}\right\}\right] \tag{47}$$

where,

$$b_H = \frac{a}{\varepsilon(T)}\left(1 - 2\alpha(T) - \frac{2q(T) f\alpha(T)}{\left(\alpha(T) + q(T)\right)^2}\right),$$

$$\omega(0) = a\sqrt{-(b_H / a)(b_H / a + c)},$$

$$c = \frac{-f\left[\alpha(T) - q(T)\right]}{\varepsilon\left[\alpha(T) + q(T)\right]},$$

$$\phi_0 = \frac{\gamma(0)}{\eta(0)}, \qquad \gamma(0) = -1/c,\ \eta(0) = -\omega_0 / c b_H,$$

$$f_{11} = \frac{2}{\varepsilon(T)}\left(\frac{2fq(T)\alpha(T)}{\left[q(T) + \alpha(T)\right]^3} - 1\right) + \frac{4q(T) b_H}{a\left[q(T)^2 - \alpha(T)^2\right]},$$

$$f_{12} = \frac{q(T)\omega(0)}{a\left[q(T)^2 - \alpha(T)^2\right]},$$

$$f_{111} = \frac{-12q(T)}{a^2\left[q(T) + \alpha(T)\right]^4}\left(\frac{fa\alpha(T)}{\varepsilon(T)} + \frac{b_H\left[q(T) + \alpha(T)\right]^2}{q(T) - \alpha(T)}\right),$$

$$f_{112} = \frac{-4q(T)\omega(0)}{a^2\left[q(T) - \alpha(T)\right]\left[q(T) + \alpha(T)\right]^2}.$$

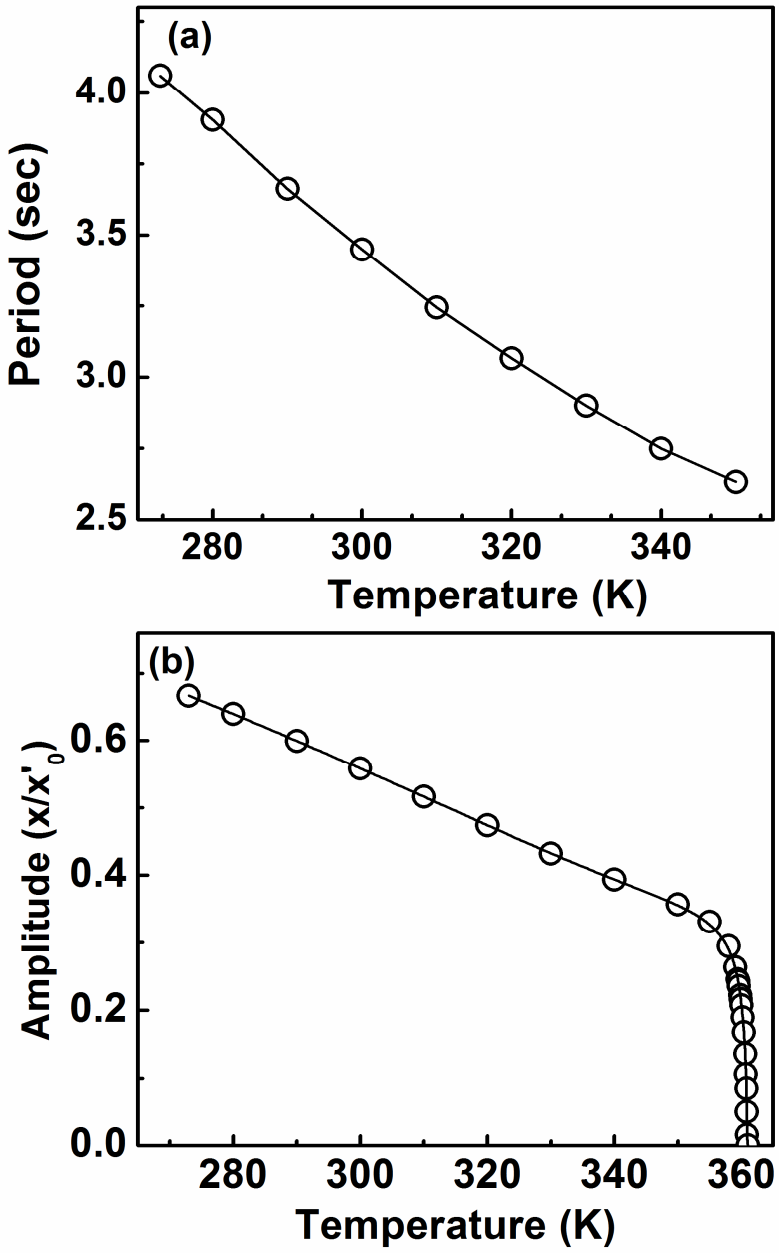

Figure 5.7 Temperature dependence of oscillation period and amplitude for the reduced Oregonator model. The activation energies are used from set (ii) in Table 5.1. The stoichiometric factor $f = 1.0$, and b/a = 1.83.

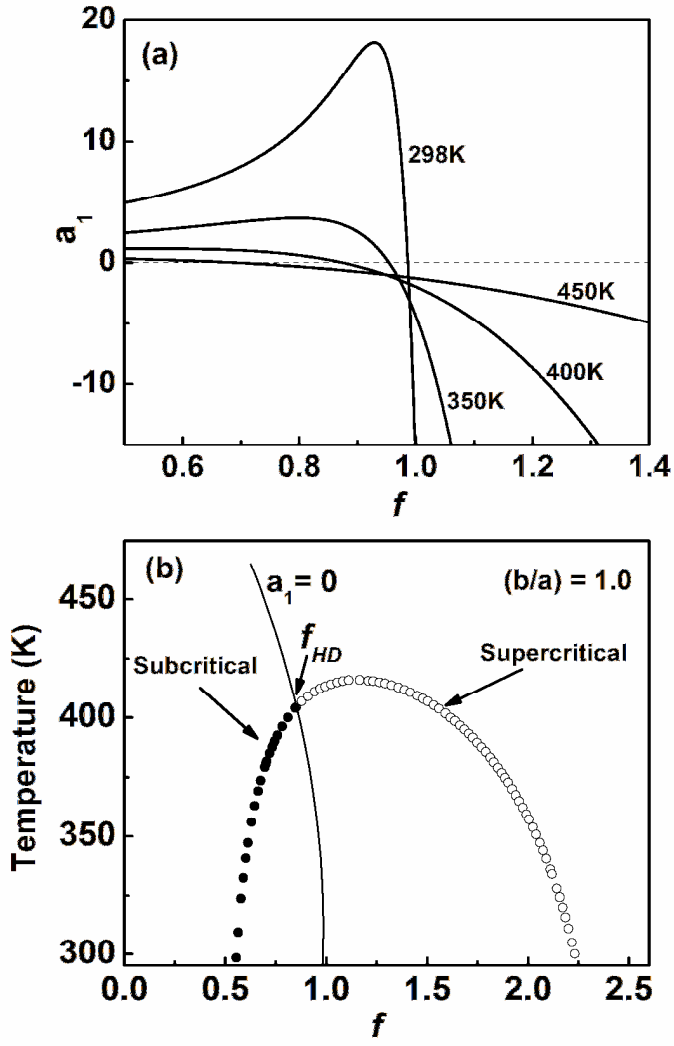

Figure 5.8 Application of normal form analysis to determine the character of Hopf bifurcation at different temperatures. (a) The reaction undergoes a supercritical Hopf bifurcation when $a_1 < 0$, and a subcritical Hopf bifurcation when $a_1 > 0$. (b) Representation of the subcritical and supercritical Hopf bifurcations in the *f*-T plane. The bifurcation curve (circular symbols) cuts out with b/a = 1 from the bifurcation surface (Figure 5.5a) intersects with $a_1 = 0$ (dashed curve) at a point f_{HD} at which the Hopf bifurcation is degenerate. Bifurcations with $f > f_{HD}$ (open circles) are supercritical and $f < f_{HD}$ (solid circles) are subcritical.

The sign of the coefficient $a_1(T)$ defines the character of Hopf bifurcation. If $a_1(T)$ is positive for the given bifurcation parameter, it undergoes a subcritical Hopf bifurcation. On the other hand, if $a_1(T)$ is negative, the bifurcation displays the characteristics of a supercritical Hopf bifurcation. Figure 5.8a illustrates the behavior of $a_1(T)$ as a function of bifurcation parameter f with b/a = 1. At temperature of 298K and b/a = 1, $a_1(T)$ becomes zero at approximately f = 0.985836, which represents the stoichiometric factor at Hopf degeneracy. Therefore the reaction exhibits a subcritical Hopf bifurcation at f = 0.52, and a supercritical Hopf bifurcation at f = 2.25. At a higher temperature 350K, $a_1(T)$ become zero at f = 0.953596. Figure 5.8b shows that the Hopf degeneracy line [$a_1(T)$ = 0] which divides subcritical and supercritical bifurcations moves towards lower f values as reported in Table 5.3. The f_{HD} is the degeneracy point for b/a = 1. Bifurcations with $f > f_{HD}$ (open circles) are supercritical and $f < f_{HD}$ (solid circles) are subcritical.

Table 5.3 Stoichiometric factors where Hopf bifurcation degenerates as a function of temperature, calculated using the activation energies of set (i) in Table 5.1. The initial reagent concentration ratio, b/a is set to 1.

Temperature (K)	f_{HD}
298	0.9858366
350	0.9535960
400	0.8739118
450	0.6897815

5.5 Conclusions

The temperature response of the two variable Oregonator model are investigated by considering all five reaction rates. The analysis is carried out in the 3-D phase space spanned by the temperature, stoichiometric factor and initial reagent concentrations. The upper temperature limits for the oscillations are calculated for a given b/a and *f*. The activation energies of the elementary reaction steps of the Oregonator model govern the overall oscillatory behavior. The predictions from the model can be correlated to the experimental findings of the temperature related BZ oscillations. Even though the BZ reaction is not a biological system, the present analysis provides insights into the role of temperature and can be extended to some of the biological oscillators. The determination of the temperature dependent subcritical or supercritical characteristics of the Hopf bifurcation is useful for the design of batch processes that run at various temperatures.

CHAPTER VI
CONCLUSIONS

6.1 Summary

The dynamics of environment sensitive PNIPAM gel particles has been investigated here, both near and away from the chemical equilibrium. In Chapter II, the freezing-melting boundaries of the charged and hard PNIPAM spheres are determined by UV Vis spectroscopy method. This method can be applied to colloidal systems in which the effective hard-sphere particle diameter during phase transition is sensitive to control variables such as temperature, pH, and salt or other chemical concentrations. The particle diameter can be measured using this technique in the coexistence regime if $\phi_{melting}$ and the dominant Bragg scattering angle are determined. The coexistence region for the chaged spheres moved towards lower concentrations, and the effective diameter of the charged particles increases with temperature due to the increase in the charge density. This method provides an accurate and time-efficient method of phase boundary analysis for temperature-sensitive polymers, and a valuable technique for inter-particle potential characterization. At low pH, the PNIPAM-co-acrylic acid microgel particles behave as thermo-sensitive hard spheres, and at high pH, the particles behave as charged spheres.

Chapter III presents a systematic study on the BZ reaction induced mechanical oscillation of PNIPAM gel particles by varying the malonic acid, sodium bromate, and the imbedded $Ru(bipy)_3$ catalyst concentrations. A ternary diagram was created to show the correlation between the dynamic behavior of the system and the substrate concentrations. It was found that the oscillating and steady state regimes coexist on the ternary diagram and are separated by a high frequency oscillation band. The dependencies of the oscillation frequency and induction time on the substrate concentrations were analyzed and tentatively explained by the inhibition effects. This

study provides guidance for tuning induction time and frequency, the two important parameters in mechanical-oscillation-facilitated colloidal assembly.

A comparative analysis of the BZ reaction characteristics between polymer immobilized and bulk catalyst systems at various temperatures is shown in Chapter IV. We found that the immobilization of the catalysts lengthens the induction time of the BZ reaction and this effect is more pronounced at lower temperatures. The high induction time for the immobilized catalyst case can be attributed to possible chemical (lowering of standard reduction potential of the ruthenium), and diffusional changes (due to the presence of a polymer network) of the BZ species due to the polymer addition. However, the rate determining step for the oscillation frequency is not affected by the polymer-catalyst interaction. Arrhenius pre-exponential factors and activation energies are calculated for both induction and oscillatory phase. The chemical bonding of PNIPAM spheres with BZ reaction catalyst can tailor the induction time while without effect on oscillation kinetics. The existence of a prolonged BZ reaction induction period with the immobilized catalyst in colloidal suspensions offers a temporal separation between the colloidal phase transition kinetics and the nonlinear dynamics of particle's size oscillation. Currently, experiments are in progress to fabricate BZ active colloidal crystals.

In Chapter V, the temperature response of the two variable Oregonator model has been investigated by considering all five reaction rates. The analysis is carried out in the 3-D phase space spanned by the temperature, stoichiometric factor and initial reagent concentrations. It is found that the activation energies of the elementary reaction steps of the Oregonator model govern the overall oscillatory behavior. The predictions from the model can be correlated to the experimental findings of the temperature related BZ oscillations. The results presented in here agree qualitatively with those of the observation in the experiments. This analysis provides insights into the role of temperature and can be extended to some of the biological oscillators.

6.2 On Going Projects

6.2.1 Phase Diagram of Charged PNIPAM Spheres

The experimental phase diagram for charged spheres investigated in Chapter II is different to that of hard sphere phase behavior, in the sense that the particles crystallize at lower volume fractions. The general trend of the charged sphere phase behavior in the concentration-temperature plane appeared to be similar to that of hard sphere phase diagram, predicted by perturbation theory. It would be interesting to correlate the experimental observation on the charged sphere phase behavior to those predictions from the theory. Therefore, the future work investigates into the application of perturbation theory to interpret charged PNIPAM sphere phase behavior. One possible route is to replace the core diameter of the neutral PNIPAM particles with the known effective diameter of the charged spheres as calculated in the results and discussion of Chapter II. This method assumes that the radial distribution functions for the solid and fluid phase are same to those in the hard sphere model.

6.2.2 Wave Patterns and Mechanical Deformation of BZ Active PNIPAM Gels

As pointed out in Chapter I, a wide range of applications are expected for the PNIPAM based polymers. An approach was developed recently for simulating chemoresponsive gels that exhibit not only large variations in volume but also alterations in shape.[95] Through this approach, oscillating gels undergoing the Belousov-Zhabotinsky (BZ) reaction were simulated, which showed that the formation of the wave pattern depends on the aspect ratios of the sample (Figure 6.1). The future work investigates into the experimental realization of the controlled dynamic patterns that give rise to distinctive oscillations in gel's shape. By probing morphological changes in BZ gels, a design criterion can be established for creating autonomous small scale devices, which perform sustained work until the reagents in the host solution are consumed and can be simply refueled by replenishing these solutes.

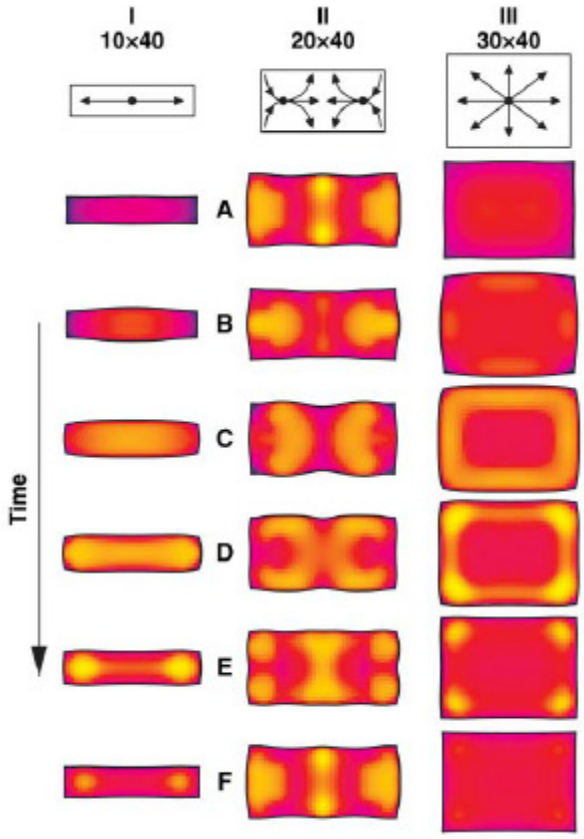

Figure 6.1 Two-dimensional wave patterns and deformations for gels of different dimensions.[95]

6.2.3 Colloidal Crystallization in Coupling to BZ Reaction

Many potential applications for colloidal crystals require samples which are free from defects over a macroscopic length scale. Several approaches have been proposed for minimizing defect formation during colloidal crystallization. A perfect (defect-free) crystal is still an idealization. The defects are due to poorly controlled kinetic processes which are affected by hydrodynamics, sedimentation, interactions among the particles etc. By inducing mechanical oscillations at the coarsening and ripening of the crystal growth, the future work focuses on controlling the kinetics of crystal growth and creating a near perfect big crystal.

Specifically, the growth and melt process of the crystallites are controlled via forced size oscillations of the PNIPAM colloidal microgels in coupling to the BZ reaction. During the oscillatory state of the BZ reaction, the volume fraction of the particles changes in accordance with the oxidization state of the ruthenium catalyst. Consequently, the sample undergoes repeated melt-recrystallize process which facilitate the crystal annealing process as shown in the Figure 6.2.

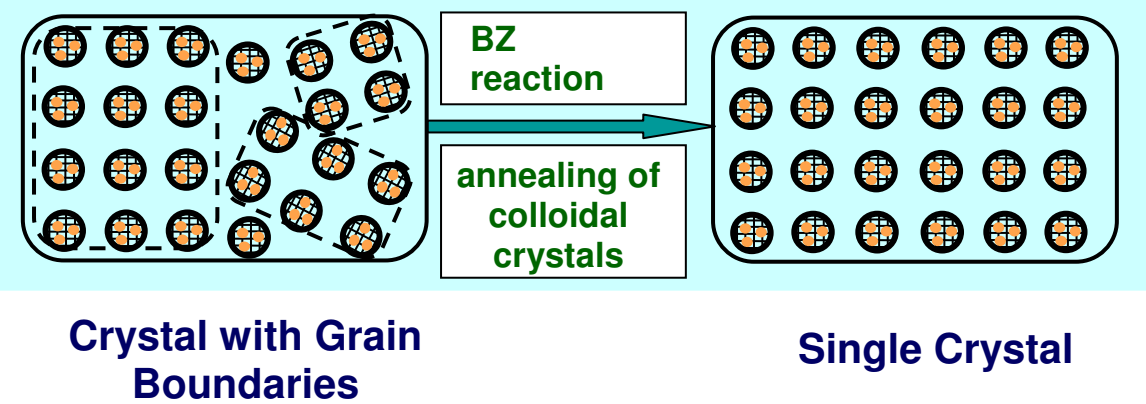

Figure 6.2 Representation of the BZ reaction facilitated colloidal self assembly.

6.2.4 Fast Responsive and High Amplitude BZ Induced PNIPAM Gel Oscillations

In this project, a novel method is developed to fabricate fast responsive self-oscillating gels with large amplitudes. The imbalance between the attractive and repulsive forces acting on the PNIPAM polymer controls the swell/shrink response of the polymer. The swelling occurs when the repulsive forces such as the ionic repulsions or osmotic forces exceeds the attractive forces such as hydrogen bonding, van der Waals interactions. In this swell/shrink process, water is diffused either from the surface towards the centre of the gel, or vice versa. It is known that the swell/shrink rate is inversely proportional to the square of the distance that the water molecules have to traverse. As a result, the gel response at macroscopic level is not sufficiently fast to make them widely useful. There are many natural examples of chemically driven actuation that rely on short diffusion

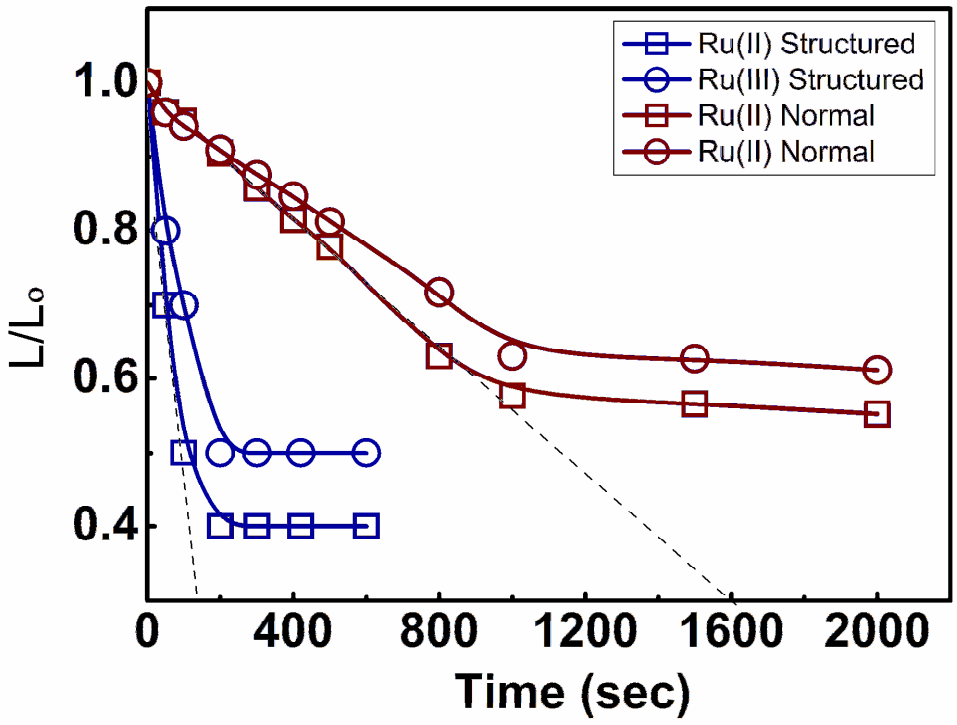

Figure 6.3 Comparison of normalized length shrinkage of PNIPAM-co-Ru(bipy)$_3$ in normal bulk and structured gel networks. The reduced and oxidized states of ruthenium are maintained by placing gel pieces in either Ce(III) or Ce(IV) solutions.

paths to produce a rapid response.[157] Faster response is desired in many areas such as drug delivery,[3] chemical and biosensing,[7] photonic crystals,[158,159] absorbants, and in separation and purification technologies.[160] Recent work by Cho et al. has demonstrated a fast responsive three dimensional gel that swells or deswells at a macroscopic level by incorporating either bridging or depletion interactions.[161] Here, we prepared fast responsive self oscillating polymer gels utilizing attractive interactions

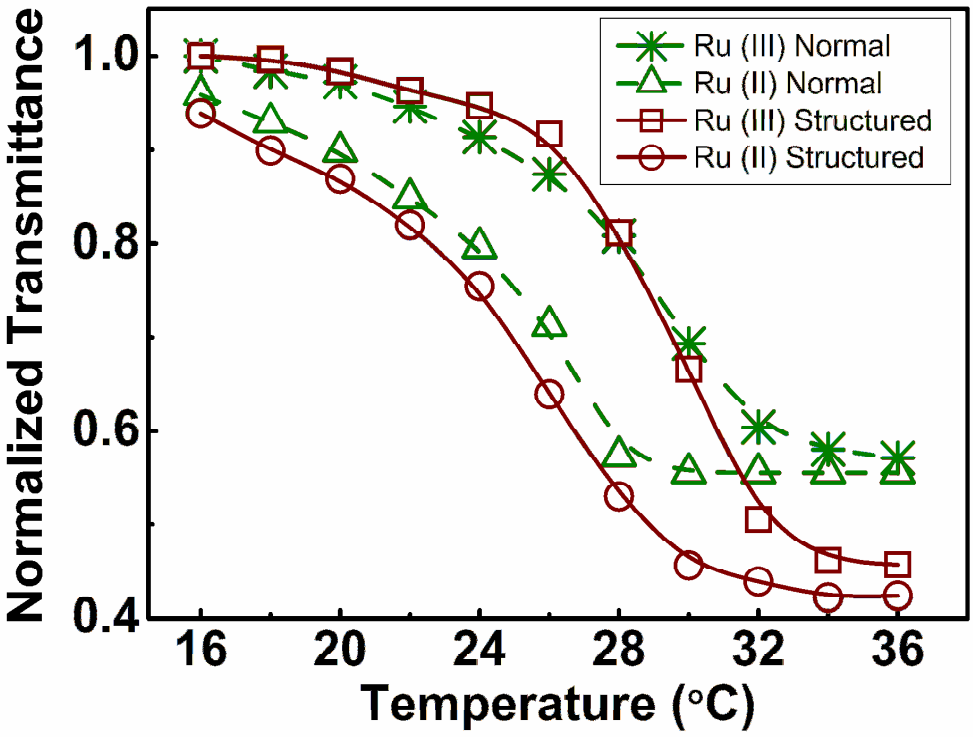

Figure 6.4 Comparison of normalized transmittance of PNIPAM-co-Ru(bipy)$_3$ in normal bulk and structured gel networks. Structured gels oscillate with larger amplitudes compared to normal bulk gels. The reduced and oxidized states of ruthenium are maintained by placing gel pieces in either Ce(III) or Ce(IV) solutions.

between positively charged ruthenium complex, allylamine and negatively charged poly(acrylic acid).

Preliminary results are suggestive of the faster response of the structured gel compared to the response in bulk gels (Figure 6.3). The gel shrinkage in length with time was monitored by placing in a solution of 1M nitric acid containing either Ce(IV)SO_4 or Ce(III)SO_4, which corresponds to the oxidized or reduced states of the ruthenium metal.

The degree of swelling in the oxidized state is higher compared to the swelling in the reduced state in both gels due to the increased Donnan osmotic pressure. It is observed that the structured microgel formed by the inter-connected gel network responds ten times faster than the bulk gel. This remarkably faster kinetics arises from the smaller dimensions of the microgel particles that form the three dimensional gel networks. The smaller size speeds up the diffusion of the fluid through the gel network. In the case of the bulk gel, the crosslinked three dimensional network reduces the diffusion of surrounding fluids and hence the gel exhibits slow response.

The normalized transmittance of the structured gel particles as a function of temperature in Figure 6.4 is measured under different oxidization states of the ruthenium metal. Compared to bulk gel particles, the structured gel particles display higher swelling and shrinkage. The structured gel particles shrink to about 40% of their original size above their LCST temperatures whereas the bulk gel particles shrink to about 55%. Therefore, in conjunction with the BZ reaction, the interconnected gel particles display higher volume changes compared to bulk particles due to the increased diffusion rates of the fluids surrounding the particles. The future work investigates into the switching time and amplitude oscillations of the PNIPAM-co-Ru(bipy)$_3$ gel between oxidized and reduced states of the ruthenium catalyst at different temperatures.

REFERENCES

(1) Lindman, S.; Lynch, I.; Thulin, E.; Nilsson, H.; Dawson, K. A.; Linse, S. *Nano Lett.* **2007**, *7*, 914-920.

(2) Pelton, R. *Adv. Colloid Interface Sci.* **2000**, *85*, 1-33.

(3) Reese, C. E.; Mikhonin, A. V.; Kamenjicki, M.; Tikhonov, A.; Asher, S. A. *J. Am. Chem. Soc.* **2004**, *126*, 1493-1496.

(4) Zhang, Y.; Guan, Y.; Zhou, S. *Biomacromolecules* **2006**, *7*, 3196-3201.

(5) Bartlett, P.; Warren, P. B. *Phys. Rev. Lett.* **1999**, *82*, 1979-1982.

(6) Debord, J. D.; Lyon, L. A. *J. Phys. Chem. B* **2000**, *104*, 6327-6331.

(7) Kim, J.; Nayak, S.; Lyon, L. A. *J. Am. Chem. Soc.* **2005**, *127*, 9588-9592.

(8) Kaholek, M.; Lee, W. K.; LaMattina, B.; Caster, K. C.; Zauscher, S. *Nano Lett.* **2004**, *4*, 373-376.

(9) Tanaka, T. *Phys. Rev. A* **1978**, *17*, 763-766.

(10) Schild, H. G. *Prog. Polym. Sci.* **1992**, *17*, 163-249.

(11) Kujawa, P.; Winnik, F. M. *Macromolecules* **2001**, *34*, 4130-4135.

(12) Zareie, H. M.; Volga, B. E.; Gunning, A. P.; Hoffman, A. S.; Piskin, E.; Morris, V. J. *Polymer* **2000**, *41*, 6723-6727.

(13) Hirokawa, Y.; Jinnai, H.; Nishikawa, Y.; Okamoto, T.; Hashimoto, T. *Macromolecules* **1999**, *32*, 7093-7099.

(14) Bulmus, V.; Ding, Z.; Long, C. J.; Stayton, P. S.; Hoffman, A. S. *Bioconjugate Chem.* **2000**, *11*, 78-83.

(15) Haeshin, L.; Tae, G. P. *Biotechnol. Progr.* **1998**, *14*, 508-516.

(16) Kim, H. K.; Park, T. G. *Enzyme Microb. Technol.* **1999**, *25*, 31-37.

(17) Oya, T.; Enoki, T.; Grosberg, A. Y.; Masamune, S.; Sakiyama, T.; Takeoka, Y.; Tanaka, K.; Wang, G.; Yilmaz, Y.; Feld, M. S.; Dasari, R.; Tanaka, T. *Science* **1999**, *286*, 1543-1545.

(18) Vernon, B.; Sung Wan, K.; You Han, B. *J. Biomater. Sci., Polym. Ed.* **1999**, *10*, 183-198.

(19) Das, M.; Mardyani, S.; Chan, W.; Kumacheva, E. *Adv. Mater.* **2006**, *18*, 80-83.

(20) Nayak, S.; Lee, H.; Chmielewski, J.; Lyon, L. A. *J. Am. Chem. Soc.* **2004**, *126*, 10258-10259.

(21) Soppimath, K. S.; Tan, D. C.; Yang, Y. Y. *Adv. Mater.* **2005**, *17*, 318-323.

(22) Masayuki, Y.; Hyeong, K.; Motohiro, H.; Akihiko, K.; Teruo, O. *J. Biomed. Mater. Res.* **2001**, *55*, 137-140.

(23) Teruo, O.; Noriko, Y.; Hideaki, S.; Yasuhisa, S. *J. Biomed. Mater. Res.* **1993**, *27*, 1243-1251.

(24) Yamato, M.; Konno, C.; Kushida, A.; Hirose, M.; Mika, U.; Kikuchi, A.; Okano, T. *Biomaterials* **2000**, *21*, 981-986.

(25) Shimizu, T.; Yamato, M.; Kikuchi, A.; Okano, T. *Tissue Eng.* **2001**, *7*, 141-151.

(26) Kondo, A.; Kamura, H.; Higashitani, K. *Appl. Microbiol. Biotechnol.* **1994**, *41*, 99-105.

(27) Rubio-Retama, J.; Zafeiropoulos, N. E.; Serafinelli, C.; Rojas-Reyna, R.; Voit, B.; Lopez Cabarcos, E.; Stamm, M. *Langmuir* **2007**, *23*, 10280-10285.

(28) Dagani, R. *Chem. Eng. News* **1997**, *9*, 26-37.

(29) Kratz, K.; Hellweg, T.; Eimer, W. *Colloids Surf., A* **2000**, *170*, 137-149.

(30) Wu, J.; Prausnitz, J. *Fluid Phase Equilib.* **2002**, *194-197*, 689-700.

(31) Wu, J.; Zhou, B.; Hu, Z. *Phys. Rev. Lett.* **2003**, *90*, 483041-483044.

(32) Fernandez-Nieves, A.; Fernandez-Barbero, A.; Vincent, B.; de las Nieves, F. J. *Macromolecules* **2000**, *33*, 2114-2118.

(33) Kawaguchi, H. *Prog. Polym. Sci.* **2000**, *25*, 1171-1210.

(34) Saunders, B. R.; Vincent, B. *Adv. Colloid Interface Sci.* **1999**, *80*, 1-25.

(35) Laukkanen, A.; Hietala, S.; Maunu, S. L.; Tenhu, H. *Macromolecules* **2000**, *33*, 8703-8708.

(36) Gao, J.; Hu, Z. *Langmuir* **2002**, *18*, 1360-1367.

(37) Senff, H.; Richtering, W. *J. Chem. Phys.* **1999**, *111*, 1705-1711.

(38) Flory, P. J. *Principles of Polymer Chemistry*; Cornell University Press: Ithaca, NY, USA, 1953.

(39) Toshiaki, H.; John, P. *J. Appl. Polym. Sci.* **1996**, *62*, 1635-1640.

(40) Gil-Villegas, A.; Galindo, A.; Whitehead, P. J.; Mills, S. J.; Jackson, G.; Burgess, A. N. *J. Chem. Phys.* **1997**, *106*, 4168-4186.

(41) Hansen, J. P.; McDonald, I. R. *Theory of Simple Liquids*; 2nd ed.; Academic Press: London, 1986.

(42) Hellweg, T.; Dewhurst, C. D.; Brückner, E.; Kratz, K.; Eimer, W. *Colloid. Polym. Sci.* **2000**, *278*, 972-978.

(43) Lennard-Jones, J. E.; Devonshire, A. F. *Proc. R. Soc. London, Ser. A* **1937**, *163*, 53-70.

(44) Yoshida, R. *Curr. Org. Chem.* **2005**, *9*, 1617-1641.

(45) Yoshida, R. *Bull. Chem. Soc. Jpn.* **2008**, *81*, 676-688.

(46) Epstein, I. R.; Pojman, J. A. *An Introduction to Nonlinear Chemical Dynamics: Oscillations, Waves, Patterns and Chaos*; Oxford University Press: New York, 1998.

(47) Field, R. J.; Koros, E.; Noyes, R. M. *J. Am. Chem. Soc.* **1972**, *94*, 8649-8664.

(48) Scott, S. K. *Oscillations, Waves, and Chaos in Chemical Kinetics*; Oxford University Press Inc.: New York, 1994.

(49) Epstein, I. R. *Proc. Nat. Acad. Sci. U.S.A.* **2006**, *103*, 15727-15728.

(50) Chance, B.; Pye, E. K.; Ghosh, A. K.; Hess, B. *Biological and Biochemical Oscillators*; Academic Press: New York, 1973.

(51) Gray, R. A.; Jalife, J.; Panfilov, A. V.; Baxter, W. T.; Cabo, C.; Davidenko, J. M.; Pertsov, A. M.; Hogeweg, P.; Winfree, A. T. *Science* **1995**, *270*, 1222-1223.

(52) Winfree, A. T.; Strogatz, S. H. *Nature* **1984**, *311*, 611-615.

(53) Kondo, S.; Asai, R. *Nature* **1995**, *376*, 765-768.

(54) Suzuki, N.; Hirata, M.; Kondo, S. *Proc. Nat. Acad. Sci. U.S.A.* **2003**, *100*, 9680-9685.

(55) Kuhnert, L.; Agladze, K. I.; Krinsky, V. I. *Nature* **1989**, *337*, 244-247.

(56) Yoshida, R.; Takahashi, T.; Yamaguchi, T.; Ichijo, H. *J. Am. Chem. Soc.* **1996**, *118*, 5134-5135.

(57) Yoshida, R.; Tanaka, M.; Onodera, S.; Yamaguchi, T.; Kokufuta, E. *J. Phys. Chem. A* **2000**, *104*, 7549-7555.

(58) Yoshida, R.; Yamaguchi, T.; Kokufuta, E. *J. Intell. Mater. Syst. Struct.* **1999**, *10*, 451-457.

(59) Tateyama, S.; Shibuta, Y.; Yoshida, R. *J. Phys. Chem. B* **2008**, *112*, 1777-1782.

(60) Yoshida, R.; Onodera, S.; Yamaguchi, T.; Kokufuta, E. *J. Phys. Chem. A* **1999**, *103*, 8573-8578.

(61) Maeda, S.; Hara, Y.; Sakai, T.; Yoshida, R.; Hashimoto, S. *Adv. Mater.* **2007**, *19*, 3480-3484.

(62) Sakai, T.; Takeoka, Y.; Seki, T.; Yoshida, R. *Langmuir* **2007**, *23*, 8651-8654.

(63) Shinohara, S.; Seki, T.; Sakai, T.; Yoshida, R.; Takeoka, Y. *Angew. Chem. Int. Ed.* **2008**, *47*, 9039-9043.

(64) Hara, Y.; Yoshida, R. *Langmuir* **2005**, *21*, 9773-9776.

(65) Hara, Y.; Yoshida, R. *J. Phys. Chem. B* **2005**, *109*, 9451-9454.

(66) Hara, Y.; Sakai, T.; Maeda, S.; Hashimoto, S.; Yoshida, R. *J. Phys. Chem. B* **2005**, *109*, 23316-23319.

(67) Field, R. J.; Noyes, R. M. *J. Chem. Phys.* **1974**, *60*, 1877-1884.

(68) Tyson, J. In *Oscillations and Traveling Waves in Chemical Systems*; Field, R., Burger, M., Eds.; Wiley-Interscience: New York, 1985, p 93-144.

(69) Pusey, P. N.; van Megen, W. *Nature* **1986**, *320*, 340-342.

(70) van Megen, W.; Pusey, P. N. *Phys. Rev. A* **1991**, *43*, 5429-5441.

(71) van Megen, W.; Underwood, S. M. *Phys. Rev. E* **1994**, *49*, 4206-4220.

(72) Gasser, U.; Weeks, E. R.; Schofield, A.; Pusey, P. N.; Weitz, D. A. *Science* **2001**, *292*, 258-262.

(73) Kegel, W. K.; Blaaderen, V. *Science* **2000**, *287*, 290-293.

(74) Weeks, E. R.; Crocker, J. C.; Levitt, A. C.; Schofield, A.; Weitz, D. A. *Science* **2000**, *287*, 627-631.

(75) Tang, S.; Hu, Z.; Cheng, Z.; Wu, J. *Langmuir* **2004**, *20*, 8858-8864.

(76) Hans, J. S.; Thomas, P. *J. Phys.: Condens. Matter* **2002**, *14*, 11573.

(77) Ackerson, B. J.; Schätzel, K. *Phys. Rev. E* **1995**, *52*, 6448.

(78) Cheng, Z.; Chaikin, P. M.; Russel, W. B.; Meyer, W. V.; Zhu, J.; Rogers, R. B.; Ottewill, R. H. *Mater. Des.* **2001**, *22*, 529-534.

(79) Cheng, Z.; Chaikin, P. M.; Zhu, J.; Russel, W. B.; Meyer, W. V. *Phys. Rev. Lett.* **2001**, *88*, 0155011-0155014.

(80) Cheng, Z.; Russel, W. B.; Chaikin, P. M. *Nature* **1999**, *401*, 893-895.

(81) Cheng, Z.; Zhu, J.; Russel, W. B.; Chaikin, P. M. *Phys. Rev. Lett.* **2000**, *85*, 1460-1463.

(82) Dixit, N. M.; Zukoski, C. F. *Phys. Rev. E* **2001**, *64*, 04160401-04160411.

(83) Lyon, L. A.; Debord, J. D.; Debord, S. B.; Jones, C. D.; McGrath, J. G.; Serpe, M. J. *J. Phys. Chem. B* **2004**, *108*, 19099-19108.

(84) Hoare, T.; Pelton, R. *Macromolecules* **2004**, *37*, 2544-2550.

(85) Jones, C. D.; Lyon, L. A. *Macromolecules* **2000**, *33*, 8301-8306.

(86) Zhou, S.; Chu, B. *J. Phys. Chem. B* **1998**, *102*, 1364-1371.

(87) Alsayed, A. M.; Islam, M. F.; Zhang, J.; Collings, P. J.; Yodh, A. G. *Science* **2005**, *309*, 1207-1210.

(88) Clements, M.; Pullela, S. R.; Mejia, A. F.; Shen, J.; Gong, T.; Cheng, Z. *J. Colloid Interface Sci.* **2008**, *317*, 96-100.

(89) Elton, N. J.; Gate, L. F.; Preston, J. S. *Pure Appl. Opt.* **1998**, 1309.

(90) Bryant, G.; Williams, S. R.; Qian, L.; Snook, I. K.; Perez, E.; Pincet, F. *Phys. Rev. E* **2002**, *66*, 0605011-0605014.

(91) Biosa, G.; Masia, M.; Marchettini, N.; Rustici, M. *Chem. Phys.* **2005**, *308*, 7-12.

(92) Murray, J., D. *Mathematical Biology*; Springer-Verlag: Berlin, Germany, 1993; Vol. 19.

(93) Gyorgyi, L.; Turanyi, T.; Field, R. J. *J. Phys. Chem.* **1990**, *94*, 7162-7170.

(94) Bishop, K.; Fialkowski, M.; Grzybowski, B. A. *J. Am. Chem. Soc.* **2005**, *127*, 15943-15948.

(95) Yashin, V. V.; Balazs, A. C. *Science* **2006**, *314*, 798-801.

(96) Miyakawa, K.; Sakamoto, F.; Yoshida, R.; Kokufuta, E.; Yamaguchi, T. *Phys. Rev. E* **2000**, *62*, 793.

(97) Toth, R.; Taylor, A. F.; Tinsley, M. R. *J. Phys. Chem. B* **2006**, *110*, 10170-10176.

(98) Vanag, V. K.; Epstein, I. R. *Science* **2001**, *294*, 835-837.

(99) Yoshikawa, K.; Aihara, R.; Agladze, K. *J. Phys. Chem. A* **1998**, *102*, 7649-7652.

(100) Ginn, B. T.; Steinbock, B.; Kahveci, M.; Steinbock, O. *J. Phys. Chem. A* **2004**, *108*, 1325-1332.

(101) Miyakawa, K.; Okabe, T.; Mizoguchi, M.; Sakamoto, F. *J. Chem. Phys.* **1995**, *103*, 9621-9625.

(102) Epstein, I. R. *Physica D* **1991**, *51*, 152-60.

(103) Yoshida, R.; Takahashi, T.; Yamaguchi, T.; Ichijo, H. *Adv. Mater.* **1997**, *9*, 175-178.

(104) Suzuki, D.; Yoshida, R. *Macromolecules* **2008**, *41*, 5830-5838.

(105) Yoshida, R.; Sakai, T.; Ito, S.; Yamaguchi, T. *J. Am. Chem. Soc.* **2002**, *124*, 8095-8098.

(106) Yoshida, R.; Sakai, T.; Ito, S.; Yamaguchi, T. *Polym. Prepr. (Am. Chem. Soc., Div. Polym. Chem.)* **2002**, *43*, 802-803.

(107) Yoshida, R.; Sakai, T.; Ito, S.; Yamaguchi, T. *ACS Symp. Ser.* **2004**, *869*, 30-43.

(108) Yoshida, R.; Sakai, T.; Tambata, O.; Yamaguchi, T. *Sci. Technol. Adv. Mater.* **2002**, *3*, 95-102.

(109) Yoshida, R.; Takei, K.; Yamaguchi, T. *Macromolecules* **2003**, *36*, 1759-1761.

(110) Sakai, T.; Hara, Y.; Yoshida, R. *Macromol. Rapid Commun.* **2005**, *26*, 1140-1144.

(111) Yoshida, R.; Otoshi, G.; Yamaguchi, T.; Kokufuta, E. *J. Phys. Chem. A* **2001**, *105*, 3667-3672.

(112) Shen, J.; Pullela, S.; Marquez, M.; Cheng, Z. *J. Phys. Chem. A* **2007**, *111*, 12081-12085.

(113) Abruna, H. D.; Breikss, A. I.; Collum, D. B. *Inorg. Chem.* **1985**, *24*, 987-988.

(114) Kofke, D. A.; Bolhuis, P. G. *Phys. Rev. E* **1999**, *59*, 618.

(115) Pronk, S.; Frenkel, D. *J. Chem. Phys.* **2004**, *120*, 6764-6768.

(116) Sakai, T.; Yoshida, R. *Langmuir* **2004**, *20*, 1036-1038.

(117) Koros, E. *Nature* **1974**, *251*, 703-704.

(118) Ruoff, P. *Physica D* **1995**, *84*, 204-211.

(119) Sciascia, L.; Lombardo, R.; Turco Liveri, M. L. *Chem. Phys. Lett.* **2006**, *430*, 67-70.

(120) Maeda, S.; Hara, Y.; Yoshida, R.; Hashimoto, S. *Angew. Chem. Int. Ed.* **2008**, *47*, 6690-6693.

(121) Szalai, I.; Oslonovitch, J.; Forsterling, H. D. *J. Phys. Chem. A* **2000**, *104*, 1495-1498.

(122) Didenko, O. Z.; Strizhak, P. E. *Chem. Phys. Lett.* **2001**, *340*, 55-61.

(123) Blandamer, M. J.; Roberts, D. L. *J. Chem. Soc., Faraday Trans. 1* **1977**, *73*, 1056-1065.

(124) Burger, M.; Koros, E. *J. Phys. Chem.* **1980**, *84*, 496-500.

(125) Kokufuta, E. *Prog. Polym. Sci.* **1992**, *17*, 647-697.

(126) Koros, E. *Faraday Symp. Chem. Soc.* **1974**, *9*, 28-37.

(127) Strizhak, P. E.; Didenko, O. Z. *Theor. Exp. Chem.* **1994**, *29*, 128-131.

(128) Cowan, D. A. *Trends Microbiol.* **2004**, *12*, 58-60.

(129) Stetter, K. *Extremophiles: Microbial life in Extreme Environments*; Wiley-Liss: New York, 1998.

(130) Field, R. J. *J. Chem. Phys.* **1975**, *63*, 2289-2296.

(131) Gyorgyi, L.; Field, R. J. *Nature* **1992**, *355*, 808-810.

(132) Petrov, V.; Gaspar, V.; Masere, J.; Showalter, K. *Nature* **1993**, *361*, 240-243.

(133) Ruoff, P. *Chem. Phys. Lett.* **1982**, *90*, 76-80.

(134) Showalter, K.; Noyes, R. M.; Bar-Eli, K. *J. Chem. Phys.* **1978**, *69*, 2514-2524.

(135) Tyson, J. J. *Ann. N.Y. Acad. Sci.* **1979**, *316*, 279-295.

(136) Tyson, J. J. *J. Phys. Chem.* **1982**, *86*, 3006-3012.

(137) Field, R. J.; Noyes, R. M. *Faraday Symp. Chem. Soc.* **1974**, *9*, 21-27.

(138) Geiseler, W.; Föllner, H. H. *Biophys. Chem.* **1977**, *6*, 107-115.

(139) Epstein, I. R. *Nature* **1995**, *374*, 321-327.

(140) Winfree, A. T. *Science* **1972**, *175*, 634-636.

(141) Taboada, J. J.; Munuzuri, A. P.; Perez-Munuzuri, V.; Gomez-Gesteira, M.; Perez-Villar, V. *Chaos* **1994**, *4*, 519-524.

(142) Sriram, K.; Bernard, S. *Chaos* **2008**, *18*, 023126-12.

(143) Dutt, A. K.; Mueller, S. C. *J. Phys. Chem.* **1993**, *97*, 10059-10063.

(144) Foerster, P.; Mueller, S. C.; Hess, B. *J. Phys. Chem.* **1990**, *94*, 8859-8861.

(145) Masia, M.; Marchettini, N.; Zambrano, V.; Rustici, M. *Chem. Phys. Lett.* **2001**, *341*, 285-291.

(146) Misra, G. P. *Chem. Phys. Lett.* **1992**, *191*, 435-440.

(147) Nagy, G.; Körös, E.; Oftedal, N.; Tjelflaat, K.; Ruoff, P. *Chem. Phys. Lett.* **1996**, *250*, 255-260.

(148) Blandamer, M. J.; Morris, S. H. *J. Chem. Soc. Faraday Trans. 1* **1975**, *71*, 2319-2330.

(149) Mazzotti, M.; Morbidelli, M.; Serravalle, G. *J. Phys. Chem.* **1995**, *99*, 4501-4511.

(150) Zhang, J.; Zhou, L.; Ouyang, Q. *J. Phys. Chem. A* **2007**, *111*, 1052-1056.

(151) Dockery, J. D.; Keener, J. P.; Tyson, J. J. *Physica D* **1988**, *30*, 177-191.

(152) Tyson, J. J. *The Belousov-Zhabotinskii Reaction*; Springer-Verlag: New York, 1976.

(153) Gray, P., S. *Chemical Oscillations and Instabilities*; Oxford University Press: Oxford, UK, 1990.

(154) Guckenheimer, J. *Nonlinear Oscillations, Dynamical Systems, and Bifurcations of Vector Fileds*; Springer-Verlag: New York, 2002.

(155) Nagao, R.; Epstein, I. R.; Gonzalez, E. R.; Varela, H. *J. Phys. Chem. A* **2008**, *112*, 4617-4624.

(156) Carbonio, E. A.; Nagao, R.; Gonzalez, E. R.; Varela, H. *Phys. Chem. Chem. Phys.* **2009**, *11*, 665-670.

(157) Schmidt, N. *Animal Physiology*; Cambridge University Press: Cambridge, UK, 1975.

(158) Hu, Z.; Huang, G. *Angew. Chem. Int. Ed.* **2003**, *42*, 4799-4802.

(159) Kawaguchi, H.; Fujimoto, K.; Mizuhara, Y. *Colloid. Polym. Sci.* **1992**, *270*, 53-57.

(160) Huang, R. *Membrane Science and Technology Series, 1. Pervaporation Membrane Separation Processes*; Elsevier: Amsterdam, The Netherlands, 1991.

(161) Cho, E. C.; Kim, J. W.; Fernandez Nieves, A.; Weitz, D. A. *Nano Lett.* **2008**, *8*, 168-172.

VITA

Srinivasa Rao Pullela received his Bachelor of Science degree in chemical technology from the University Institute of Chemical Technology (UICT) at the University of Mumbai in 1999. He entered the chemistry program at Oklahoma State University, Stillwater, OK in August 2001 and received his Master of Science degree in July 2004. He later joined the Department of Chemical Engineering at Texas A&M University, College Station, TX in January 2005 and received his Doctor of Philosophy degree in May 2009. His research interests include nonlinear chemical dynamics and equilibrium colloidal phase transitions of environment-sensitive poly(N-isopropylacrylamide) microgels.

Srinivasa Pullela may be contacted through Dr. Zhengdong Cheng at the Chemical Engineering Department, Texas A&M University, College Station, TX 77843-3122.